Department of Information Engineering, Electronics and Telecommunications

PhD in Electronics Engineering – XXXV cycle

Transparent selective contacts for silicon-based heterojunction solar cells

Francesca Menchini

Supervisors:

Prof. Giampiero de Cesare - DIET, Sapienza University of Rome, Italy

Ing. Mario Tucci - TERIN Department, ENEA, Rome, Italy

A.A. 2022-2023

Forewords and acknowledgements

The idea of getting a PhD degree was in my mind since a long time, but decisive was a pleasant conference in Nice, during which a colleague convinced me not to postpone anymore. So, my first thanks go to my colleague and friend Valentina Pinto.

But I would have never taken the challenge if I were not sure of being surrounded by the right environment, which I call "my thermal bath": the Photovoltaic Technology Laboratory, full of people, ideas, competences and talents that always pushed me one step forward.

My deepest gratitude goes to Ing. Mario Tucci, who is much more than a boss. He accepted me in his group and always showed me his esteem. He taught me with patience and passion, and never stopped me from going through new experiences.

A warm thank to Prof. Giampiero de Cesare and Prof. Domenico Caputo for their master courses and for having given me precious advices during my experience inside the University.

I deeply thank my "brother" Dr. Luca Serenelli, a brilliant experimentalist, with an elephant memory and a golden heart. He shared with me all his knowledge and all the ups and downs. You gave me *the force*!

Thanks to Dr. Luca Martini, the curious engineer, for helping me with HF experiments and much more, for his passion for science and for his joyful whistling.

I am sincerely grateful to Dr. Teodoro Dikonimos and Dr. Nicola Lisi for having shared with me their competences on photoelectron spectroscopy, which has become a passion. I thank Prof. Alessandro Latini for the preparation of the precursors and for the advices in chemistry. Thanks to Dr. Marco Montecchi for his help with optical characterisations.

Thanks to the entire FSD-IIF group: to Claudia, Glauco, Matteo, Enrico, Pietro, Alberto, Massimo, Franco, Riccardo for their help with the experiments, for the scientific and human discussions, for the positive influence and for the daily company.

Last, and not at all least, I thank my family for their patience in having understood my commitment and having tolerated the late dinners. You touched me with your respect for my work and I will miss your glances beyond my shoulders when I sat at the PC! I thank my husband, who actually pushed me into the challenge since the beginning. He carried the burden of the busiest days and always sustained me with his love. You were my strength and I dedicate this gratification to you all.

Abstract

Renewable energies are nowadays recognised to be the protagonists of a necessary sustainable transition in the energy production process. Among the existing technologies, photovoltaic (PV) stands out for the infinite availability of the source, the direct efficient energy transformation and for low global energy costs. These reasons drive the global research toward materials and methods to obtain higher and higher efficiencies.

Beyond the well-assessed silicon-based homojunction technology, that covers the 95% of the total PV production, the amorphous/crystalline-silicon heterojunction (HJ) concept is gaining increasing market share. Heterojunctions are able to overcome some shortcomings of homojunctions, such as the high thermal budget connected to the diffusion process to achieve the doping and to the recombination losses that limit the V_{OC}. However HJs still require complex architectures and the use of toxic and dangerous gases, which demand costly measures for a safe industrial manufacturing. A new approach to circumvent some of the above-mentioned issues is currently explored with increasing interest, and involves the use of non-doped, non-silicon films to replace the amorphous-silicon ones. A great variety of materials has already been proposed and tested for the purpose, but some challenges still have to be completely solved, first of all the resistance to thermal annealing at 200-250°C, that is a necessary step in module assembling. Moreover, in view of an industrial application, the manufacture of these novel materials needs to satisfy several constrains and then guarantee an easy and high-throughput process.

In this thesis the attention is focused on some of these novel materials for both emitter and base contacts of a heterostructure solar cell based on n-type doped crystalline silicon. In particular nickel oxide and titanium oxide or zinc sulphide are exploited as selective emitter and base contact respectively. These materials have to be more transparent than the doped amorphous layer counterpart to enhance the quantum yield of the solar cell in the blue region of the solar spectrum where the amorphous films introduce parasitic absorptions. Moreover the substitute layers must be deposited on the well-assessed thin buffer layer of amorphous silicon suboxide used in our laboratory to passivate the surfaces of the silicon wafer, therefore the most relevant constrain to fulfil is to avoid any contamination and any detrimental thermal stress of the surface passivation. On the basis of these requirements, particular care will be given to the choice of the deposition procedures as well as to the choice of the doping elements to be introduced into the selective contacts. The measurement of silicon surface passivation will be adopted as the most relevant method to evaluate the suitability of materials and manufacturing methods. Numerical simulations will also be used to evaluate the ideal band diagram of the proposed heterostructures and to verify how differences in the experimental properties of the materials with respect to ideality could affect the heterostructure device performances.

In analogy with the doped amorphous layers used in conventional HJs, also the proposed novel materials for selective contacts need to be coupled to a transparent conductive oxide to make up for the poor lateral conductivity that still remains a basic issue of any selective layer proposed in the literature up to now. In this thesis a promising material is tested as an alternative to indium tin oxide, namely tungsten-doped indium oxide. It is found that non-reactive radio-frequency sputtering is suited to grow transparent films with very high mobility and low resistivity due a low carrier concentration that reduces parasitic absorptions. Most importantly, the sputtering damage to surface passivation of the crystalline silicon substrates can be completely recovered after a suitable thermal annealing.

All the discussed results show that ideal materials or totally qualified deposition methods for obtaining alternative selective contacts have yet to be found, mostly from the point of view of the resistance to thermal treatments. This thesis adds some tiles to the road to high-efficiency, low-thermal budget, low-toxicity, high-throughput silicon-based heterojunctions.

List of contents

Forewords and acknowledgements i

Abstract ii

Chapter1 - Introduction 1
1.1 The energetic transition 1
1.2 The race for high efficiency solar cells 2
1.3 Aim and structure of the thesis 3
1.4 Framework and collaborations 4

Chapter 2 - Silicon heterojunction solar cells working principles and efficiency limitations
2.1 Basics of solar cells 7
2.2 Crystalline-silicon solar cell structures 10
2.3 Silicon heterojunctions: working principles and limitations 12
2.3.1 Structure of the standard HJ solar cells 12
2.3.2 Working principles 13
2.3.3 Advantages and drawbacks of HJs 16
2.3.4 Fill factor limitations due to the TCO work function and an indirect method to evaluate them 17
2.3.5 Fill factor limitations due to hidden barriers at the base contact and a method to detect them 19
2.3.6 Fill factor limitations due to barriers at the emitter contact and a method to detect them 21
2.3.7 V_{OC} limitations due to edge recombination 23
2.4 Alternative carrier selective contacts 24
2.5 The choice for the passivation layer 27
2.6 Summary 28

Chapter 3 - Doped nickel oxide as hole-transport layer
3.1 Introduction 34
3.2 Nickel oxide and its applications in silicon heterojunctions... 35
3.3 Conductivity of pure, sub-stoichiometric and doped nickel oxide 36
3.4 lectron-beam deposited NiOx:Li as hole-transport layer 37
3.5 Thermally evaporated NiOx:Li as hole-transport layer 42
3.6 Conclusions on NiOx:Li 46
3.7 Thermally evaporated NiOx:Ag 46

3.7.1 The idea of "decoupling" layers: lithium fluoride (LiF) 50
3.7.2 Another decoupling layer: titanium dioxide (TiO_2) 51
3.7.3 The double interlayer 55
3.8 Conclusions on doped NiO as hole-transport layer 58

Chapter 4 - Materials for electron-transport layers
4.1 Introduction 63
4.2 Tungsten-doped titanium dioxide as electron-transport layer 63
4.2.1 Thermally evaporated TiOx:W as electron-transport layer 65
4.2.2 Conclusions on TiOx:W 67
4.3 Oxide, fluorides and selenides tunnelling contacts 68
4.3.2 LiF/Ti base contact 71
4.3.3 LiF/TiO_2/Ti base contact 72
4.3.4 MgF_2/Ti base contact 73
4.3.5 MgF_2/ZnS/Ti base contact 74
4.4 Conclusions on materials for base contacts 75

Chapter 5 - Indium tungsten oxide (IWO) as a high-mobility TCO
5.1 Introduction 79
5.2 IWO films deposited by reactive RF sputtering 81
5.3 IWO films deposited by non-reactive RF sputtering 83
5.4 Heterojunctions containing IWO films as TCO 89
5.4.1 Work function evaluation 89
5.4.2 Solar cells 90
5.5 Summary, conclusions and future perspectives 92

Chapter 6 - Additional research 97

Conclusions 105

Appendix 107
A.1 Deposition techniques 107
A.2 Materials 107
A.3 Experimental methods and measuring techniques 108
A.4 GDOES measurements 110
A.5 Ohmic contact with InGa 112

List of publications vi

Chapter 1

Introduction

In this chapter the motivation for photovoltaic research is given and an outline of the thesis presented.

1.1 The energetic transition

Since the origin of planet Earth, the Sun has been the source of light and life. And it has undoubtedly been for free. Now that the global energy demand is constantly growing, we should be aware that this limitless resource could represent our future.

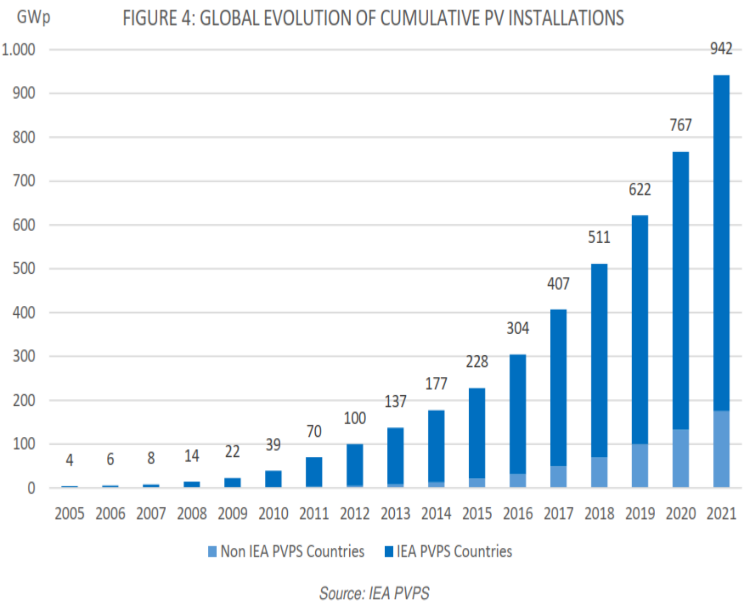

Figure 1.1 Global evolution of cumulative PV installations [4].

Since 2000 the world community has started debating about global warming, which anthropic component has been recognised in the excess greenhouse gases mostly produced by fossil fuel combustion. Renewable energies are thus the protagonists of all world policies that aim at acting a clear sustainable transition in the energy production process. Renewables generated 29% of global electricity in 2021, with a growing trend from 20.4% in 2011 [1]. Beyond wind, waves, tides and geothermal, solar energy stands out for its wider availability and for its one-step conversion

process; in particular, photovoltaics (PV) has undergone a frenetic growth thanks to technological innovations. According to IRENA, the International Renewable Energy Agency, the cost of PV power production has decreased by 82% in the last decade [2], with a global electricity cost of 0.048 $/kWh. Again in 2021, solar PV kept its record-breaking pathway, adding 175 GW of new capacity, reaching nowadays a cumulative total of around 1 TW, definitely higher than the value reported in Figure 1.1 for 2021 [3, 4].

Solar energy alone could fulfil the entire needs of humanity, with its 50 kTW power over the whole terrestrial surface. A few minutes of solar irradiation could satisfy a one-year world demand. Of course, the surface that can be dedicated to PV production is limited, so that the pursuit for more efficient solar cells is still a trend topic.

1.2 The race for high efficiency solar cells

Since the fortuitous discovery of the photovoltaic effect by Alexandre Edmond Becquerel in 1839 and the first rudimentary selenium photovoltaic cell built in 1879 by Charles Fritts, the development of more and more efficient solar cells has still not ended.

Every year the National Renewable Energy Laboratory (NREL) in U.S. updates a chart of the highest confirmed conversion efficiencies for research cells, which latest version is shown in Figure 1.2 [5]. The best efficiencies are actually obtained with multi-junction cells or single-junction GaAs cells under concentrated sunlight regime, but the high production costs makes that the most diffused technology on the market is based on crystalline silicon (c-Si) cells.

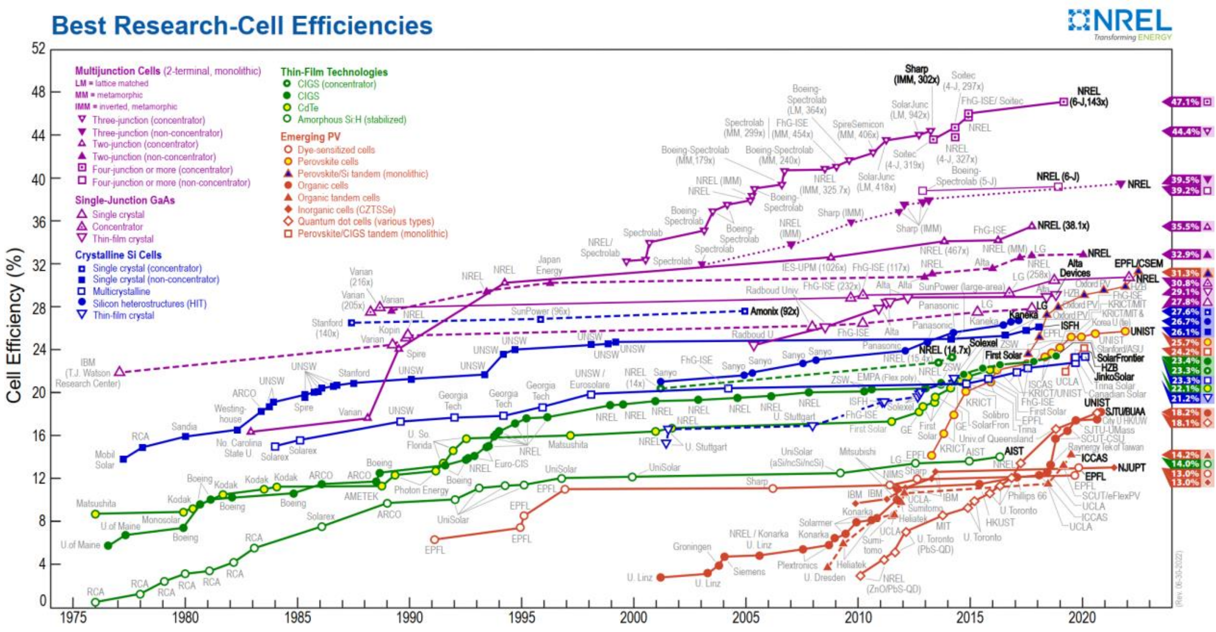

Figure 1.2 NREL efficiency chart for research cells [5].

Between 2010 and 2014 the mainstream technology for mass-production was based upon 6 in. (156 mm) square cells based on multicrystalline p-type silicon wafers, which then evolved to monocrystalline Si and PERC architecture that covered 80% of the production in 2016 (Figure 1.3a). The growth of PERC/PERT/PERL technology forecasted for 2021 (Figure 1.3a) was greatly surpassed by actual production (Figure 1.3b), and is believed to keep dominating the market for many years to come [6]. The ultimate technological change will be the migration to heterojunction cells based on n-type wafers, and the route has already started: as an example, in 2022 Enel Green Power in Italy has recently installed a world-unique production plant of bifacial photovoltaic panels with cutting-edge heterojunction technology (HJT) that uses amorphous crystalline silicon [7]. Silicon heterojunctions (SHJs) are expected to gain a market share of about 20% by 2032. The other emerging technology to attain high efficiency is based on tandem silicon-perovskite solar cells, which claim the possibility to overtake the theoretical limit of silicon-based technologies.

Aimed by these observations, a consistent part of the research community is continuously making efforts to optimise solar cells, looking for growing efficiencies and at the same time making sure to keep production processes simple and low-cost. The main research fields include new materials and new architectures.

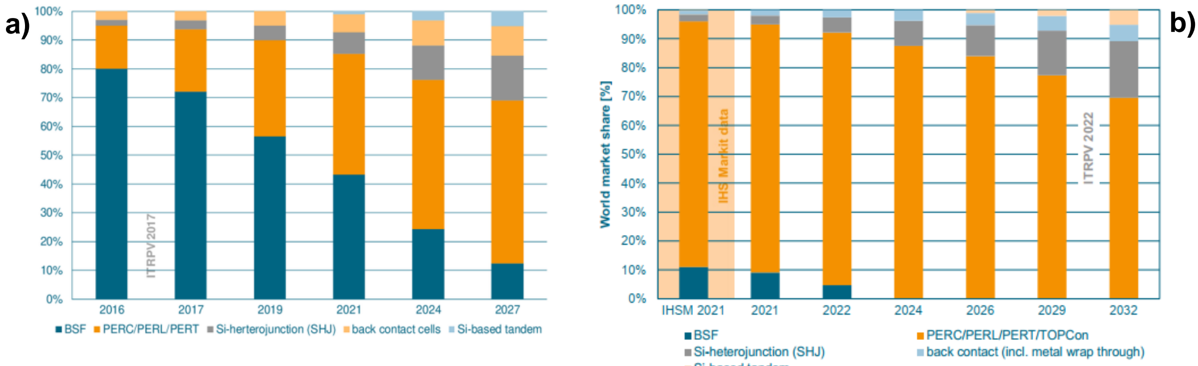

Figure 1.3 World market share of different cell technologies as assessed and forecasted a) in 2017 and b) in 2022 [6].

1.3 Aim and structure of the thesis

The demand for high-efficiency solar cells pusher the photovoltaic research to pursue new objectives and identify innovative solutions in a field where the theoretical limit has not yet been reached. The new routes can follow different paths, from the optimisation of the efficiency to the maximization of production/cost factors, always passing through technological innovation and scientific intuition. This thesis focuses on the emerging technology of silicon heterojunction solar cells, which promises to be the leading trail in the next years. Notwithstanding their known advantages over homojunction solar cells, heterojunctions still suffer from some limitations mainly connected to the presence of doped layers. Such latter elements, fundamental to the functioning of

the cell, are produced in processes that involve high temperatures and, more importantly, the use of toxic and dangerous gases such as phosphine and diborane or trimetilborane. In this way the production process becomes demanding in terms of costs and safety issues. The new trend to overcome these limitations consists in the search for new materials to exploit the *carrier-selective contact* concept. In this new approach the traditional amorphous silicon layers are replaced by non-doped, non-silicon films which can help reducing the heterojunction limitations to high efficiency while simultaneously simplifying the production process.

The thesis is divided in six chapters, of which a brief description is given in the following. Chapter 1 serves as an introduction to the role of photovoltaic technologies in the energetic transition that we are now traversing. The most efficient solar cells at laboratory level are presented, and the potentialities of heterojunctions are indicated. Chapter 2 describes the basic working principles of solar cells, with a description of different architectures to end up with heterojunctions (HJs). The functioning principles of HJs are then given, together with some of their advantages and drawbacks. Some factors limiting high-efficiency HJ solar cells and the need for optimised selective contacts and TCOs are discussed. Finally new concepts for carrier selective contacts are presented, and are used as a starting point for the subsequent experimental work. Chapter 3 describes investigations on doped nickel oxide to be used as a hole-transport layer. Different deposition methods are tested, and their suitability is discussed. A possible strategy to avoid lifetime degradation due to metal diffusion is proposed. Chapter 4 describes experiments on different materials as electron-transport layers. Thermally-evaporated doped titanium oxide is investigated, and its limits are discussed. Different materials are also tested as decoupling layers to preserve passivation, and the best results are presented. Chapter 5 contains a detailed study on indium tungsten oxide films to be used as transparent selective contacts. The films are found to possess high mobility, high transparency and low carrier density, which make them suitable for the proposed application. Most importantly, the substrate lifetime after deposition and subsequent annealing is recovered and even surpassed. Chapter 6 summarises the results of additional research performed during the period of the PhD course. Finally, conclusions and perspectives are discussed. Appendix 1 sketches some methods and procedures common to most experiments presented in this work.

1.4 Framework and collaborations

The work described in this thesis was performed between 2019 and 2022, while I was working as a researcher in the ENEA Photovoltaic Laboratory. The work was almost entirely included in the framework of the AMPERE European Project* and of the MiSE-ENEA Agreement on Research on the National Electric System**, which demonstrates the strong interests of national and international institutions in the field of high-efficiency silicon heterojunction solar cells. Moreover, also on the basis of the studies presented in this work, a national project called TANDEM has been

presented and ranked first in the topic of PV in the call for projects emitted in 2021 by the MiSE on the Research on the National Electric System.

The sample preparation and experiments were mostly performed at the Photovoltaic Laboratory in the Enea Casaccia Research Centre (Roma). The NiOx:Ag pellets and TiOx:W powders for e-beam and thermal evaporation were fabricated by Prof. A. Latini from the Chemistry Department at Sapienza University of Roma. Collaborations with the Information engineering, Electronics and Telecommunications Department (DIET) at Sapienza University of Roma and with the Centre for Hybrid and Organic Solar Energy (CHOSE) in Roma have also been very fruitful.

* AMPERE is a H2020-founded project with the scope of developing an EU innovative and sustainable manufacturing full-scale automated industrial pilot line, to produce heterojunction technology (HJT) silicon solar cells and modules. The final goal of the AMPERE Project is the setting-up of an innovative 100 MWp full-scale automated pilot line in production environment while preparing the next steps to 250 MWp and the GWp scale.

** The MiSE-ENEA Agreement on Research of the national electric system is a 3-year renewable project with the aim of developing high efficiency solar cells and new photovoltaic systems and architectures, including innovative solar cells with a perovskite absorber, tandem silicon-based solar cells, innovative materials and solutions for building integration and agrivoltaics.

References to Chapter 1

[1] IEA (2021) “Global Energy Review 2021”, IEA, Paris - https://www.iea.org/reports/global-energy-review-2021

[2] IRENA (2020), “Renewable Power Generation Costs in 2019”, IRENA, Abu Dhabi - https://www.irena.org/publications/2020/Jun/Renewable-Power-Costs-in-2019

[3] Renewables 2022 Global Status Report - REN21 - https://www.ren21.net/gsr-2022/

[4] IEA (2021), “Renewables 2021 - Analysis and forecast to 2026”, IEA, Paris - https://www.iea.org/reports/renewables-2021

[5] https://www.nrel.gov/pv/cell-efficiency.html

[6] International Technology Roadmap for Photovoltaics (ITRPV): 2016 Results and 2021 Results; itrpv.vdma.org

[7] https://www.enelgreenpower.com

Chapter 2

Silicon heterojunction solar cells working principles and efficiency limitations

In this chapter the working principles of silicon heterojunction (HJ) solar cells are described. Advantages and drawback of HJs are discussed and some of the main limitations to high efficiency are commented, supported by simulations and experiments. New trends in heterojunction structures are described and the background for the experimental work is set up. Part of the content of this chapter has been published in peer-reviewed journals ([1, 2]), has been submitted for publication and presented in international conferences ([11, 17, 19] in the List of Publications).

2.1 Basics of solar cells

Before plunging into the original experimental research at centre of this thesis, I will draw a brief introduction on the operation principles of a solar cell, and I will provide a quick overview of different cell architectures, to end up with the heterojunction structure. Parts of the descriptions are adapted from [3].

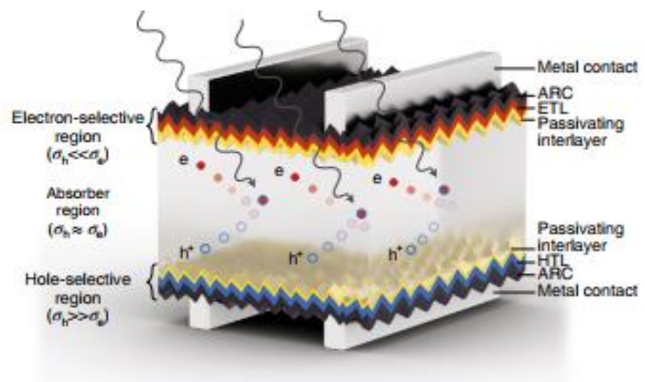

Figure 2.1 Elements of a solar cell [4].

A solar cell (see Figure 2.1) is essentially a device in which the energy of photons from the sun is used to produce electricity. The one-step mechanism makes the process very efficient. The core

of a solar cell is the semiconductor absorber, characterised by a well-defined energy gap (Eg). When light impinges on the absorber surface, photons with energy greater than Eg are able to excite electrons from the valence band into the conduction band, symmetrically generating holes in the valence band. The photogenerated charges must then be separated and driven to the terminals of the cell by two selective contacts, i.e. structures that efficiently transport only one kind of carrier while blocking the other one. The separated charges will then produce a net electric current inside the device, which can eventually flow to an external circuit.

In a conventional solar cell the separation of the carriers is produced by a p-n junction that forms between two oppositely doped areas or of the same semiconductor. At the junction, a current will build up due to diffusion of the unbalanced majority carriers; this will bring to the formation of a space charge region at the two sides of the junction where no free carriers are found, while the fixed ions will generate an electric field across the junction. Under the effect of this electric field, the free carriers will again flow through the junction in the opposite direction, until a balance between drift and diffusion will be reached. In this equilibrium conditions the Fermi levels of the materials at the two sides of the junction will line up and the conduction and valence bands will bend, as illustrated in Figure 2.2a. The potential difference between the two sides of the junction is called built-in potential (V_{bi}) and depends on the energy difference between the Fermi levels of the two materials, thus on their doping, according to eq. (1)

$$V_{bi} = \frac{kT}{q} ln\left(\frac{N_A N_D}{n_i^2}\right), \quad (1)$$

where k is the Boltzmann constant, T is the temperature in K, q is the electron charge, N_A and N_D are the acceptor and donor concentration of the two semiconductors and n_i is the intrinsic carrier concentration at equilibrium.

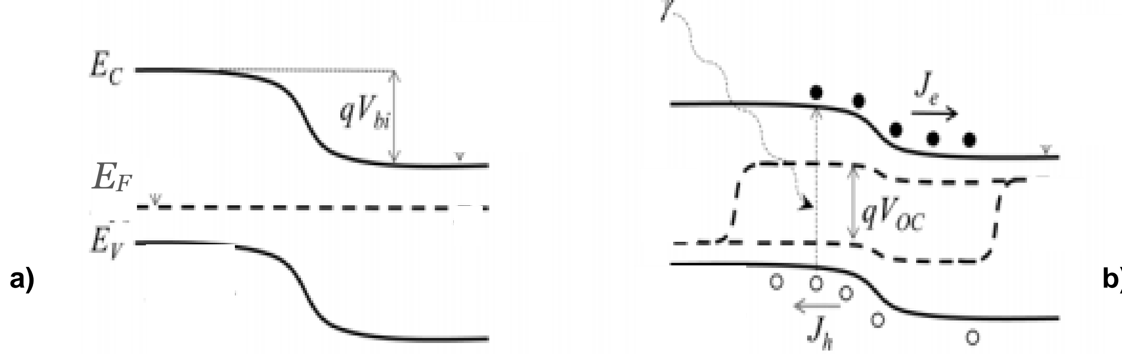

Figure 2.2 Energy band diagram of a p-n junction at open circuit a) in thermal equilibrium and in the dark and b) under illumination. E_c and E_v are the energies of the conduction and valence bands, while J_e and J_h are the electron and hole currents, respectively.

When the cell is illuminated, new electrons and holes will be photogenerated in the absorber, with excess concentrations Δn and Δp, respectively, and the equilibrium Fermi level will split in

two quasi-Fermi levels for the two distributions of carriers, namely E_{Fn} and E_{Fp} (see Figure 2.2b). When the cell is kept open-circuited, photogeneration is counterbalanced by recombination, and the steady-state excess carrier concentration determines the maximum voltage that can be established at the edges of the cell, i.e. the open-circuit voltage (V_{OC}) defined by:

$$V_{OC} = \frac{E_{Fn}-E_{Fp}}{q} \quad , \tag{2}$$

where E_{Fn} and E_{Fp} are defined by

$$n = n_0 + \Delta n = N_D \exp\left(\frac{E_{Fn}-E_c}{kT}\right) \tag{3a}$$

$$p = p_0 + \Delta p = N_A \exp\left(\frac{E_{Fp}-E_v}{kT}\right) \tag{3b}$$

and E_C and E_V are the energy of the conduction and valence band edges, respectively.

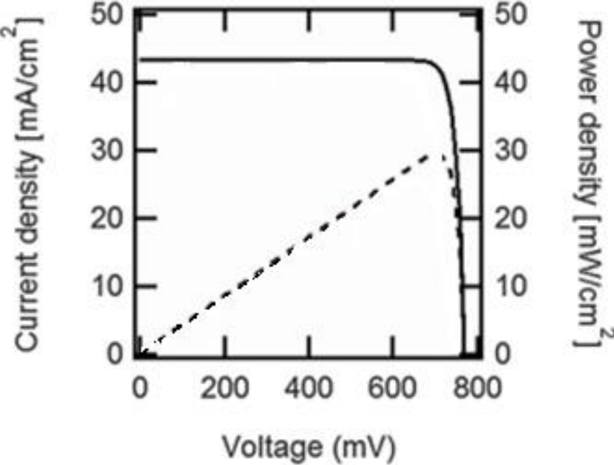

Figure 2.3 Current density (continuous black line) and power density (dashed black line) vs voltage for the ideal crystalline silicon solar cell with a 110 µm-thick silicon absorber (adapted from [3]).

When the cell is connected to an external circuit a current will flow, which will reach a maximum value (J_{sc}) in short-circuit conditions, when the concentration of carriers, and hence their recombination, is low. The maximum power that can be extracted from the cell occurs at the trade-off between current and voltage simultaneous production, indicated as J_{mpp} and V_{mpp}, respectively; these latter values are used to define the cell fill factor (FF) as

$$FF = \frac{J_{mpp}V_{mpp}}{J_{sc}V_{OC}} \,. \tag{4}$$

The balanced combination of these three parameters defines the cell final power conversion efficiency

$$\eta = V_{OC} J_{sc} \cdot FF \;. \tag{5}$$

Figure 2.3 depicts the current density and power density characteristics as a function of voltage for the ideal c-Si solar cell. Silicon, with its band gap of 1.12 eV well matched to the solar spectrum, could theoretically achieve a maximum efficiency of 29.4%, with a highest obtainable J_{sc} value of 43.3 mA/cm^2, a maximum V_{OC} of 760 mV and a maximum possible fill factor of 89.3%. With respect to other photovoltaic technologies, silicon solar cells employ a stable, non-toxic and abundant absorber material, which has contributed to the constant technological progresses that bring to a new efficiency record almost every year.

2.2 Crystalline-silicon solar cell structures

Since the first reported solar cell in 1941, the PV technology has followed many evolution steps. The first traditional structure of a silicon solar cell was the diffused n^+pp^+ homojunction, often referred to as BSF (back surface filed) [5] and sketched in Figure 2.4a. It featured a high concentration of diffused dopants near the two surfaces of a bulk p-type crystalline silicon (c-Si) wafer. Both surfaces of the silicon wafer are textured to obtain excellent antireflection and light-trapping properties, but the structure typically suffers from strong recombination losses at the back contact. This technology reached a record PCE of 20.3% in 2016 [6] and has represented an industrial standard for decades thanks to its low production costs.

Its ideal evolution was to restrict the diffused p+ region to a small fraction of the total back area and passivating the rest with a suitable insulating material, such as silicon oxide, aluminium oxide and silicon nitride, or a combination of them. This structure, sketched in Figure 2.4b, is known as PERC (Passivated Emitter and Rear Cell), which was further optimised as PERL (Passivated Emitter, Rear Locally-doped) or PERT (Passivated Emitter, Rear Totally diffused), or generally PERX [7]. The obtained benefits are an almost ideal back surface mirror and the prevention of recombination. PERC solar cells started to emerge in production since 2012 and are actually dominating the production market (see Figure 1.3) with assessed efficiencies around 25% [8].

The further cell concept was the silicon heterojunction cell (SHJ), based on two essential innovations: an excellent surface passivation achieved with a layer of hydrogenated amorphous silicon, which benefits from a lower deposition temperature (~250°C) with respect to the diffusion process, and the presence of electron-selective and hole-selective contact layers, that eliminated the expensive and complicated steps involving sub-millimetric masks (see Figure 2.4c). This permitted to obtain record V_{OC} values of 750 mV [9]. The subsequent improvement involved the elimination of the metal grid on the front and the collection of both carriers at the back by means of interdigitated back contacts (IBC), which had been already proposed for concentrating cells [10]. Passivation and antireflection are obtained at the front surface by a combination of silicon oxide and silicon nitride, also accompanied by a lightly-diffused n-type layer (see Figure 2.4c). This architecture has achieved efficiencies of 26.7% [11].

Structure	Features	Actual record
a) Al-BSF (p c-Si)	metal finger front contact passivation and antireflection diffused electron contact silicon wafer diffused hole contact metal back contact and reflector	20.3 % [6]
b) PERC (p c-Si)	metal finger front contact passivation and antireflection diffused electron contact silicon wafer diffused hole contact passivation metal back contact and reflector	25.0% [8] PERC
c) SHJ (n c-Si)	metal finger front grid transparent conductive oxide hole contact passivation silicon wafer passivation electron contact transparent conductive oxide metal back contact and reflector	26.3% [9]
d) HJ-IBC (n c-Si)	transparent conductive oxide passivation silicon wafer passivation electron contact stripe hole contact stripe metal back contacts for holes metal back contact for electrons	26.7% [11]

Figure 2.4 Schematic of standard silicon solar cells structures, with the characteristic features and record efficiencies. a) Al-diffused silicon homojunction (BSF). Electrons and holes generated in the textured p-type silicon wafer are extracted via phosphorus-doped (front) and aluminum-doped (back) regions. The front surface is passivated with hydrogenated amorphous silicon nitride, which acts simultaneously as antireflection coating. Aluminum is employed as back contact and serves as a dopant source during firing. b) Localized rear contact solar cell with dielectric rear surface passivation (PERC). Aluminum doping from the back contact into the silicon wafer is confined to the small openings in the rear passivation layer. c) Silicon heterojunction cell (SHJ). The front and rear surfaces of the n-type silicon wafer are passivated by an intrinsic hydrogenated amorphous silicon layer (a-Si:H). Contact for holes and electrons is established by a boron-doped p-type and a phosphorus-doped n-type hydrogenated amorphous silicon on the front and rear, respectively. Lateral transport of holes at the front toward the silver finger grid is achieved via an indium-oxide-based transparent electrode which simultaneously acts as antireflection coating. d) Interdigitated-back-contact cell (IBC). Both electrons and holes are extracted through the rear side via locally-diffused phosphorus and boron stripes that are contacted to individual metal stripes via local openings in the dielectric passivation layer. Adapted from [3].

As introduced in Chapter 1, the HJ technology is currently entering mass production, thanks to the massive research on the topic that has permitted a constant improvement of the technology. The market is actually dominated by the PERX technology, which actually has reached a record efficiency of 24.5% [12] and offers a low-cost cell production process. However, a more relevant parameter to describe costs is the levelised cost of energy (LCOE), given in units of $/kWh, which takes into account not only the cost to produce, but also to operate a photovoltaic complex system. With such an evaluation, new cell concepts with high efficiencies can possibly become economically convenient even if the production process may result more complicated. HJ solar cells have been studied since 1974 [13], and the following years have seen many investigations on the transport mechanisms and band discontinuities at the interfaces [14-16]. In 1992 the HJ cell efficiency became comparable to that of classical homojunction cells thanks to the adoption of the HIT concept (heterojunction with intrinsic thin layer) [17]. The efficiencies of HJ cells continued growing even on full-area cells, up to 25.6% [18] on 143.7 cm^2. The current world record belongs to Longi, with a 26.5% efficient HJ on a 274.4 cm^2 p-type silicon wafer [19].

Following these technological trends, we have decided to focus our research on heterojunction solar cells, exploring emerging ideas to improve efficiency and sustainability.

2.3 Silicon heterojunctions: working principles and limitations

2.3.1 Structure of the standard HJ solar cells

The basic solar cell structure, as already mentioned, is constituted by a p-n junction created by doping the same material (crystalline silicon) with different atoms. The structure is called a *homojunction* because the junction is formed between portions of the same semiconductor material. On the other hand, a *heterojunction* owes is name to the fact that it contains different semiconductor materials, which constitute the absorber (c-Si) and the selective contacts (a-Si:H). As described in Chapter 2.2, the heterojunction concept solved simultaneously the problem of passivation and of contact selectivity. A silicon HJ is usually manufactured as follows.

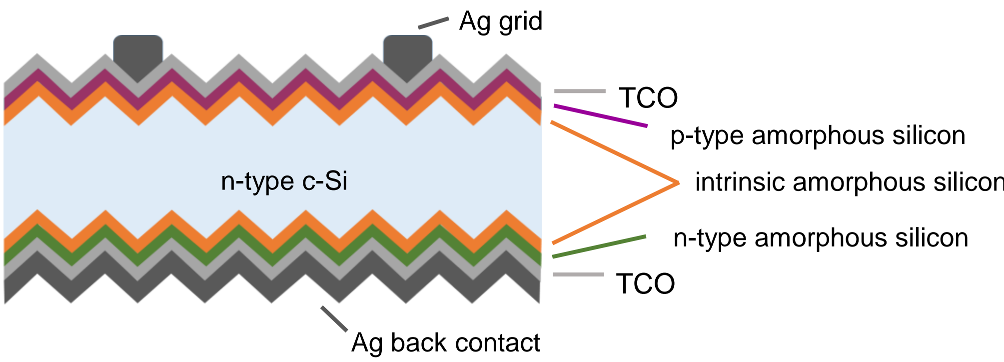

Figure 2.5 Structure of a traditional c-Si heterojunction.

The substrate is constituted by an n-type c-Si wafer, usually mono-crystalline Czochralsky (CZ) or Floating Zone (FZ) that are characterised by low bulk defect densities that typically correspond to 1-5 Ω·cm resistivities. The wafers are textured on both sides by a wet anisotropic etching procedure that produces random pyramids of ~2-5 μm height and are cleaned by a standard procedure (RCA) which removes organic and metal impurities form the surface of the wafer, and leaves it covered with an oxide layer that shall be removed before further processing.

The wafer is then passivated on both sides by intrinsic amorphous silicon layers (i-a-Si:H) deposited by plasma-enhanced chemical vapour deposition (PECVD) in silane (SiH_4) and hydrogen (H_2) plasma at a typical temperature of 180-200°C. The a-Si:H layers ensure the saturation of the c-Si dangling bonds with hydrogen, and reduce recombination.

On the front (illuminated) side, a p-doped a-Si:H (p-a-Si:H in the following) (or n-type a-Si:H depending on the film conductivity) layer is also deposited by PECVD after the addition of diborane (B_2H_6) to the base gas mixture, while on the back contact a layer of n-doped a-Si:H (n-a-Si:H) is deposited by PECVD with phosphine (PH_3) gas. These films constitute the selective contacts for the two carriers. Both sides of the device are then covered with a film of transparent conductive oxide (TCO) usually deposited by sputtering, characterised by high transparency and high conductivity to ensure lateral transport. Finally the front TCO is contacted by a screen-printed metallic grid on the illuminated side and by a full-area metallic film on the back as external contacts.

2.3.2 Working principles

The working principles of the standard heterojunction based on n-type crystalline silicon substrates and amorphous silicon intrinsic and doped layers can be explained observing the band diagram of the structure in the Anderson approximation [20], sketched in Figure 2.6.

The crystalline silicon absorber is sandwiched by two similar stacks of layers on the two sides. Its thickness should be smaller than the diffusion length of the carriers, to ensure that they can reach the opposite sides. At these interfaces, the passivating intrinsic amorphous silicon layers ensure the passivation of the dangling bond thanks to their high hydrogen content. The application of these layers permits decoupling the c-Si absorber from the defect states at the surface of the metal electrode, as happens also in homojunctions, reducing minority carrier recombination. The thickness of the intrinsic amorphous layers must be a trade-off between passivation and carrier transport.

The p- and n-doped amorphous silicon layers have a principal function of producing the c-Si band bending and inducing the p-n junction inside the bulk absorber. Crystalline silicon has an energy gap of 1.12 eV and an electron affinity of 4.05 eV, while the same quantities for amorphous silicon are 1.72 eV and 3.9 eV, respectively. As a consequence of the large bandgap of the a-Si:H layers, two barriers appear at the conduction and valence band equal to ΔE_v=0.45 eV and ΔE_c=0.15

eV, respectively. The doping of the amorphous layers determines their work function values: the high work function of the p-a-Si:H pushes its Fermi level towards the c-Si valence band, while the low work function of the n-a-Si:H pushes its Fermi level towards the conduction band. However, due to the high amount of defects in the layers, their doping efficiency stays considerably lower than that of c-Si, keeping the Fermi levels of the doped a-Si:H quite distanced from the respective valence or conduction band. From this picture it is clear that the p-n junction is not located at the heterointerface between c-Si and a-Si:H, but rather it is induced inside the c-Si. In this sense it would be more correct to speak about a *heterostructure* and not about a heterojunction.

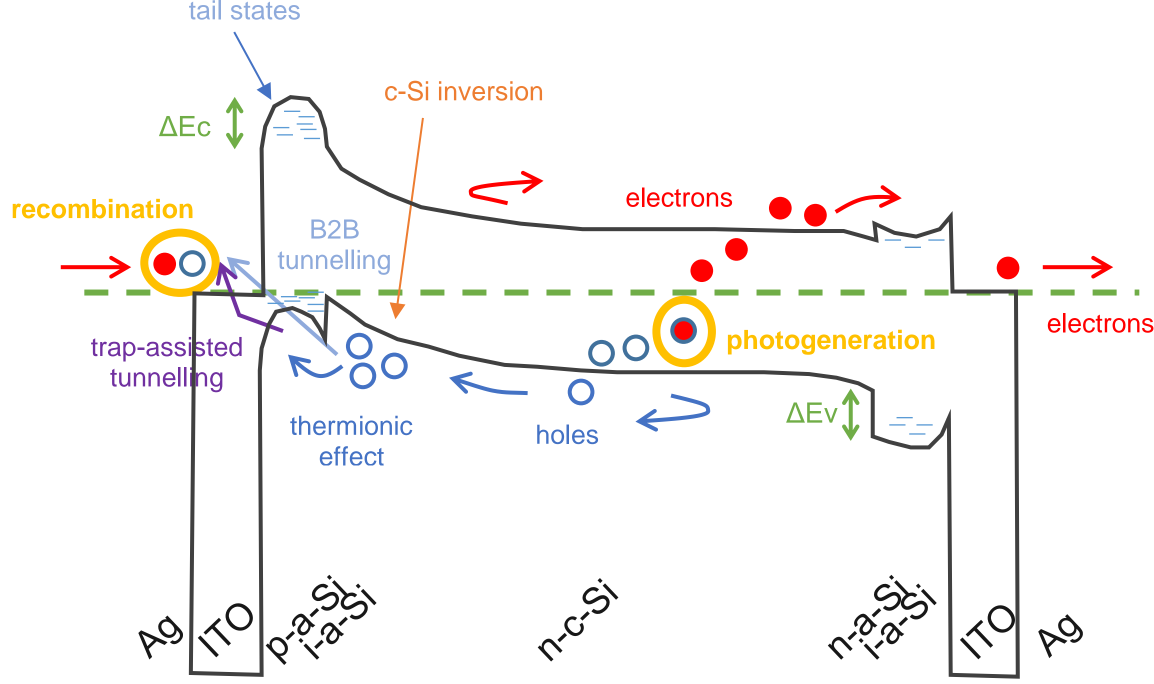

Figure 2.6 Band diagram at equilibrium of a standard heterojunction based on n-type c-Si and a-Si:H layers. The carriers photogenerated inside the absorber are separated by the electric field induced inside the c-Si and recombine at the electrodes.

The doped layers also act as “semi-permeable membranes” [21] as they allow the passage of only one type of carrier. This is enabled by the different conductivity that the doped layers present to the passage of carriers: electrons can easily move inside the n-a-Si:H film, while the transport of holes, which are minority carriers in the layer, is strongly limited by recombination. The opposite applies for electrons inside the p-a-Si:H film. The ΔEv and ΔEc barriers created at the interface of the c-Si absorber further impede the passage of holes from the absorber to the p-doped a-Si:H layer and of electrons to the n-doped a-Si:H layer, respectively. This prevents recombination in the amorphous layers, resulting in a more efficient exploitation of the photogenerated carriers and thus in a higher extracted photocurrent [22]. By these mechanisms the doped layers provide the necessary carrier

selectivity at the two sides of the heterostructure. Many works show that in principle heterojunctions provide better carrier selectivity than homojunctions [23].

The last, but not less important, function of the doped a-Si:H layers is to ensure the charge transport towards the TCO. TCOs are n-type semiconductors with a high bandgap and a work function typically ranging from 4.2 to 4.8 eV. Thus a work function difference is present between the TCO and the adjacent doped amorphous layers, which induces a band bending opposed to that of the c-Si. Due to the metal-like nature of the TCO films, which are degenerate semiconductors, they can form a Schottky-like contact with the doped a-Si:H layers if a depletion within the amorphous film occurs, otherwise they form a tunnel contact. At the p-contact the electric field, that is distributed along the c-Si wafer and has a tail into the a-Si:H film, promotes thermionic emission of holes from the absorber to the emitter over the barrier generated by the work function differences, then trap-assisted tunnelling through the tail states in the a-Si:H layer or band-to-band tunnelling allow the transfer of holes from the p-a-Si:H to the TCO, where they recombine with electrons flowing through the external circuit. At the n-a-Si:H interface, the small conduction-band offset on the n-contact does not prevent electrons from reaching the rear electrode, as it can be overcome by a low thermionic effect if an accumulation at the c-Si interface occurs.

The front layers determine the amount of radiation that will actually reach the absorber. The high bandgap of TCOs (around 4 eV) ensure a high transmittance, while the small bandgap of the amorphous layers produces an absorption of the radiation with energy higher than the bandgap. In this sense, the thickness of the doped amorphous layers must be a trade-off between transparency, carrier transport and passivation protection. If the thickness is too high, the photons absorbed in the amorphous layer will cause a reduction of the photogenerated current [24]. Moreover, if the intrinsic/amorphous bilayer is too thick, the electric field will mainly drop inside this bilayer, reducing the inversion inside the bulk c-Si and consequently increasing the potential barrier at the heterointerface and hindering hole transport. On the other hand, if the doped layer is too thin it will not provide a protection to the underlying passivating layer, for example against the sputtering damage that the structure should necessarily undergo during TCO deposition. The illuminated state of the solar cell is described by the quasi-Fermi levels (QFL) for electrons and holes (E_{FC} and E_{FV}, respectively), which difference determines the V_{OC} of the cell.

The role of the TCO, beyond carrier extraction, is to ensure a good lateral conductivity of the charges and a low resistivity with the metal contact. Moreover it has to be optically matched (via a suitable combination of refractive index and thickness) with the adjacent layers, so to provide optimal light coupling at the front and internal reflection at the rear. The maximization of optical absorption is simultaneously accomplished by the c-Si surface texturing [25], which is able to lower the effective surface reflectivity from 30% to 5-8%.

Finally, the TCO is contacted to the external circuit by a metal electrode, which is deposited in form of a grid on the illuminated side or on both sides if bifaciality is required. In general, the TCO always needs a thermal annealing step between 200°C and 300°C to exploit its best features. The

same annealing step helps the recovery of passivation, which is usually damaged during the TCO deposition via sputtering. The metal electrodes are formed by low-thermal curing screen-printable silver pastes that are costly and less conductive with respect to those used in the conventional homojunctions. The low temperature applicable to HJs implies the use of costly electrically-conductive adhesive tapes to connect the cells within the module instead of the conventional low-cost and high-reliability tin-based soldering procedure, thus reducing the FF of the module. Innovative concepts, such as the shingling method, have recently been introduced in module manufacturing of SHJ to partially overcome this issue.

2.3.3 Advantages and drawbacks of HJs

Silicon heterojunction solar cells owe their success to many unique characteristics with respect to homojunctions. From an industrial point of view, the great advantage of this technology is represented by the very low thermal budget used in the process chain (below 250°C) that strongly reduces the stress and the unvavoidable contamination of c-Si wafer during the thermal treatment at high temperature (at least 900°C) needed to overdope the c-Si to form the diffused junction (Fig. 2.7). The absence of thermal stress allows the employment of thinner wafers, thus consuming less material. Both aspects contribute to the lower production cost of heterojunctions.

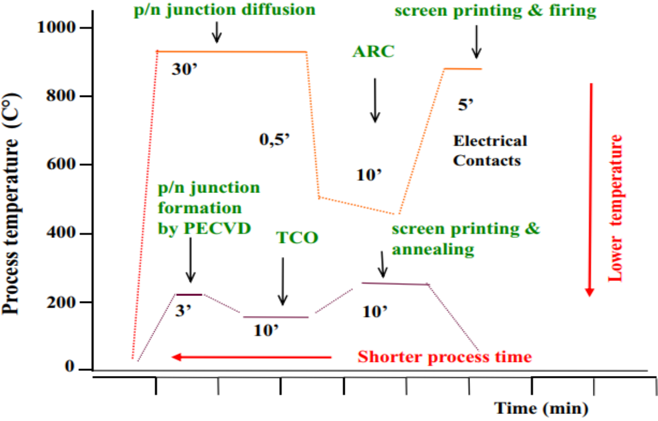

Figure 2.7 Estimated thermal budget and process time for conventional c-Si technology (top curve) and SHJ technology (bottom curve). [28]

The main factor that brings heterojunctions to record efficiencies is the effective passivation of the c-Si surfaces that, together with the low bulk contamination due to the absence of diffusion, allows obtaining very high V_{OC} values. In homojunctions the diffusion process generates numerous recombination centres that reduce the Fermi-level splitting. Moreover the QFL join at the metal contacts, where a high concentration of defects is again present, so that the carriers recombine where they should be extracted. On the contrary in a heterostructure the QFL splitting can almost

extend as much as the c-Si gap, and the QFL join inside the amorphous layers, where only one type of carrier is present, leading to a higher V_{OC}. HJ devices also have a lower temperature coefficient than homojunctions (-1.58 mV/°C instead of -2.5 mV/°C) which is advantageous for in-field applications. The wide use of n-type c-Si wafers avoids light-induced degradation processes connected with boron-oxygen complexes present in p-type wafers [26, 27], while the use of thin wafers reduces recombination losses inside the bulk.

There are still a few drawbacks on HJ that should me mentioned. The use of n-type wafers has initially brought to higher costs, which however are actually reducing. High-temperature processes degrade the intrinsic and doped a-Si:H layers, and this implies that technological steps commonly performed in homojunctions must be replaced by lower temperature ones. For example, the external metal contact must be obtained by low-temperature sintering screen-printable pastes that are less conductive and more expensive than silver. Soldering at high temperatures must be avoided, so more expensive conductive ribbons and tapes have to be used. The doped a-Si:H layers have low conductivity, thus they require the conjunction with TCOs to increase lateral transport. The most widely used TCO, ITO, contains an expensive and rare material, indium, which should be avoided. However, most of these drawback are currently finding more and more efficient solutions, and are balanced by the higher efficiencies that can be reached.

2.3.4 Fill factor limitations due to the TCO work function and an indirect method to evaluate them [1]

As mentioned, the TCO is necessary to overcome the issue of low conductivity of the a-Si:H doped layers and to reduce the specific contact resistivity of the metal contact with both emitter and base layers. On n-type a-Si:H base contacts, the TCO does not represent a special limitation because its role is basically that of ensuring an equipotential surface. On the contrary, on a p-doped emitter the situation is different, because in this case the contact between TCO and emitter works as a tunnelling contact. For the tunnelling to be effective, the barrier at the TCO/emitter interface must be very thin, and to this end the emitter should be heavily doped to avoid a large emitter depletion, which would reduce the tunnelling mechanism.

In principle, the best solution would be the use of two different degenerate TCO layers: one with a high work function ($\Phi \approx 5.2$ eV) on the emitter side and another one with a lower work function ($\Phi \approx 4.1$ eV) at the base contact, in order to respectively collect holes and electrons without affecting the Fermi level position at the edges of the inverted c-Si. This situation is depicted in the simulated energy band distribution reported in Figure 2.8(left) [29]. Nevertheless, it is very difficult to find in practice a degenerate TCO with a work function as high as 5.2 eV.

A more realistic case is simulated in Figure 2.8(right), where the TCO is assumed to have $\Phi=4.4$ eV on both sides of the HJ cell, as typically obtained with ITO. In this condition the p-type a-Si:H emitter depletes, due to the downward shift of the fermi level at the edge of TCO and emitter layers.

Also, on the base contact, the Φ_{TCO} higher than the Fermi level position in the n-doped a-Si:H layer induces the formation of a small barrier at the n-a-Si:H/TCO interface. In this particular case this barrier is not as critical as the one formed at the emitter side but, if further increased, it can promote depletion up to the n-c-Si, leading to the formation of a larger barrier against electron collection.

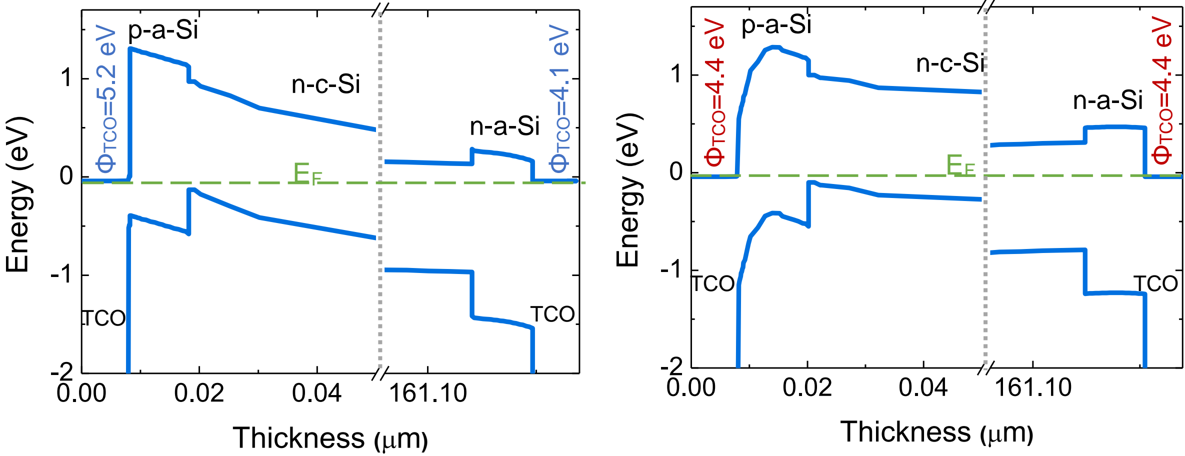

Figure 2.8 Numerical simulation of the energy band distribution in the dark at 0 V bias of a traditional HJ solar cell with different TCOs at the edges. Left: “ideal” situation in which the TCOs at the front and back side have a high (5.2 eV) and low (4.2 eV) work function, respectively. Right: “real” situation in which the TCOs have an equal work function of 4.4 eV. A depletion at both the emitter and base contacts can be seen.

The simulated light J-V characteristic of a HJ with Φ_{TCO} = 4.4 eV on both sides is reported in Figure 2.9a (blue line) and compared to that of an ideal cell (purple line) with performances very close to the actual HJ record cell (see [1] for details). The J-V characteristic is clearly affected by an s-shape that reveals a barrier against carrier collection. To understand where this barrier is located, we also performed a numerical simulation of the J-V characteristic related to the bare rear side of the same cell, obtained after removing the emitter, and shown in Figure 2.9b (black line). The graph shows a rectifying behaviour that remains almost unchanged even after increasing the doping of the n-a-Si:H layer (orange line). The only way to obtain an ohmic behaviour is to reduce the Φ_{TCO} to 4.1 eV (green line). Thus, the undesired s-shape on the J-V characteristic in Figure 2.9 can be also due to the base contact.

The effect of this barrier on the fill factor value has been simulated and the FF trend as a function of Φ_{TCO} is reported in Figure 2.9c for two doping levels of the n-a-Si:H layer, namely 7×10^{17} cm^{-3} and 1.7×10^{18} cm^{-3}, corresponding to doping activation energies of 0.18 eV and 0.14 eV, respectively. The simulations suggest that the higher the Φ_{TCO}, the lower the FF, and the higher the doping level, the lower the FF decrement with increasing Φ_{TCO}. A higher doping can mitigate the FF reduction caused by the higher work function value, thanks to the higher carrier density.

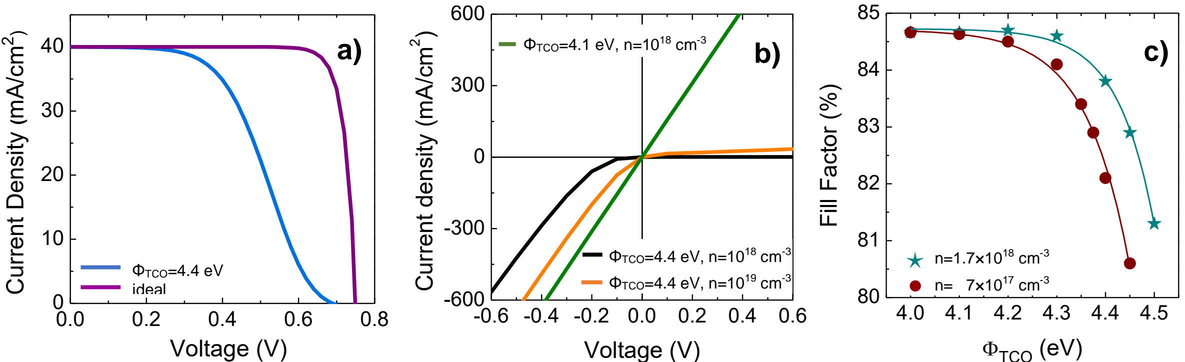

Figure 2.9 a) Simulated light J-V characteristics of an "ideal" HJ solar cell (purple line) and of a cell having TCOs with non-optimal Φ values on both sides (blue line), which bring to an s-shape. b) Simulated light J-V characteristics of the bare base contact for different values of Φ_{TCO} and n-a-Si:H doping (n). The base contact is ohmic only when the Φ_{TCO} is low. c) Simulated trend of the fill factor as a function of Φ_{TCO} for two values of the n-a-Si:H doping. The fill factor value saturates at 84.7% for Φ_{TCO} below 4.1 eV.

2.3.5 Fill factor limitations due to hidden barriers at the base contact and a method to detect them [1]

When we deal with a "good" HJ solar cell, i.e. with a FF value around 80%, the above-mentioned barrier induced by a too high Φ_{TCO} at the back contact is a small contribution and can be hidden by coexisting resistive effects. In fact it can be almost overcome by thermionic effect at room temperature. However, when we lower the temperature, the barrier can no more be surmounted. Guided by this observation, we developed a method - described in the following - based on low-temperature measurements to evaluate the detrimental effect of Φ_{TCO} even on "good" cells, which limits the FF and hinders the achievement of best performances.

We produced a HJ solar cell with the standard structure based on an n-type c-Si substrate and intrinsic and doped a-Si:H layers, completed by two identical layers of ITO on the two sides. First, the base contact of the structure was isolated from the whole cell by chemically removing the emitter side and contacting the c-Si wafer with a proper ohmic contact with an InGa eutectic (see Appendix for details). The so-obtained contact thus consisted in an InGa/c-Si/i-a-Si:H/n-a-Si:H/ITO stack. Then the J-V characteristic of the contact was measured at various temperatures between 80 and 350 K, and the curves are reported in Figure 2.10.

The base contact is (almost) ohmic only at a moderate temperature of 350 K (red line), while it behaves nonlinearly at room temperature (green line) and it is strongly rectifying at the lowest temperatures (grey and blue lines). Referring to the numerical simulation of the base contact reported in Figure 2.9b, the nonlinear behaviour of the J-V curve at room temperature suggests the presence of a barrier against electron collection due to a too high Φ_{TCO}.

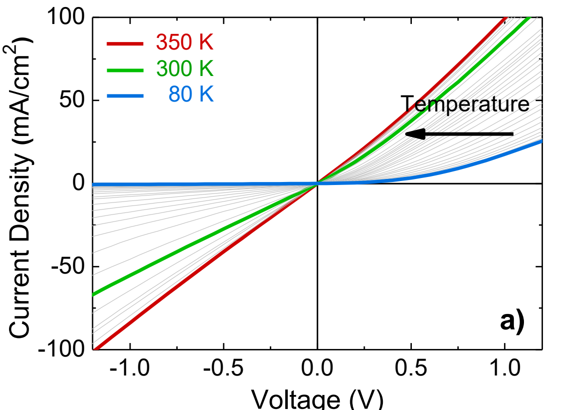

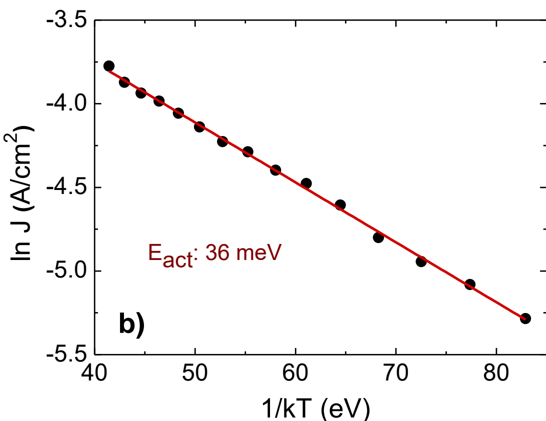

Figure 2.10 a) Dark J-V characteristics of the base contact of the HJ solar cell sample measured at various temperatures. A transition from a non-linear to a linear behaviour is evident when increasing the temperature. b) Arrhenius plot evaluated from the J-V characteristics in (a) at 0.4 V.

From the observation of the curve bundle in Figure 2.10a we can account for an activation process from a non-linear behaviour to a linear one. The characteristic activation energy (E*) of this process can be evaluated by an Arrhenius plot (see Figure 2.10b) of the current density data measured at a bias voltage of 0.4 V, which corresponds to the forward bias working conditions of the base contact of the solar cell. For this sample, an activation energy of 36 meV was obtained.

To exploit the meaning of this number, we performed a numerical simulation of J-V curves and corresponding Arrhenius plots for different base contacts which differed only in the Φ_{TCO} value (varied from 4.0 to 4.6 eV). The resulting E* values are plot in Figure 2.11a (black dots) and are fitted by an exponential curve (red curve). The line at kT=26 meV corresponding to room temperature is drawn as a reference. When E* is lower than this value (i.e. when Φ_{TCO} is lower than ~4.23 eV), then a linear behaviour of the base contact can be ensured at least at room temperature. Instead, if the E* value is higher than 26 meV, the J-V behaviour of the base contact will always be affected by non-linearity and its resistivity will be definitively lower than the expected value. In the particular case relative to Figure 2.10, the obtained E* value of 36 meV (green star in Figure 2.11) confirms that the base contact is affected by nonlinearity due to a $\Phi_{TCO}\approx 4.3$ eV. It is remarkable to observe that even a slight mismatch of the value at the base contact from the ideal one (4.1 eV) is sufficient to introduce a barrier to transport. This undesired effect decreases the FF of the HJ cell.

The described method is thus a powerful tool to detect possible hidden barriers at the base contact by low-temperature characterisations. The extracted E* can serve as an evaluation of the Φ_{TCO} at the base contact, which cannot be measured by direct methods because the related interface is buried inside the structure. Indeed, most of the direct measurements that can be performed on TCO films to determine their work function (for example Ultraviolet Photoemission Spectroscopy -UPS- or Kelvin Probe) are referred to the free surface of the TCO layer. Moreover, it is very difficult

to evaluate the correct Φ value of air-exposed ITO by UPS [30] even after surface cleaning [31]. Furthermore, the TCO film growth is influenced by several parameters, like the substrate nature and morphology [32, 33] or the layer thickness [34], that can modify the film properties during the growth and, in turn, modify the film work function. Consequently, the mentioned techniques can only assess Φ_{TCO} at the free surface. All these reasons give a clear indication of the relevance of the described method to obtain an indication of the TCO's work function at the significant interface, i.e. that with a-Si:H.

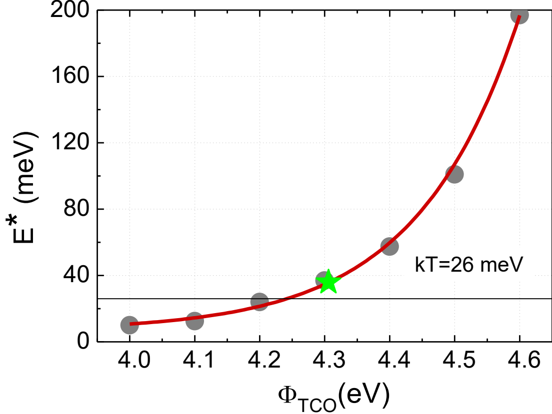

Figure 2.11 Relationship between the characteristic activation energy E* of the non-linear/linear behaviour of the J-V characteristics of a heterojunction base contact as a function of the TCO's work function. The black dots (and the resulting red curve fit) are calculated from simulations using different Φ_{TCO} values. The green star is referred to a particular experimental case. The black line at E*=26meV corresponding to room temperature is drawn as a reference.

2.3.6 Fill factor limitations due to barriers at the emitter contact and a method to detect them [2]

As already mentioned in Section 2.3.2, the holes collection takes place at the TCO/p-a-Si:H/i-a-Si:H/n-c-Si heterostructure. Here the contact selectivity is ensured by the electric field that allows the jump over the valence-band barrier at the i-a-Si:H/p-a-Si:H/c-Si interface by thermionic emission (see Figure 2.6). At this interface, the higher the built-in voltage, the better the collection of holes. The valence band offset ΔEv represents a barrier to thermionic emission and to collection probability, so it plays a relevant role in the determination of the FF of the solar cell. Clearly, the impact of the barrier is more evident under illumination, because the holes generated into the n-c-Si absorber must cross the barrier (see Figure 2.12b) to be collected by the emitter layer and produce a current available for the external circuit. On the other hand, the role of the valence band offset is less relevant when the cell is in dark conditions and forward bias because of majority carrier injection into the oppositely doped region (see Figure 2.12a). This asymmetry implies that, at equal voltages, the injection current is slightly lower under illumination than in the dark, which in turn brings to an overlap in the light and dark J-V characteristics (see Figure 2.12c). So, if an overlap is

detected between the light and dark characteristics of a cell, this can be the evidence of the presence of a barrier at the valence-band interface.

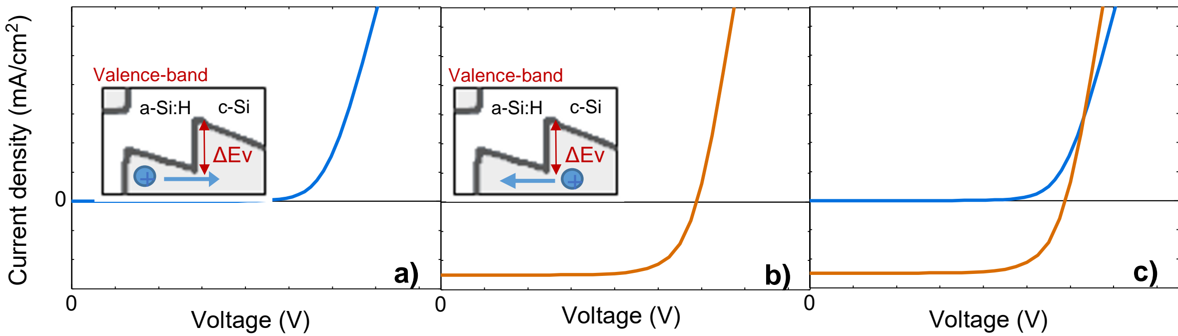

Figure 2.12 Schematic explanation of the different influence of the valence-band barrier on the a) dark and b) light characteristics of a HJ cell, resulting in c) the crossing of the two curves.

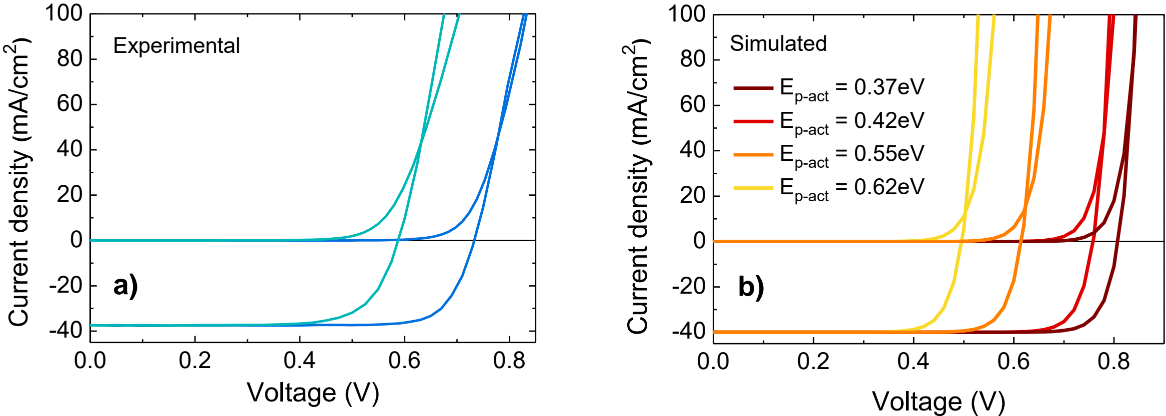

Figure 2.13 Light and dark J-V characteristics at RT of HJ solar cells showing the crossing of the two curves. a) Experimental curves of different cells; b) simulated characteristics of cells having different doping activation energies of the p-a-Si:H layer. The figures evidence the crossing of all couples of curves.

The predicted crossing is actually observed experimentally, as shown in Figure 2.13a for two cells having different values of Φ_{TCO} and doping of the p-a-Si:H layer (see [2] for details). As the transport at the p-contact depends also on the doping level of the p-a-Si:H layer ($E_{p\text{-}act}$), light and dark J-V characteristics in HJ cells with different $E_{p\text{-}act}$ values are simulated and are reported in Figure 2.13b. Each couple of curves confirms the crossing, which takes place at a higher forward bias voltage as the $E_{p\text{-}act}$ value decreases, while the corresponding FF values vary between 79% and 85.5%. When the HJ cell reaches very high V_{OC} values, corresponding to $E_{p\text{-}act}$ values below 0.2 eV, the crossing between the two curves almost disappears, meaning that the cell is no more affected

by any built-in voltage lack due to the valence band offset, which in the simulations is kept at a constant value of 0.45 eV. Even though in practice it is very difficult to achieve a doping value on a p-a-Si:H layer corresponding to $E_{p\text{-}act}$=0.2 eV, the crossing voltage can be assumed as a useful indication of the overall cell quality.

2.3.7 V_{OC} limitations due to edge recombination

One of the fundamental components to reach high efficiency is the open-circuit voltage (V_{oc}), which in silicon HJs is granted by the excellent surface passivation capabilities of a-Si:H films. Even if during cells production the a-Si:H deposition covers also the edges of the wafer, there can be some cases in which such edges could remain un-passivated. For example, when cells are cut in halves following the shingling concept [35] to improve the modules fill factor or at laboratory level, where it is quite common to manufacture small cells from larger wafers. This leads to a larger contour/area ratio due to the creation of cleaved edges, which can lead to higher recombination losses and thus to the reduction of the cell's V_{OC}. It would be interesting, though, to know at which dimension this effect would become important for the cell performance.

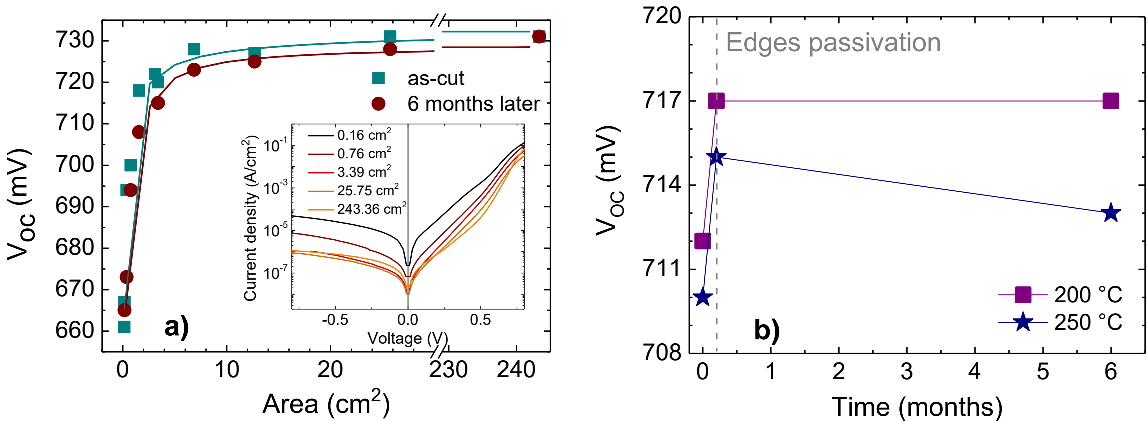

Figure 2.14 a) V_{OC} vs area of samples of different dimension cut from an M12 commercial SHJ cell with V_{OC}=731 mV. The V_{OC} decreases with decreasing dimensions of the pieces. After 6 months the trend is similar. The dark J-V characteristics of the samples (inset) shift to higher current-density values with decreasing dimensions, confirming that the V_{OC} reduction can be correlated with the increase of the recombination. b) Time evolution of V_{OC} in cut cells after edges re-passivation for two deposition temperatures of the a-Si:H film. The dashed vertical line indicates the time of the edges re-passivation.

We cut a full-size commercial c-Si HJ M2 cell with V_{OC}=731 mV in smaller pieces, both in square and rectangular shapes, down to 0.16 mm^2. We then measured the V_{OC} of all pieces and the results are reported in Figure 2.14a as a function of the sample area (green squares). Both square and rectangular cells share the same trend. It can be seen that for areas between the maximum

dimension (243 cm^2) and 25 cm^2 the V_{OC} is reduced by a negligible amount, while it sharply drops for cells of smaller sizes, reaching an absolute value of 661 mV (i.e. a 9.6% reduction) for the smallest piece. The inset in Figure 2.14a shows the dark J-V characteristics of selected cells with different areas: it can be seen that the characteristics of cells with areas within the full size and 25.5 cm^2 the curves do not differ much, while for lower areas the saturation current increases, especially in the moderate forward-bias region, denoting an increased recombination. Thus the V_{OC} reduction with decreasing sample area can be correlated with the increase of the recombination, which mainly occurs at the un-passivated edges along the cut perimeter. A similar V_{OC} trend, but with lower values, is found after 6 months (red dots in Figure 2.14a). Only the full-area cell remains unchanged, suggesting that the recombination at the edges has worsened due to native oxidation and/or ambient contamination.

We also performed a re-passivation of the edges of two small cells, by masking the exposed area and re-depositing an a-Si:H layer by PECVD on the edges. The effects on V_{OC} are reported in Figure 2.14b and show that re-passivation has an immediate recovery effect on the V_{OC}, with a beneficial increase of about 0.7 % for both tested deposition temperatures (200°C and 250°C). After 6 months, however, only the V_{OC} of the cell re-passivated at lower temperature is still stable, while the higher a-Si:H deposition temperature shows some negative effects on the time stability of re-passivation.

All in all, reducing the cell size without passivating the edges may lead to a maximum V_{OC} reduction of 10%, which has to be taken into account when working with cells of reduced dimensions.

2.4 Alternative carrier selective contacts

As we have seen, the heterojunction approach has permitted avoiding or circumventing some technological issues connected with homojunctions, such as a high thermal budget, that can stress the thinner wafer, and longer processes such as thermal diffusion, that reduce the throughput of cell production. However even the standard heterojunction architecture has been reviewed, and nowadays the research has steered towards the new concepts of “heterocontacts”, or “carrier selective contacts” or “passivating contacts” [4, 36, 37], denoting alternative materials to substitute the doped-amorphous layer counterparts. Even if all these characteristics well match also with the standard a-Si:H contacts, they actually refer to new cell approaches with new working principles. The main aim of these alternatives is the reduction of the optical losses due to parasitic absorption and Auger recombination introduced by the highly-doped a-Si:H layers and the avoidance of dangerous and toxic gases (phosphine and diborane/trimetil-boron) that complicate the industrial safety procedures and thus the whole production process. For this reason the new investigated materials have also been referred to as “dopant free” carrier-selective layers [37, 38], even if - as we shall see in the following - they sometimes need to be doped.

Actually none of these definitions completely describes the new materials: heterocontacts or carrier-elective contacts also applies to doped a-Si layers in heterojunctions, as already explained, while the use of the new material to simultaneously passivate the c-Si surface has been demonstrated not to be so efficient [39-41]. Also the dopant-free request has to be frequently dropped to obtain materials with the favourable band alignment [42]. However the definitions are commonly used to indicate selective contacts different from doped amorphous silicon.

There are two kinds of operating principles for selective contacts. The first one, sketched and simplified in Figure 2.15a, is based on the use of n-type high-work function materials as hole-selective layers, which produces a large upward bending of the bands of n-c-Si; this induces an inversion of c-Si at the interface and generates a p-n junction inside the bulk. The transport mechanism is widely discussed, and may take place via direct band-to band (B2B) tunnelling [44] or include a transfer of electrons by trap assisted tunnelling (TAT) into the deep oxygen-vacancy defect states inside the TMO [45]. Basically, the holes must cross the barrier created by the valence-band offset between a-Si:H and c-Si and then reach the degenerate TCO on the front electrode. This mechanism is very much similar to what happens in standard HJs, where the transit takes place through the tail state of p-a-Si:H. While in the case of TMOs the barrier height depends on the material's high work function, in the case of p-a-Si:H it is controlled by the doping.

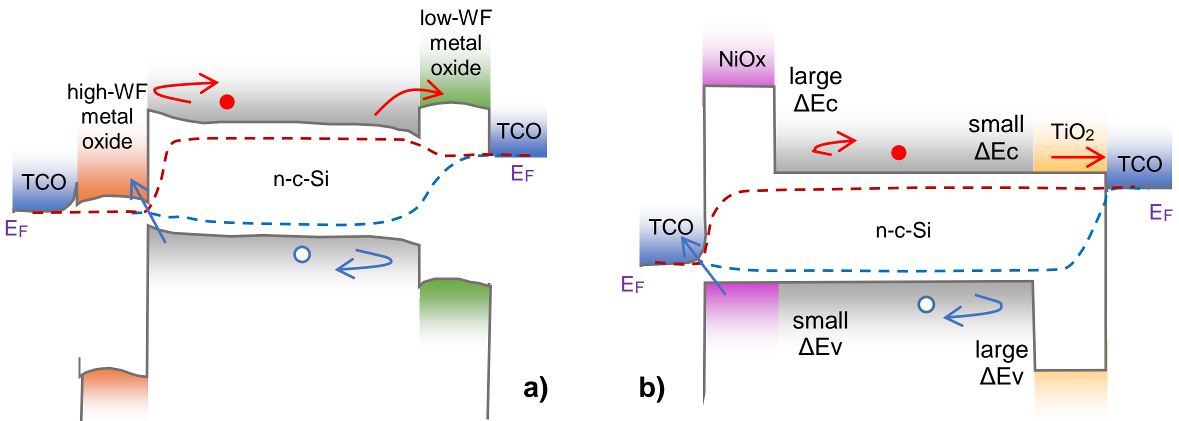

Figure 2.15 Schematic band diagrams under illumination of heterostructures implementing different selective contacts. Adapted from [43].

The second principle (see Figure 2.15b) involves materials that have a small valence- or conduction-band offsets with silicon; this essentially makes the extraction simple for one type of carrier while simultaneously creating a barrier for the other one [46].

The material of choice must have some more basic characteristics beyond the just-mentioned electrical features. It should not be doped, in order to avoid increased recombination; it should provide passivation in analogy with i-a-Si:H; it should be highly transparent to avoid parasitic

absorption losses; it should have a low deposition temperature to reduce wafer warping and strain, and thus the production cost connected to a lower material consumption; it should be deposited without the employment of toxic and flammable gases, to reduce the process complexity and ensure safety; it should be mechanically and chemically stable, to accomplish the required 25-years expected lifetime of commercial modules.

The search for materials with the mentioned characteristics is very active and lively, and many candidates have been identified for the scope. Among the hole-selective contacts we find high-work function TMOs such as n-type MoOx, WOx, VOx and p-type NiO and PEDOT, while for the electron selective contacts we find low-work function fluorides such as LiF and MgF_2 and n-type oxides such as TiO_2 [4, 37, 47]. The energy band diagrams of these and other materials are reported in Figure 2.16. Many of them have already reached very good levels of implementation in c-Si heterojunctions [38, 49-53] also thanks to the fact that they can be deposited via low-temperature processes, bringing to cost reduction and process simplification, which makes the study on heterocontacts very attractive also for the PV industry. On the contrary, other promising materials such as NiOx, fully explored in theoretical works [54], have not yet reached a full maturity [55]. However, in all cases none of the materials can withstand thermal processes above 150°C, which is currently their main bottleneck. The full exploitation of this new concept of selective contacts will thus be achieved only when materials with a resistance to thermal treatments at temperatures higher than 200°C will be found, as requested by the current most efficient production processes.

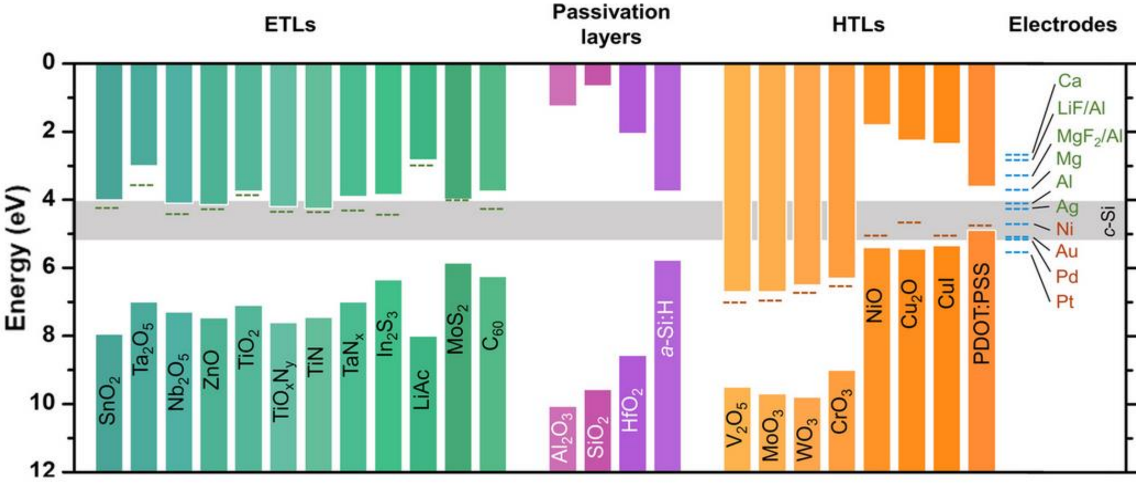

Figure 2.16 Schematic energy band diagrams for HTL e ETL materials [48].

In this thesis, we will examine the possibility of using doped NiOx and TiO_2, LiF, MgF_2 and ZnS as a hole- and electron-extracting layer. For the above-mentioned reasons, a particular attention will be directed to the investigation of their behaviour after thermal annealing treatments at 200°C.

2.5 The choice for the passivation layer

One of the sources of losses in silicon HJs is the optical absorption inside the front a-Si:H layer, that has to be kept as transparent and as thin as possible. The standard a-Si:H layer presents an energy gap of 1.7 eV and a not-negligible absorption, especially in the UV-Vis parts of the spectrum. An alternative solution can be found in amorphous hydrogenated silicon suboxide (a-SiOx:H), which will be indicated as SiOx in the following for brevity. SiOx is reported to have a larger bandgap (1.8-1.9 and a higher transparency with respect to a-Si:H. It also has a higher thermal stability (up to 250-300°C) which is due to the higher deposition temperature [56, 57].

SiOx can be deposited by PECVD similarly to a-Si:H, with the sole addition of CO_2 in the plasma mixture (see Appendix for further details). In our laboratory we optimised the deposition conditions so to obtain a very transparent material (see Figure 2.17) with high passivation performances, i.e. around 10 ms for a c-Si wafer passivated by 15 nm-thick SiOx layers on both sides. The passivation is enhanced by ~50% after a thermal annealing at 200°C for 10 minutes, and remains stable after thermal treatments up to 250°C. The best SiOx trade-off thickness between passivation and carrier transport has been evaluated in 5.5 nm, with a substrate lifetime of ~2.2 ms, which will be the standard passivation applied to the c-Si substrates used for the experiments described in the following.

In recent years we already explored the first approach to selective contacts, by applying MoOx and WOx thin films to n-type c-Si wafers passivated with SiOx [58], and we have showed proof-of-concept cells which demonstrated the compatibility of the materials with this passivation layer. So, even if it is not the mainstream choice in the literature, in this work we have used SiOx to passivate the c-Si substrates for the experiments. The first request that all the investigated materials should accomplish is thus the avoidance of damage to the SiOx layer, in order to preserve its passivation capabilities and keep the device lifetime as high as possible.

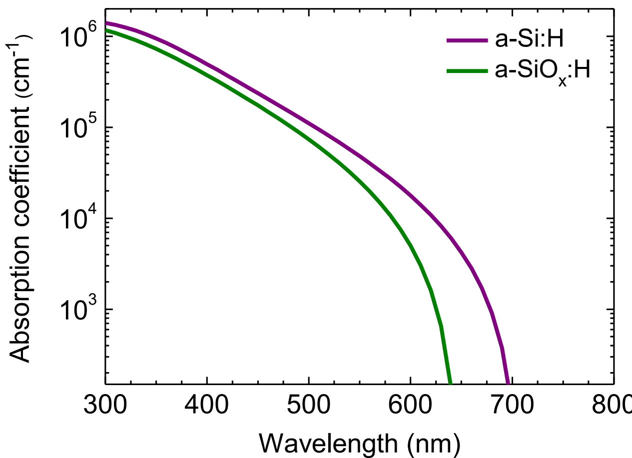

Figure 2.17 Comparison between the absorption coefficient of a-Si:H and SiOx samples deposited in our laboratory.

2.6 Summary

Heterojunction solar cells have many advantages over the homojunction original design. They possess higher efficiencies thanks to the c-Si surface passivation and show higher thermal stability. They also have a lower thermal budget that can bring to a higher throughput and lower costs. HJs are gaining an important role in the PV scenario, and have already been employed in industrial production lines. The research, however, is still looking for improved solutions, both from the point of view of more performing architectures and with the search for more suitable materials, always with an eye to cost effectiveness and sustainability.

The performances of HJ cells depend on the properties of the composing materials, and they are usually evaluated by measuring their J-V characteristics. Several parameters can contribute to lowered performances, and some of them are discussed in this chapter.

The workfunction of the TCO films used to complete the selective contacts plays a fundamental role in the cell performances, and we have simulated the effects of this parameter on the fill factor. We have also presented an indirect method to evaluate such workfunction value, which is naturally inaccessible to direct measurements. The method consists in isolating the back contact of the cell and measuring its J-V characteristic at low temperatures.

Limitations to HJ performances due to the back side of the cells are very often underestimated as they cannot be easily evaluated. We have indicated a simple method to individuate a barrier to hole transport at the emitter contact caused by a valence-band offset, consisting in the simple superposition of light and dark J-V characteristics. If the curves show a crossing, this is the evidence of a barrier to transport.

Another source of reduction of the cell performances, which is of interest for the great majority of the research community at laboratory level, comes from the V_{OC} reduction associated with the use of small-dimension cells. We have shown that the V_{OC} reduction is not negligible for dimensions smaller than 5×5 cm^2.

A recent development in the field of heterojunction solar cells involves the use of new materials for the *selective contacts*, a term that needs to be contextualised to clarify that it indicates non-silicon contacts, i.e. different from the traditional doped amorphous-silicon layers. The literature state-of-the-art shows a very rich and lively interest on the topic, with some materials having already reached a good grade of maturity. However, the main problem to be solved is the temperature stability of the materials, which is essential when coming to industrial production where thermal processes are needed for the fabrication of modules.

References to Chapter 2

[1] L. Martini, L. Serenelli, F. Menchini, M. Izzi, M. Tucci, "Silicon heterojunction solar cells toward higher fill factor", Prog. Photovolt: Res. Appl. 28 (2020) 307-320. DOI: 10.1002/pip.3241

[2] L. Serenelli, L. Martini, F. Menchini, M. Izzi, G. de Cesare, G. Condorelli, C. Gerardi, D. Munoz, M. Tucci, "Selective contacts and fill factor limitations in heterojunction solar cells", Prog. Photovolt: Res. Appl. 29 (2021) 876-884. DOI: 10.1002/pip.3418

[3] C. Battaglia, A. Cuevas, S. De Wolf, "High-efficiency crystalline silicon solar cells: status and perspectives", Energy Environ. Sci. 9 (2016) 1552-1576. DOI: 10.1039/c5ee03380b

[4] T. G. Allen, J. Bullock, X. Yang, A. Javey, S. De Wolf, "Passivating contacts for crystalline silicon solar cells", Nat. Energy 4 (2019) 914-928. DOI: 10.1038/s41560-019-0463-6

[5] J. Mandelkorn, J. H. Lamneck, "Advances in the theory and applications of BSF cells", Proc. 11th Photovoltaic Specialists Conference, 1975.

[6] K. H. Kim, C. S. Park, J. D. Lee, J. Y. Lim, J. M. Yeon, I. H. Kim, E. J. Lee, Y. H. Cho, "Record high efficiency of screen-printed silicon aluminium back surface field solar cell: 20.29%", Jpn. J. Appl. Phys. 56 (2017) 08MB25. DOI: 10.7567/JJAP.56.08MB25

[7] J. Zhao, A. Wang, M. A. Green, "24.5% efficiency silicon PERT cells on MCZ substrates and 24.7% efficiency PERL cells on FZ substrates", Prog. Photovolt: Res. Appl. 7 (1999) 471-474. DOI: 10.1002/(SICI)1099-159X(199911/12)7:6<471::AID-PIP298>3.0.CO;2-7

[8] M. A. Green, "The passivated emitter and rear cell (PERC): from conception to mass production", Sol. Energy Mater. Sol. Cells 143 (2015) 190-197. DOI: 10.1016/j.solmat.2015.06.055

[9] https://en.longi-solar.com/home/events/press_detail/id/335.html

[10] R.A. Sinton, Y. Kwark, J. Y. Gan, R. M. Swanson, "27.5% silicon concentrator solar cells", IEEE Electron Device Lett. 7:10 (1986) 567-569. DOI: 10.1109/jphotov.2013.2282737

[11] K. Yoshikawa, H. Kawasaki, W. Yoshida, T. Irie, K. Konishi, K. Nakano, T. Uto, D. Adachi, M. Kanematsu, H. Uzu, K. Yamamoto, "Silicon heterojunction solar cell with interdigitated back contacts for a photoconversion efficiency over 26%", Nat. Energy 2:5 (2017) 17032. DOI: 10.1038/nenergy.2017.32

[12] https://www.trinasolar.com/us/resources/newsroom/210-perc-cell-sets-world-record-24.5%25-efficiency

[13] W. Fhus, K. Niemann, J. Stuke, "Heterojunctions of amorphous silicon and silicon single crystals," AIP Conference Proceedings 20, 1974, pp. 345-350. DOI: 10.1063/1.2945985

[14] H. Matsuura, T. Okuno, H. Okushi, K. Tanaka, "Electrical properties on n-amorphous/p-crystalline silicon heterojunctions," J. Appl. Phys. 55 (1984) 1012-1020. DOI: 10.1063/1.333193

[15] H. Matsuura, "Hydrogenated amorphous silicon/crystalline silicon heterojunctions: properties and applications," IEEE Trans. Electron Dev. 36 (1989) 2908-2914. DOI: 10.1109/16.40954

[16] H. Mimura, Y. Hatanaka, "Carrier transport mechanisms of p-type amorphous-n-type crystalline silicon heterojunctions," J. Appl. Phys. 71 (1992) 2315-2320. DOI: 10.1063/1.351104

[17] M. Tanaka, M. Taguchi, T. Matsuyama, T. Sawada, S. Tsuda, S. Nakano, H. Hanafusa, Y. Kuwano, "Development of new a-Si:H/c-Si heterojunction solar cells: ACJ-HIT (Artificially Constructed Junction-Heterojunction with Intrinsic Thin-Layer)", Jpn. J. Appl. Phys. 31 (1992) 3518. DOI: 10.1143/JJAP.31.3518

[18] https://news.panasonic.com/global/press/en140410-4

[19] https://www.longi.com/en/news/p-type-hjt-record/

[20] R. L. Anderson, "Experiments on Ge-GaAs heterojunctions", Solid-State Electron. 5:5 (1962) 341-351. DOI: 10.1016/0038-1101(62)90115-6

[21] P. Würfel, "Physics of solar cells: from principles to new concepts", Wiley-WCH, Weinheim (2005). ISBN: 978-3-527-61855-2

[22] M. Zeman and D. Zhang in "Physics and technology of amorphous-crystalline heterostructure silicon solar cells", W. van Sark, L. Korte, F. Roca (Eds.), Springer-Verlag Berlin Heidelberg (2012). DOI: 10.1007/978-3-642-22275-7

[23] U. Würfel, A. Cuevas, P. Würfel, "Charge carrier separation in solar cells," IEEE J. Photovolt. 5:1 (2015) 461-469. DOI: 10.1109/JPHOTOV.2014.2363550

[24] S. De Wolf, A. Descoeudres, Z. C. Holman, C. Ballif, "High-efficiency silicon heterojunction solar cells: a review", Green 2:1 (2012) 7-24. DOI: 10.1515/green-2011-0018

[25] H. Angermann and J. Rappich in "Physics and technology of amorphous-crystalline heterostructure silicon solar cells", W. van Sark, L. Korte, F. Roca (Eds.), Springer-Verlag Berlin Heidelberg (2012). DOI: 10.1007/978-3-642-22275-7

[26] X. Chen, X. Yu, X. Zhu, P. Chen, D. Yang, "First-principles study of interstitial boron and oxygen dimer complex in silicon", Appl. Phys. Express 6:4 (2013) 041301. DOI: 1882-0786/6/4/041301

[27] J. Schmidt, K. Bothe," Structure and transformation of the metastable boron and oxygen-related defect center in crystalline silicon", Phys. Rev. B 69:2 (2004) 024107. DOI: 10.1103/PhysRevB.69.024107

[28] W. van Sark, L. Korte, F. Roca in "Physics and technology of amorphous-crystalline heterostructure silicon solar cells", W. van Sark, L. Korte, F. Roca (Eds.), Springer-Verlag Berlin Heidelberg (2012). DOI: 10.1007/978-3-642-22275-7

[29] M. Tucci, L. Serenelli, S. De Iuliis, M. Izzi, G. de Cesare, D. Caputo in "Physics and technology of amorphous-crystalline heterostructure silicon solar cells", W. van Sark, L. Korte, F. Roca (Eds.), Springer-Verlag Berlin Heidelberg (2012). DOI: 10.1007/978-3-642-22275-7

[30] R. Schlaf, H. Murata, Z.H. Kafafi, "Work function measurements on indium tin oxide films", J. Electron. Spectrosc. Relat. Phenom. 120 (2001) 149-154. DOI: 10.1016/S0368-2048(01)00310-3

[31] K. Sugiyama, H. Ishii, Y. Ouchi, K. Seki, "Dependence of indium-tin-oxide work function on surface cleaning method as studied by ultraviolet and x-ray photoemission spectroscopies", J. Appl. Phys. 87:1 (2000) 295-298. DOI: 10.1063/1.371859

[32] N. Manavizadeh, F. A. Boroumand, E. Asl-Soleimani, F. Raissi, S. Bagherzadeh, A. Khodayari, M. A. Rasouli, "Influence of substrates on the structural and morphological properties of RF sputtered ITO thin films for photovoltaic application", Thin Solid Films 517:7 (2009) 2324-2327. DOI: 10.1016/j.tsf.2008.11.027

[33] C. Li, M. Furuta, T. Matsuda, T. Hiramatsu, H. Furuta, T. Hirao, "Effects of substrate on the structural, electrical and optical properties of Al-doped ZnO films prepared by radio frequency magnetron sputtering", Thin Solid Films 517:11 (2009) 3265-3268. DOI: 10.1016/j.tsf.2008.11.103

[34] L. R. Damiani, R. D. Mansano, "Thickness dependence of indium-tin oxide thin films deposited by RF magnetron sputtering", ECS Trans. 31:1 (2010) 117-124. DOI: 10.1149/1.3474149

[35] D. Tonini, G. Cellere, M. Bertazzo, A. Fecchio, L. Cerasti, M. Galiazzo, "Shingling technology for cell interconnection: technological aspects and process integration", Energy Procedia 150 (2018) 36-43. DOI: 10.1016/j.egypro.2018.09.010

[36] J. Melskens , B. W. H. van de Loo , B. Macco, L. E. Black, S. Smit, W. M. M. Kessels, "Passivating contacts for crystalline silicon solar cells: from concepts and materials to prospects", IEEE J. Photovolt. 8:2 (2018) 373-388. DOI: 10.1109/JPHOTOV.2018.2797106

[37] P. Gao, Z. Yang, J. He, J. Yu, P. Liu, J. Zhu, Z. Ge, J. Ye, "Dopant-free and carrier-selective heterocontacts for silicon solar cells: recent advances and perspectives", Adv. Sci. 5 (2018) 1700547. DOI: 10.1002/advs.201700547

[38] J. Bullock, M. Hettick, J. Geissbühler, A. J. Ong, T. Allen, C. M. Sutter-Fella, T. Chen, H. Ota, E. W. Schaler, S. De Wolf, C. Ballif, A. Cuevas, A. Javey, "Efficient silicon solar cells with dopant-free asymmetric heterocontacts", Nat. Energy 1 (2016) 15031. DOI: 10.1038/NENERGY.2015.31 [39] C. Battaglia, X. Yin, M. Zheng, I. D. Sharp, T. Chen, S. McDonnell, A. Azcatl, C. Carraro, B. Ma, R. Maboudian, R. M. Wallace, A. Javey, "Hole selective MoOx contact for silicon solar sells", Nano Lett. 14 (2014) 967-971. DOI: 10.1021/nl404389u

[40] X. Yang, Q. Bi, H. Ali, K. Davis, W. V. Schoenfeld, K. Weber, "High-performance TiO_2-based electron-selective contacts for crystalline silicon solar cells", Adv. Mater. 28 (2016) 5891-5897. DOI: 10.1002/adma.201600926

[41] M. Adeel, N. Z. Butt, "Heterojunction solar cell with selective contacts", IEEE Proc. 1st International Conference on Electrical, Communication and Computer Engineering, 2019, Swat, Pakistan. ISBN: 9781728138268

[42] H. Imran, T. M. Abdolkader, "Carrier-selective NiO/Si and TiO_2/Si contacts for silicon heterojunction solar cells", IEEE Trans. Electron Dev. 63:9 (2016) 3584-3590. DOI: 10.1109/TED.2016.2585523

[43] T. Zhang, "Transition metal oxides and their application as hole-selective contacts for silicon solar cells", PhD thesis, 2019.

[44] C. Messmer, M. Bivour, J. Schön, and M. Hermle, "Requirements for efficient hole extraction in transition metal oxide-based silicon heterojunction solar cells", J. Appl. Phys. 124 (2018) 085702. DOI: 10.1063/1.5045250

[45] C. Battaglia, S. Martın de Nicolas, S. De Wolf, X. Yin, M. Zheng, C. Ballif, and A. Javey, "Silicon heterojunction solar cell with passivated hole selective MoOx contact", Appl. Phys. Lett. 104 (2014) 113902. DOI: 10.1063/1.4868880

[46] A. Tyagi, K. Ghosh, A. Kottantharayil, S. Lodha, "An analytical model for the electrical characteristics of passivated carrier selective contact (CSC) solar cell", IEEE Trans. Electron Dev. 66:3 (2019) 1377-1385. DOI: 10.1109/TED.2019.2893998

[47] J. Bullock, Y. Wan, M. Hettick, J. Geissbühler, A. J. Ong, D. Kiriya, D. Yan, T. Allen, J. Peng, X. Zhang, C. M. Sutter-Fella, S. De Wolf, C. Ballif, A. Cuevas, A. Javey, "Survey of dopant-free carrier- selective contacts for silicon solar cells", IEEE 43rd Photovoltaic Specialists Conference, 2016. DOI:10.1109/PVSC.2016.7749580

[48] Y. Wang, S. T. Zhang, L. Li, X. Yang, L. Lu, D. Li, "Dopant-free passivating contacts for crystalline silicon solar cells: progress and prospects", EcoMat. (2022) e12292. DOI: 10.1002/eom2.12292

[49] X. Yang, P. Zheng, Q. Bi , K. Weber, "Silicon heterojunction solar cells with electron selective TiOx contact", Sol. Energy Mater. Sol. Cells 150 (2016) 32-38. DOI: 10.1016/J.SOLMAT.2016.01.020

[50] J. Bullock, P. Zheng, Q. Jeangros, M. Tosun, M. Hettick, C. M. Sutter-Fella, Y. Wan, T. Allen, D. Yan, D. Macdonald, S. De Wolf, A. Hessler-Wyser, A. Cuevas, A. Javey, "Lithium fluoride based electron contacts for high efficiency n-type crystalline silicon solar cells", Adv. Energy Mater. 6 (2016) 1600241. DOI: 10.1002/aenm.201600241

[51] Y. Wan, C. Samundsett, J. Bullock, T. Allen, M. Hettick, D. Yan, P. Zheng, X. Zhang, J. Cui, J. Mc Keon, A. Javey, A. Cuevas, "Magnesium fluoride electron-selective contacts for crystalline silicon solar cells" ACS Appl. Mater. Interfaces 8 (2016) 14671–14677. DOI: 10.1021/acsami.6b03599

[52] J. Dréon, Q. Jeangros, J. Cattin, J. Haschke, L. Antognini, C. Ballif, M. Boccard, "23.5%-efficient silicon heterojunction silicon solar cell using molybdenum oxide as hole-selective contact", Nano Energy 70 (2020) 104495. DOI: j.nanoen.2020.104495

[53] W. Wu, J. Bao, X. Jia, Z. Liu, L. Cai, B. Liu, J. Song, "Dopant-free back contact silicon heterojunction solar cells employing transition metal oxide emitters", Phys. Status Solidi - Rapid Res. Lett. 6 (2016) 1–6. DOI: 10.1002/pssr.201600254

[54] R. Islam and K. C. Saraswat, "Metal/Insulator/Semiconductor carrier selective contacts for photovoltaic cells", Proc. IEEE 40th Photovoltaic Specialists Conference, 2014, pp. 285-289

[55] X. Yang, W. Liu, J. Chen, Y. Sun, "On the annealing-induced enhancement of the interface properties of NiO:Cu/wet-SiO_x/n-Si tunnelling junction solar cells", Appl. Phys. Lett. 112 (2018) 173904. DOI: 10.1063/1.5026135

[56] H. Fujiwara, T. Kaneko, M. Kondo, "Application of hydrogenated amorphous silicon oxide layers to heterojunction solar cells", Appl. Phys. Lett. 91 (2007) 133508. DOI: 10.1063/1.2790815

[57] J. P. Seif, A. Descoeudres, M. Filipič, F. Smole, M. Topič, Z. C. Holman, S. De Wolf, C. Ballif, "Amorphous silicon oxide window layers for high-efficiency silicon heterojunction solar cells", J. Appl. Phys. 115 (2014) 024502. DOI: 10.1063/1.4861404

[58] F. Menchini, L. Serenelli, L. Martini, M. Izzi, G. Stracci, P. Mangiapane, E. Salza, M. Tucci, "Transparent hole-collecting and buffer layers for heterojunction solar cells based on n-type-doped silicon", Appl. Phys. A 124 (2018) 489. DOI: 10.1007/s00339-018-1903-z

Chapter 3

Doped nickel oxide as hole-transport layer

In this chapter lithium- and silver-doped nickel oxide are investigated as possible candidates to form hole-selective contacts with n-type c-Si substrates. Different techniques are used for deposition and their suitability is discussed. Heterojunction devices are manufactured and their performances are analysed, identifying qualities and limits of the different materials and methods. Part of the content of this chapter has been presented in international conferences ([18] in the List of Publications).

3.1 Introduction

As deeply explained in Chapter 2, the main characteristics that selective contacts must possess are carrier selectivity and preservation of passivation. Transparency is also required for contacts to be placed on the illuminated side of the cell. As already introduced in Section 2.4, a certain number of materials has been individuated as candidates for hole-selective contacts and, in some cases, has reached a good grade of maturity. Some issues however remain to be solved, first of all the poor temperature stability of the materials, which hinders their complete exploitation in final applications.

In this chapter we investigate the possible application of doped nickel oxide (NiOx) films as hole-transport layer by studying the characteristics of the films and of the hetero-structure devices in which they will be inserted. First we describe some properties of nickel oxide, then we illustrate experiments on heterostructure devices containing lithium-doped NiOx deposited by e-beam evaporation. Finally we explore the potentialities of thermal evaporation of lithium- and silver-doped NiOx from different crucibles.

The main effort of the research lies in the use of low-temperature deposition methods as a tool for low-thermal budget processes that are preferred when coming to industrial applications. Such methods must ensure an efficient doping and a suitable band structure of the grown material, to produce optimal charge selectivity. Moreover, the thermal stability and the performances of the materials after a thermal annealing at 200°C must be examined, as this treatment is a fundamental step in full industrial processes.

3.2 Nickel oxide and its applications in silicon heterojunctions

Nickel(II) oxide (NiO) is potentially abundant and low cost, has good intrinsic chemical stability and is compatible with silicon fabrication [1]. It is often referred to as NiOx, which is its nickel-deficient form, as explained in the next section. Moreover it has a wide bandgap (between 3.4 and 3.8 eV [2, 3]) and a high transmittance in the UV-Vis range [2], which make it suitable for applications as front layer in solar devices.

The most interesting characteristic for applications as carrier selective layer in silicon heterojunctions is the almost perfect alignment of its valence band with that of silicon. In fact, due the combination of a low electron affinity (1.5-1.8 eV [4, 5]) and a wide bandgap, the energy of the valence band maximum is brought to an average value between 5.2 and 5.5 eV (see Figure 3.1a), i.e. very close to that of silicon (5.17 eV) and this, in principle, confers to the material optimal hole-extracting properties. However the Fermi level of stoichiometric NiO is far from the valence band edge, thus a large offset is created with the valence band of silicon, so that also a doping of the material is mandatory.

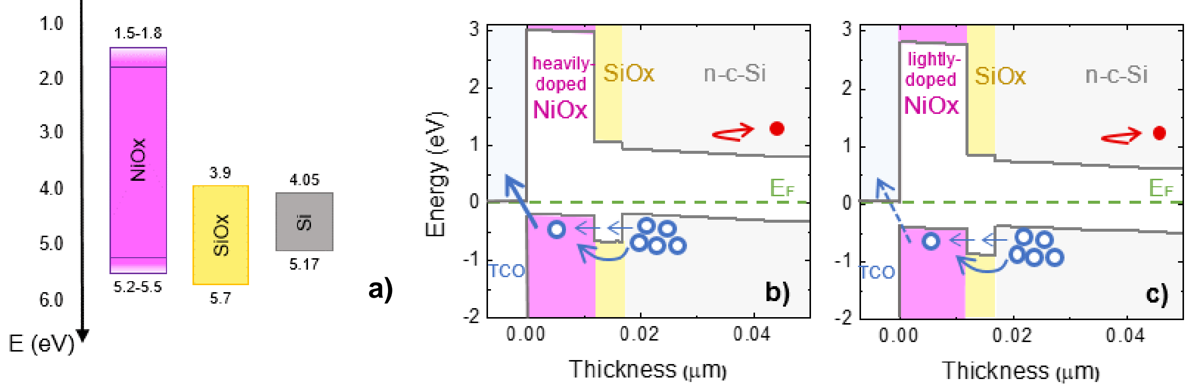

Figure 3.1 a) Energy bands of NiOx, c-Si and SiOx. Simulated band diagram in a n-c-Si/SiOx/doped-NiOx/TCO structure where the NiOx has b) a higher and c) a lower doping concentration, and thus a lower or a higher activation energy, that bring to different barrier heights with silicon.

Several simulation articles can be found in the literature on the topic. Islam et al. [6] estimated a 27.98% efficiency for a NiOx film used as hole-extracting layer on n-c-Si, but the calculations were conducted without taking into account bulk or surface defects and in ideal conditions of band alignment and Fermi level pinning towards the valence band edge of silicon. Imran et al. [7] calculated that a high doping (~10^{19} cm^{-3}) of the NiOx is necessary to produce a large built-in between NiOx and n-c-Si and hence induce a strong electric field which lowers the surface recombination. Menchini et al. confirmed such conclusions in [8], experimentally showing that no photocurrent could be extracted from a c-Si/NiOx device in forward bias, as shown in Figure 3.2; this was attributed to a high concentration of defects at the c-Si/NiOx interface that pins the Fermi

level and inverts the c-Si surface, causing the s-shape form in the J-V characteristic. This situation can be considered as a starting point for the necessary optimisation of the structure. Notwithstanding the promising theoretical potentialities, only a few experimental articles can be found on hole-selective NiOx layers on n-type silicon. Hsu et al. [9] implemented lithium-doped NiO films in an n-c-Si based heterostructure with optimised back contact, and they reached a 6.3% efficiency thanks to the NiO doping, but still no c-Si passivation was introduced. More recently, Yang et al. [10] reported a conversion efficiency of 6.3% in a solar cell containing copper-doped NiO, which was increased to 10.8 % after thermal annealing; in this case the c-Si substrate was passivated by a thin wet SiOx layer. In Figure 3.2b the simulated J-V characteristic of the structure depicted in Figure 3.1b is reported. It can be seen that the performances are even better than those of a corresponding cell containing a-Si , thanks to the higher transparency of NiOx:Li; obviously the NiOx shall be highly doped.

So far, then, the theoretically ideal features of doped NiOx have not been fully exploited yet. As deduced from the above-reported study, it appears that impressive results cannot be achieved unless the following requirements are fulfilled: i) a good surface passivation of the c-Si substrate to neutralise interface defects and ii) a proper doping of the NiOx film.

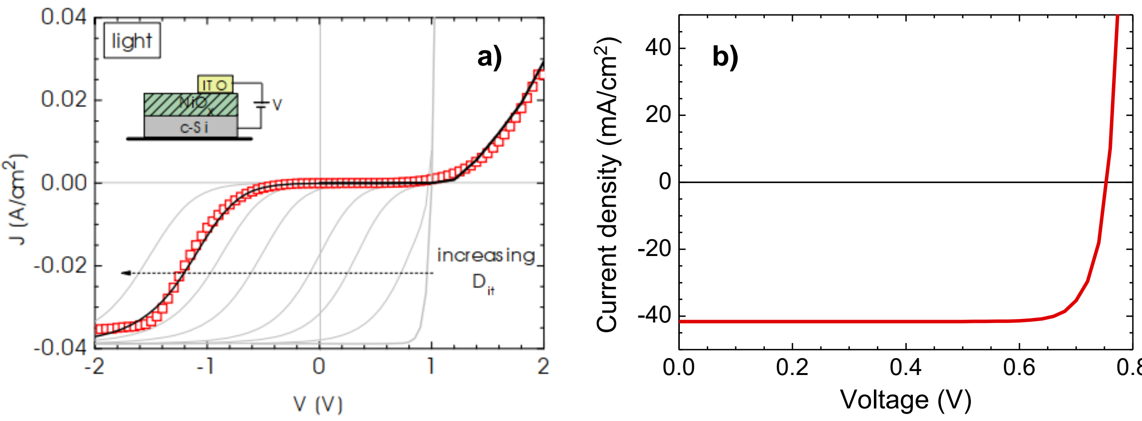

Figure 3.2 a) Light J-V characteristics of a NiOx-based heterojunction structure on n-c-Si, showing a s-shape (red dots). The grey lines are simulations with increasing concentrations of surface defects D_{it} in the range between 2×10^{10} cm^{-2} and 3×10^{13} cm^{-2}. The black line corresponds the simulation for D_{it} = 1.8×10^{13} cm^{-2}. Adapted from [8]. This device, with no passivation of the c-Si substrate and no doping of the NiOx layer, can be considered as a starting point for further optimisation. b) Simulated light J-V characteristics of a HJ with the structure depicted in Figure 3.1b.

3.3 Conductivity of pure, sub-stoichiometric and doped nickel oxide

Nickel(II) oxide has a rock-salt crystalline structure (see Figure 3.3). It is a semiconducting transition-metal oxide for which the conventional band theory does not hold satisfactorily, mainly

because the outer valence orbitals of adjacent atoms do not have a strong enough overlap so to form bands of delocalised energy levels [11], and the electrons in the outer (d) orbital are more localised than itinerant (rather in bonds than in bands). Materials with such characteristics are called *hopping semiconductors* and the conduction electrons, though localised on single atoms, can hop to neighbour atoms when supplied with sufficient energy. Stoichiometric NiO is a greenish solid with a very low conductivity that in particular conditions (e.g. after heating in air at 800°C) becomes black and semiconducting, with an empirical stoichiometry $Ni_{1-x}O$ ($x \approx 0.1$), often referred to also as NiOx. The same intrinsic non-stoichiometry is usually obtained in oxygen-rich deposition processes of thin films [12]. Some of the Ni^{2+} ions are oxidised to Ni^{3+}, so some Ni^{2+} ions diffuse out of the material to maintain charge balance, leaving cation vacancies (*V*). In this form the cation sites contain a mixture of Ni^{2+} and Ni^{3+} ions and cation vacancies, indicated by the formula $Ni^{2+}_{1-3x}\,Ni^{3+}_{2x}\,V_x\,O$. Electrons are able to hop from Ni^{2+} to Ni^{3+} ions, which can be seen as a Ni^{3+} ion moving, causing the p-type conductivity of the material. However, controlling this kind of conductivity is quite tricky, as the oxidation is highly temperature dependent. Instead the concentration of Ni^{3+} ions can be fixed by adding an aliovalent dopant cation (C^+). To ensure charge neutrality the obtained material, a *controlled valence semiconductor* indicated as $C^+_x\,Ni^{2+}_{1-2x}\,Ni^{3+}_x\,O$, will contain the same amount of C^+ and Ni^{3+} ions, which permits controlling the conductivity via the doping. Moreover, no vacancies are left in the lattice, avoiding possible distortions.

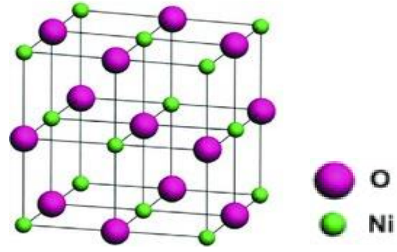

Figure 3.3 Structure of NiO. The green spheres represent the nickel atoms (cations) while the pink spheres represent the oxygen atoms (anions).

Increasing dopant concentrations are found to increase the material conductivity [13], so this could allow tailoring the Fermi level positioning inside the gap. Different elements (not only monovalent) can be used as dopants for NiO, such as lithium [13-15], caesium [16], aluminium [17], copper [18], zinc [19], silver [20] or a combination of them [21]. Among them, Li^+ is very indicated for the purpose due to its ionic radius (0.135 Å) which is very similar to that of Ni^{2+} (0.145 Å). While doped NiOx is largely used as hole-extracting layer in perovskite solar cells [20, 22], exciting results have not been achieved yet on silicon solar cells, which is the aim of the present research.

3.4 Electron-beam deposited NiOx:Li as hole-transport layer

As a first approach, we tried to deposit lithium doped nickel oxide (NiOx:Li) by electron-beam evaporation. The pellets, containing different dopant concentrations (see Appendix for details), were heated by a focused e-beam and evaporated onto rotating substrates that were not intentionally heated during deposition. One control sample was also evaporated from an undoped

NiO pellet. The thickness of the films was controlled by a quartz oscillator during the growth process, being too small to be measured with a mechanical profilometer.

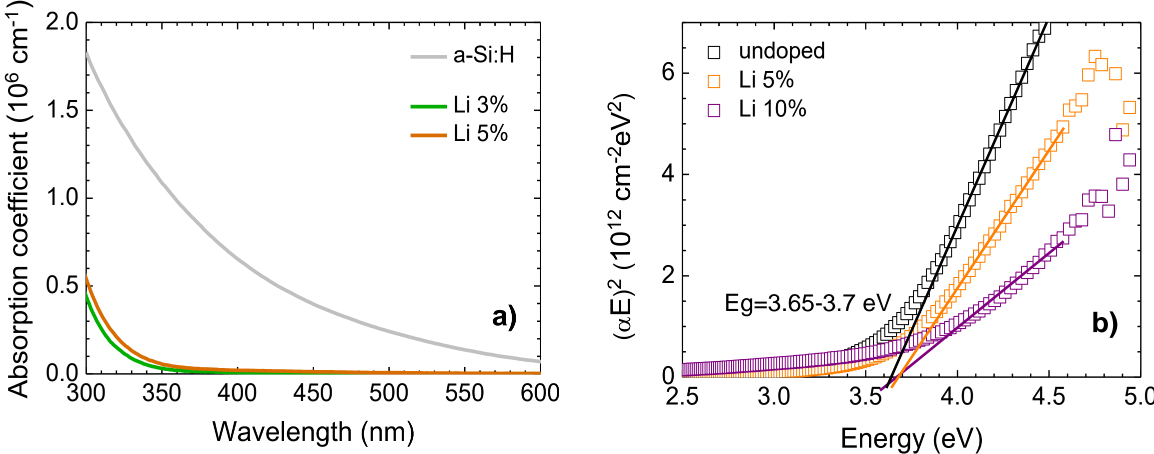

Figure 3.4 a) Absorption coefficient of two NiOx:Li films with different Li doping concentrations compared to that of a-Si:H; b) Tauc plots for an undoped NiO_x film and two NiOx:Li films with different Li doping concentrations, with the extrapolation of the linear part indicating the Eg.

Some films were deposited on glass for the optical characterisation, and the results are shown in Figure 3.4a, confirming the higher transparency of NiOx:Li with respect to the amorphous silicon (p-a-Si) counterpart. The bandgap of the undoped film is around 3.65 eV (Figure 3.4b), while the doped films have a slightly higher Eg, around 3.7 eV, in accordance with other literature values [13, 23].

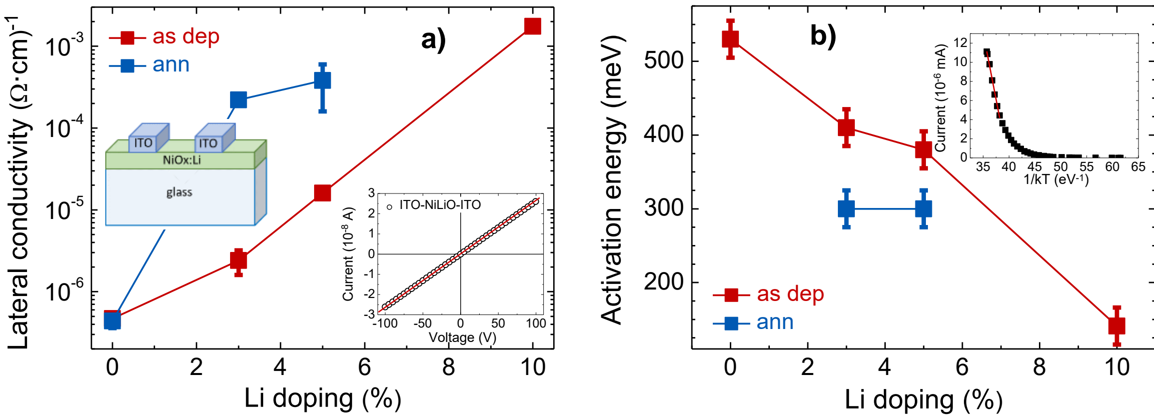

Figure 3.5 a) lateral conductivity and b) activation energy of NiOx:Li films with different Li doping before (red symbols) and after (blue symbols) a thermal annealing treatment of 180°C for 30’. The inset in Fig. 3.5a shows the ohmic contact between the NiOx:Li film and the ITO contact pads for a representative sample. The inset in Figure 3.5b shows the Arrhenius plot for the evaluation of the activation energy for a representative sample.

The electrical properties of the films were measured as described in the Appendix, and the results are reported in Figure 3.5. Two ITO pads were deposited over the films to ensure the contact, which was proven to be ohmic for all samples (see inset in Figure 3.5a). It can be seen that as the Li doping increases the conductivity of the films also increases from 4.7×10^{-7} $(\Omega \cdot cm)^{-1}$ in the undoped sample to 1.8×10^{-3} $(\Omega \cdot cm)^{-1}$ in the highly-doped sample, while in the same range of Li doping the activation energy drops from 530 mV to 140 mV. Both results are in accordance with the increase of doping: an increased concentration of Li in the material induces the substitution of more Ni^{2+} lattice cations, forming valence vacancies, i.e. free holes that increase the p-type conductivity of the material. The activation energy is consequently reduced because of the approaching of the Fermi level to the valence band. After annealing the conductivity of the samples is increased and the activation energy is consequently reduced.

Based on these premises, several devices were fabricated in order to test the performances of the NiOx:Li films as hole extractors. An n-type textured c-Si wafer was used as a substrate, and was passivated on both sides by a 5.5 nm-thick layer of SiOx deposited via PECVD. The emitter side was composed by a 15-20 nm-thick NiOx:Li layer with different Li doping contents covered by an 80 nm-thick layer of ITO, subsequently annealed at 180°C for 10’ to improve lateral conductivity. The base contact on the back side of the c-Si was ensured by the application of an InGa eutectic film (see Appendix for details). Samples with this structure are called *half-cells*. Only for Cell 5%, a standard base contact was realised, after the deposition of the front layers, by growing a 18 nm-thick layer of n-type a-Si:H covered by an 80 nm-thick layer of ITO and a full metal contact of Ag. The ITO films on the p- and n- side were grown at room temperature and at 180°C, respectively, to obtain a high and low work function, respectively, which are best suited for the respective contact. As the deposition of the n-a-Si:H is carried out at a temperature of about 200°C, it produces a thermal treatment on the whole structure. This latter sample is indicated as *full cell* in contrast to the other devices with the InGa back contact. No metal grid was applied on any of the ITO films, but some dots of Ag paint were used to reduce the contact resistivity between the measuring probes and the ITO film on the illuminated p-side. Some details of the samples are summarised in Table 3.1 together with their PV parameters, and the structures of half- and full-cells are sketched in Figure 3.6.

Table 3.1 Structure, characteristics and PV parameters of half- and full-cells containing electron beam-deposited NiOx:Li films with different doping concentrations.

Sample	Li conc. (% at.)	NiOx:Li film thickness (nm)	Device structure	V_{OC} (mV)	J_{sc} (mA/cm^2)	FF (%)	η (%)
Cell 0% e-b.	0	15	half-cell	279	8.5	24.6	0.58
Cell 3% e-b.	3	20	“	306	17.5	29.3	1.57
Cell 5% e-b.	5	20	full-cell	324	33.6	37.1	4.04

The light and dark J-V characteristics of the structures were measured and the results are shown in Figure 3.7, while the PV parameters are summarised in Table 3.1. As expected, the device containing the undoped NiO films (Figure 3.7a) showed very poor performances; still, there is no s-shape and some photocurrent is measured in forward bias, with an evident improvement with respect to the starting situation depicted in Figure 3.2. Most probably the (still small) photocurrent could be extracted thanks to the presence of the passivation on the c-Si substrate, which drastically decreased the number of interface defects and thus recombination. When some Li doping (3%) is introduced in the NiO film, the J-V characteristic shows a slight increase in V_{OC} and FF (Figure 3.7b) and a further improvement after a thermal annealing treatment at 180°C connected with the decreased activation energy of the material. Yet the half-cell does not reach high performances also because of the removed passivation on the back side.

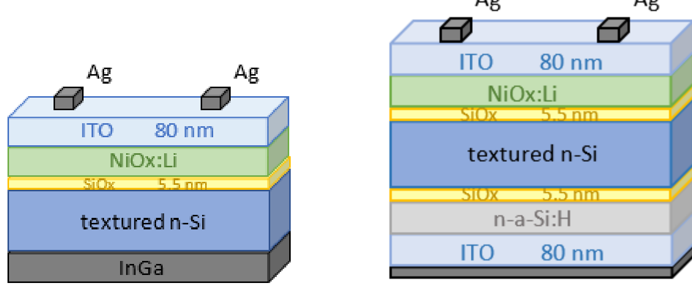

Figure 3.6 Structures of the half- (left) and full-cells (right) containing a NiOx:Li film as HTL.

Encouraged by these results, we then realised a complete cell with a NiOx:Li film with a higher doping (5%) and completed the back contact of the cell as already described. The J-V characteristics of the cell are reported in Figure 3.7c and show a V_{OC} of 324 mV, a FF of 37.1% and a J_{sc} of 18.6 mA/cm^2, confirmed by the internal quantum efficiency shown in Figure 3.7d. The better performances are clearly connected to the cell structure. The presence of the n-a-Si:H back contact ensures an efficient electron extraction and a lower series resistance, which results in an higher FF, while the higher V_{OC} could be due to a better band alignment as a consequence of the reduced activation energy of the NiOx:Li layer. The lower inverse current in the dark characteristics of Cell 5% with respect to that of Cell 3% (insets in Figure 3.7b and c) also confirms a lower recombination current due to a lower defect density. The fact that in Cell 5% the light and dark characteristics do not cross each other (lower inset in Figure 3.7c) is also an indication that no V_{OC} drop due to a valence band offset is present in the cell, as explained also in Section 2.3.6 and in [24]. However, the overall features of the cell are still scarce. Beyond the non-optmised front and back contacts (no metal grids are applied to the back and front of the structure to reduce the R_{sh} and increase the FF) and probably the excessive thickness of the NiOx:Li film, the main reason for the low performances of the cell was connected to the low V_{OC}, due to the very low lifetime of the structure. In fact the initial lifetime of the passivated substrate (above 1 ms) was strongly deteriorated after the NiOx:Li

film deposition, when it reached 100 μm, and not even the thermal treatment was able to restore it.

Figure 3.7 J-V characteristics and quantum efficiency of some representative cells as described in Table 3.1.

We theorised that this could be a consequence of the e-beam deposition technique, during which x-rays are emitted from the electronic gun. To prove this, we positioned several passivated substrates in different positions inside the evaporation chamber (see Figure 3.8), so that some of them laid inside the plume of the evaporated material, while others were not hit by the evaporated particles (position α, beyond the shutter). It was found that all samples, even those with no deposited material on them, experienced a strong degradation of passivation. This proved that the degradation was not the effect of the deposited material but of the x-rays, which are able to reach every region of the deposition chamber. This radiation cannot be avoided, so the degradation of the samples during e-beam deposition is inevitable. For this reason we were forced to abandon this deposition technique.

Figure 3.8 Test of x-ray irradiation inside the evaporation chamber during e-beam deposition.

To conclude, we realised a proof-of-concept Si-based HJ cell containing a NiOx:Li hole-selective layer, which shows that the material is well suited for such application and could be even further optimised in terms of doping. However, the e-beam deposition technique turned out not to be adequate for depositing materials over passivated c-Si substrates, because of the remarkable and permanent damages to the passivation, which leaded to very low V_{OC} values.

3.5 Thermally evaporated NiOx:Li as hole-transport layer

To avoid the permanent damage to passivation due to x-ray emission during the e-beam evaporation process, we tried to deposit NiOx:Li films by other techniques.

First, a wet chemical spinning deposition method was investigated. The method did not result applicable to textured substrates, as the spun material did not uniformly cover the c-Si surface. However, even for flat substrates we observed some uniformity issues, but the real limiting factor to cell functioning was found, again, to lie in the damage that the deposition and post-deposition heat treatments caused to passivation. The preliminary results were not satisfactory and are not reported here.

Then we passed to explore thermal evaporation. The technique does not imply any emission of radiation, but can present some complications due to the high evaporation temperatures of the source material: in particular NiO has a fusion temperature of around 2000°C. The evaporation material was constituted by the same pellets already used for e-beam evaporation (see Section 3.2.3), while different evaporation crucibles were tested.

As a first experiment, a cylindrical alumina crucible was chosen, due to its high temperature resistance, inserted in a tungsten heater. The deposition rate was kept very low (0.1-0.2 Å) to avoid excessive thermal stresses. We deposited a 7 nm-thick 5%-doped NiOx:Li films over a textured c-Si substrate passivated on both sides with a 5.5 nm-thick SiOx layer. An 80 nm-thick IWO layer (IWO films are described in Chapter 5) and silver dots to contact the probes were deposited over the emitter, while the base contact was realised with InGa (Figure 3.9). The sample was finally annealed at 200°C for 15'. Some details of the sample are reported in Table 3.2.

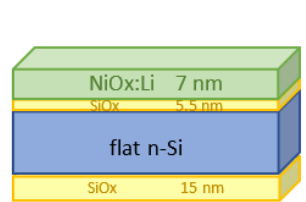

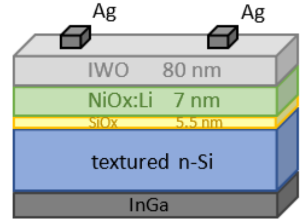

Figure 3.9 Structures of the thermally-evaporated samples for lifetime measurements (left) and J-V characterisation (right).

The light J-V characteristics of the sample are reported in Figure 3.10a and show a typical p-n-junction performance. The PV parameters are reported in Table 3.2. The cell behaviour is compromised mostly in terms of V_{OC} (280 mV), and the dark characteristic (Figure 3.10b) shows a Schottky-like behaviour. The initial lifetime of the passivated substrate + base contact of 1.5 ms dropped to a few tens of µs after the deposition of the emitter, and could not be recovered after the last thermal annealing. So in this case, even if the damaging x-rays connected to e-beam evaporation were no more an issue, some other source of damage for the passivation should have been present. Possibly a diffusion of some metal may have happened during deposition, probably coming from the heater-crucible system, as they were heated at very high temperatures.

Table 3.2 Structure, characteristics and PV parameters of the half-cell containing a thermally-evaporated NiOx:Li film.

Sample	Li conc. (% at.)	NiOx:Li film thickness (nm)	Device structure	V_{OC} (mV)	J_{sc} (mA/cm²)	FF (%)	η (%)
Cell 5% th.	5	7	half-cell	279	28.1	62.0	5.03

To check this possibility, we deposited the same NiOx:Li film on flat c-Si substrate, and used GDOES measurements to identify the composing elements (see Appendix for details on the technique). The results are shown in Figure 3.11a. In the first part of the profile, besides the expected signals form Ni and Li (and O), also a contribution from Al is clearly visible, revealing that a metallic contamination is coming from the crucible-heater (we checked that this contamination was not present in the pellets). The metal contamination is also suggested by the unexpectedly high conductivity of the sample (around 10^{-2} Ω·cm), which is many orders of magnitude higher than the corresponding value found for the e-beam evaporated sample (Figure 3.5). Obviously these contaminations are not acceptable, as they are completely uncontrolled, so they have to be avoided *a priori*. Moreover, they could also be at the basis of the unexpected damage of the substrate after deposition.

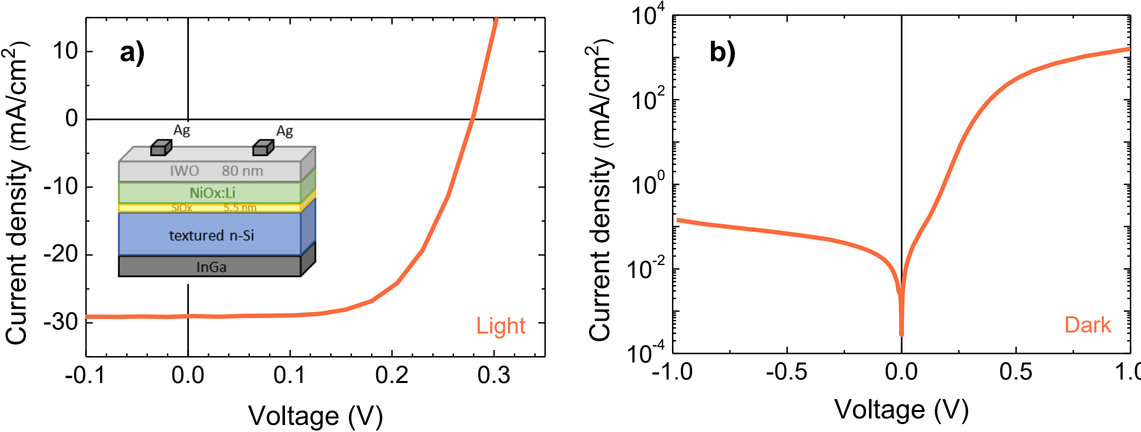

Figure 3.10 a) Light and b) dark J-V characteristics of a cell containing a thermally-evaporated NiOx:Li film.

So we tested several different evaporation set-ups, choosing materials with low chemical reactivity and high temperature resistance, i.e. MgO and ZrO_2 for the crucible and W and Ta for the heater. The GDOES profiles are gathered in Figure 3.11 and the details are given in the caption. In all cases, beyond the elements composing the NiOx:Li film, other elements were detected, proving a contamination from the crucible and/or from the heater, or even from the boat as in the case of a sample evaporated directly from a W crucible, not shown here. The blue dotted line approximately indicates the c-Si interface (see Appendix for details), and we cannot exclude a diffusion of some contamination atoms inside the sample. It may also be observed that the Ni profiles are very different in the various samples, so that the Ni atoms appear to be very mobile inside the structures. This could be the indication that probably part of the Ni atoms in the evaporated material are not or not tightly bond to the NiO lattice, and are free to move. This effect has to be taken into account and eventually monitored. Moreover, when the samples were deposited on passivated c-Si substrates, their lifetime was drastically reduced after deposition and subsequent annealing, from about 1 ms to about 100 µs.

These two clues together let us suppose that the metal contamination and/or diffusion inside the sample could be the cause of lifetime degradation: the contaminants may have induced damages to the interfaces of the structure thus creating recombination centres that have lowered the carriers lifetime. The worst situation would be the one in which the contaminations have reached the c-Si/SiOx interface, damaging the passivation interface itself.

Some of the samples indicated in Figure 3.11 were completed with an 80 nm-thick IWO film on the front and contacted with InGa on the back (see Appendix for details) in order to measure their light J-V characteristics. The results are reported in Figure 3.12. In all cases, the very low V_{OC} values can be connected to the very low lifetimes of the structure after deposition, which indicate a strong degradation of passivation. In addition to this, the s-shapes observed in Figure 3.12b and c are the

indication of a limitation in charge transport that may be due to a strong misalignment between the NiOx:Li bands and those of the c-Si/SiOx substrate. Referring to Figure 3.1b and c, such misalignment could be due to an insufficient doping of the NiOx:Li film, or in general to a too low work function. In this way the NiOx:Li Fermi level would be placed close to midgap, and would establish an energy barrier in the valence band that can be overcome only by an electric field, as happens in reverse polarization when the current is actually saturating. It cannot be excluded that these characteristics of the material may be a result of the deposition technique.

Given these findings, we had to conclude that also thermal evaporation is not suited for the deposition of NiOx:Li, at least for our sintered doped precursor and for the tested crucibles.

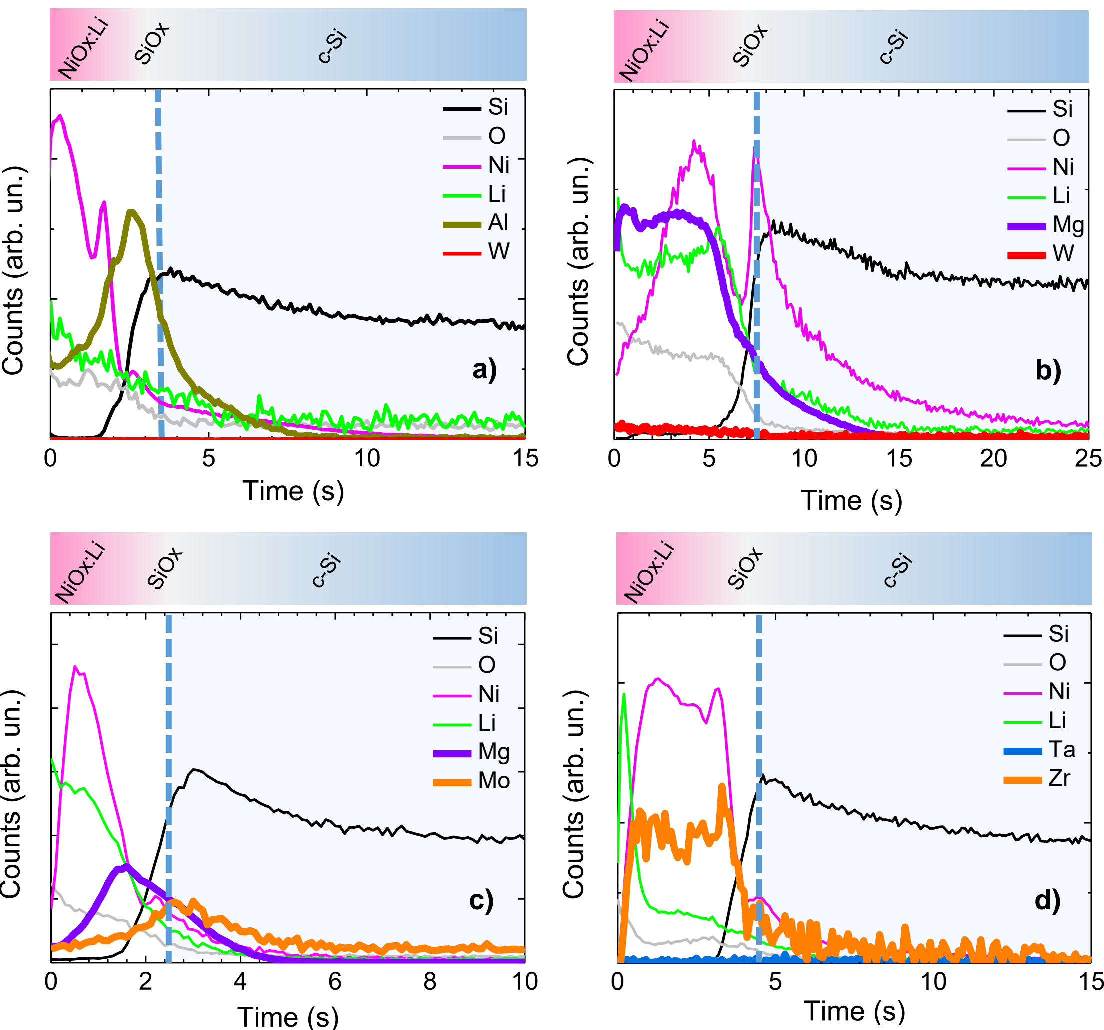

Figure 3.11 GDOES profiles of NiOx:Li films deposited on a c-Si/SiOx substrate by thermal evaporation from a) Al_2O_3 crucible in W heater, b) MgO crucible in W heater, c) MgO crucible over a Mo boat, d) ZrO2 crucible in Ta heater. The positions of the c-Si interface (blue dashed line) and of the films shown in the upper part of the graphs are approximate and only a guide for the eye.

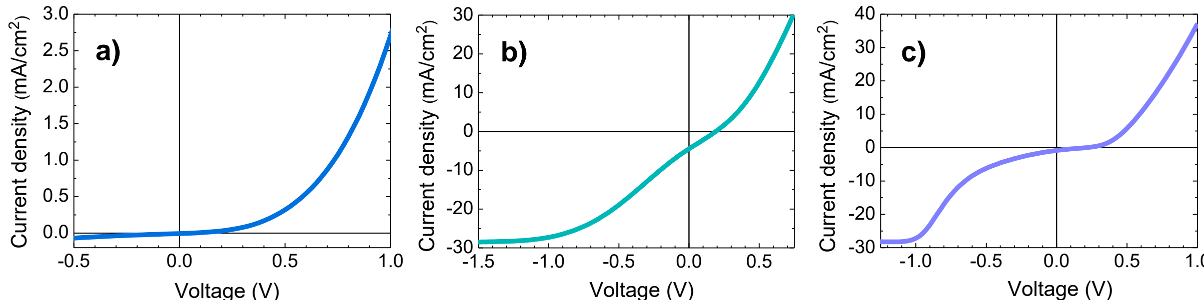

Figure 3.12 J-V light characteristics of some samples containing thermally-evaporated NiOx:Li films from various crucibles: a) MgO crucible in W heater, b) MgO crucible in Ta heater, c) W boat.

3.6 Conclusions on NiOx:Li

Summing up, we tested NiOx:Li films as hole-extracting layers in Si-based heterojunctions. The e-beam evaporation technique was demonstrated not to be compatible with passivated substrates, due to the unavoidable damage caused by x-rays. The more versatile thermal evaporation was also tested, but after many and different attempts it was found out that the used NiOx:Li sintered precursor required too much power to be evaporated, thus causing contaminations coming from the crucible. The reduced lifetimes after deposition and the s-shapes in the J-V characteristics suggested both a damage induced by diffused species and a band misalignment due to low NiOx:Li doping. However the material continues being interesting, so that the challenge for its optimisation still remains open.

3.7 Thermally evaporated NiOx:Ag

As discussed in Sections 3.4 and 3.5, thermal evaporation of NiOx:Li pellets did not bring to performing cells. The main issues can be resumed as follows: i) deposition problems due to the high powers needed during evaporation from sintered NiOx:Li pellets and ii) possible band line-up problems due to low NiOx:Li work function. For these reasons we again changed deposition strategy. We passed to a reactive thermal evaporation of metallic Ni pellets in an oxygen atmosphere. In this way we were able to overcome two problems: firstly, the metallic Ni has a lower melting point (1453°C) than NiO, so that we could evaporate it from a simple W boat without fearing contaminations (as later confirmed by GDOES measurements not shown here); secondly, by means of co-evaporation we are now in principle able to dope the material with any element and in any concentration. As a last point, we could verify if the presence of ambient oxygen during deposition reduces the amount of free Ni and thus its diffusion into the structure.

Table 3.3 Summary of the investigated samples containing Ag-doped NiOx:Ag, together with some of their characteristics. The "structure" indicates the layers deposited over the passivating SiOx layer. The lifetimes are measured on the substrate before deposition (initial), on the sample after the deposition of the single/bi/trilayer and after the thermal annealing. The "delta" values represent percent variations with respect to the initial value.

Sample #	**Structure and thicknesses (nm)**	**Lifetime (μs)**			**Barrier to diffusion?**
	Single emitter layer	**Initial**	**After single layer deposition (delta)**	**After annealing (delta)**	
806	NiOx(7)	700	80 (-88%)	-	
818	NiOx:Ag(5)	2200	30 (-99%)	-	
	LiF interlayer		**After bilayer deposition (delta)**	**After annealing (delta)**	
809	LiF(1.5)/NiO(6)	1300	150 (-88%)	90 (-93%)	no to Ni
	TiO_2 interlayer	**Initial**	**After bi/trilayer deposition (delta)**	**After annealing (delta)**	
814	TiO_2(1.8)/NiO(7)	1000	1400 (+40%)	120 (-88%)	yes to Ni (as dep)
815	TiO_2*(1.5)/NiO(7)	1600		1600 (=)	yes to Ni (ann)
818T	TiO_2*(1.8)/NiOx:Ag(5)	1900	1900 (=)	590 (-69%)	yes to Ag (as dep) no to Ag (ann)
819	TiO_2*(1.8)/NiOx:Ag(5)	2300	2300 (=)	620 (-73%)	"
818W	TiO_2*(1.8)/NiOx:Ag(5)/IWO	-	-	-	
	TiO_2/LiF double interlayer	**Initial**	**After trilayer deposition (delta)**	**After annealing (delta)**	
822	TiO2*(1)/LiF(1)/NiOx:Ag(5)	1600	1200 (-25%)	1200 (-25%)	yes (partial) to Ni and Ag (as dep and ann)
822P	TiO2*(1)/LiF(1)/NiOx:Ag(5)/Pd	-	-	-	
830	TiO2*(0.7)/LiF(0.7)/NiOx:Ag(5)	2600	2250 (-13%)	1000 (-62%)	yes (partial) to Ni and Ag (as dep and ann)
830P	TiO2*(0.7)/LiF(0.7)/NiOx:Ag(5)/Pd	-	-	-	
860	LiF(0.7)/TiO_2*(0.7)/NiOx:Ag(5)	1360	510 (-63%)	410 (-70%)	no

All the samples deposited in this phase are collected in Table 3.3 together with some of their properties to permit a rapid overview. The samples were deposited on flat c-Si to avoid possible issues arising from a non-ideal covering of the textured surface. Basic structures (sketched in Figure

3.13a) were first characterised in terms of lifetime before and after deposition, and checked after an eventual thermal annealing, to evaluate in an evident and reliable manner if a damage to passivation had occurred or not. GDOES profiles were acquired on selected samples to get some suggestions about the behaviour of the composing elements. Finally, J-V characteristics were measured on relevant samples to get a better insight in the transport behaviour of the structures, after having contacted the front and back sides (see Figure 3.13b) as described in the following sections.

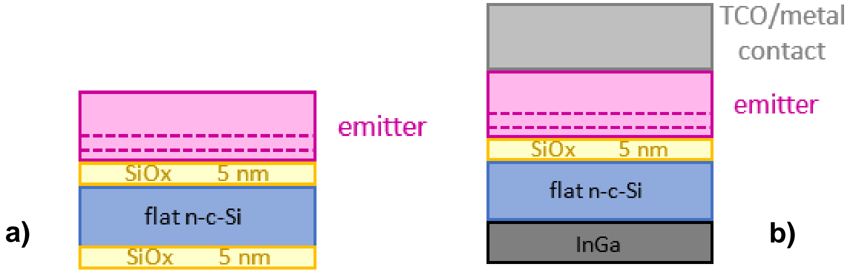

Figure 3.13 Structure of samples containing different emitters with doped and undoped NiO for a) lifetime measurements and b) J-V characterisation.

The trial experiment consisted in depositing a 7 nm-thick NiOx undoped film over a passivated c-Si substrate (Sample 806). The deposition procedure was successful, and we were able to set a very slow deposition rate (~0.2 Å/s) with which we could control the deposition of very thin layers. The initial lifetime of 700 μs was lowered to 80 μs after deposition, indicating a strong damage to passivation.

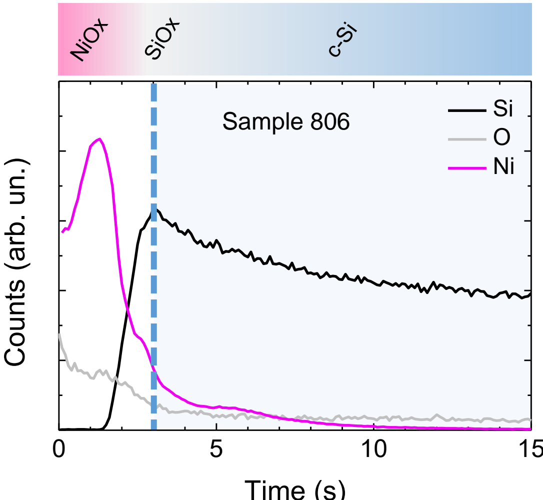

Figure 3.14 GDOES profile of a NiOx/SiOx/c-Si structure (Sample 806). The blue dashed line suggests the position of the c-Si interface.

The GDOES profile of the sample reported in Figure 3.14 shows a small "bump" in the Ni profile right before the c-Si interface, suggesting that probably some Ni from the NiOx film may have diffused inward, eventually reaching the SiOx layer and damaging the c-Si/SiOx interface, explaining the lifetime reduction.

Afterwards we tested the possibility to obtain a doped NiOx layer with this deposition method. We chose Ag as the doping element among the possible options suggested in the literature [20], and performed a co-evaporation with Ni and oxygen. The resulting deposited film is indicated as NiOx:Ag in the following. We first deposited some NiOx:Ag films on glass in order to characterise them. The film had a conductivity of 1×10^{-4} $(\Omega\cdot cm)^{-1}$ and an activation energy of 180 meV, which confirmed the effectiveness of the doping. On the other hand, the absorption coefficient (see Figure 3.15) resulted quite high with respect to that of the NiOx:Li films reported in Section 3.2.3, but still lower than the absorption of a-Si in the short-wavelength range. However, at this stage of the work we wanted to test the general compatibility of the deposition method with the passivated substrate, so we did not optimise the doping nor the transparency yet.

Then we passed to deposit a 5 nm-thick doped NiOx:Ag layer on a passivated c-Si wafer (Sample 818). The initial lifetime of 2.2 ms passed to 30 μs after deposition, revealing a strong lifetime degradation. Of course, we did not expect a different result, if the damage was due to diffusion, as the situation could only have worsened with respect to the undoped NiO film due to the presence of the dopant.

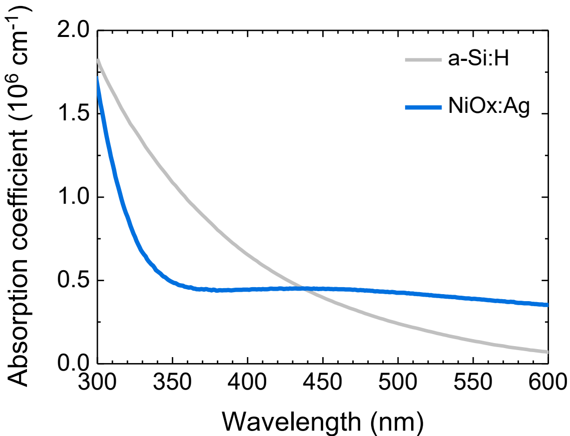

Figure 3.15 Absorption coefficient of a NiOx:Ag film and of a-Si:H for camparison.

In summary, we found out that the deposition of a NiOx:Ag film over a c-Si wafer passivated by a 5.5 nm-thick SiOx layer causes a lifetime degradation of the substrate. A possible explanation could be the diffusion of nickel towards the c-Si/SiOx interface, which could both cause some damage to the passivating layer itself, or induce the formation of some kind of recombining defects inside the structure. This damage would certainly be an obstacle to an effective performance of the

investigated materials as transport layer. So an idea took form of finding some "decoupling" materials which could act as barriers to such diffusion.

3.7.1 The idea of "decoupling" layers: lithium fluoride (LiF)

The first proposed material was lithium fluoride (LiF), which has recently been successfully enclosed among the electron-selective contacts of silicon-based heterojunction solar cells [25]. It is already known that while the direct application of a metallic electrode (typically aluminium) to the c-Si substrate leads to high recombination losses and a Schottky-like behaviour, the addition of a thin LiF layer under the Al contact permits a great improvement in the electron extraction [26, 27].

LiF is an ionic compound with a band gap of about 10 eV due to its insulating nature and a work function of about 2.9 eV [28], so that in heterojunctions it is always applied in very thin layers that can be passed by tunnelling. The mechanism that ensures the very high electron conductivity of the LiF/Al electrode is still not completely explained, and it is most probably due to a combination of factors. In first place the chemical protection of the c-Si surface from the overlying metal, impeding the formation of defects. Another effect reported in the literature for both organic and silicon-based devices is a work function-reduction of the LiF/Al system, probably due to the large dipole moment of the polar LiF molecule, which lowers the injection barrier for electrons between the absorber and the cathode, reducing charge accumulation at the interface [29, 30]. However, some authors report that when LiF is deposited directly on the c-Si surface it induces a high recombination rate [28], so that the introduction of an additional interlayer is necessary. Both a passivation layer (for example SiN_x [26]) or a metal oxide interlayer (for example TiO_x as in [27, 28]) have been tested with promising results, but it appears that the contact cannot withstand a thermal annealing process, with the exception of a device in which the TiO_x layer was fabricated by atomic layer deposition [31].

Summing up, LiF films are currently used to decouple the passivating layer from the outer metallic contact at room temperature. However, all the reported LiF/Al structures badly stand thermal processes. One possible explanation of this problem could be that aluminium is a highly-diffusive material, which upon heating may spread inside the sample and even reach the silicon absorber. As a result, a damage of the c-Si/buffer layer interface with subsequent damage to passivation could happen.

Nonetheless, we tried to implement this material in our structures, also because it can be easily deposited by the same room-temperature thermal evaporation process as the emitter. We optimised the process to grow LiF films from a LiF powder heated in a W boat. The substrates were not intentionally heated. We then grew a sample in which a 1.5 nm-thick LiF layer was interposed between the passivated c-Si/SiOx substrate and a 6 nm-thick NiO intrinsic layer, still undoped (Sample 809). The LiF/NiO films were deposited in sequence without breaking the vacuum. The lifetime of the sample passed from 1.3 ms to 150 μs after the deposition. The final lifetime was

comparable to that of the sample without LiF (Sample 806), indicating that no significant improvement was achieved in terms of protection of the passivation. After annealing the lifetime further degraded to 90 μs, proving further damages.

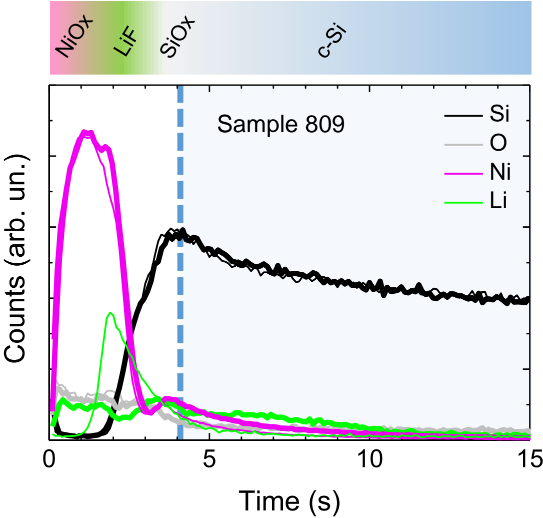

Figure 3.16 GDOES profile of a c-Si/SiOx/LiF/NiOx structure (Sample 809). The blue dashed line suggests the position of the c-Si interface. The thin and thick lines are referred to the various elements revealed in the as-dep and in the annealed sample, respectively.

The GDOES profiles of the sample before and after annealing reported in Figure 3.16 show a small Ni accumulation close to the c-Si interface, which would suggest Ni diffusion as the cause of lifetime degradation. The nickel signal of the sample after annealing is not very different from that of the as-deposited sample, confirming that the detrimental effect had already taken place right after deposition. Moreover it can be seen that the lithium signal, which showed a typical peak in the as-deposited sample, was flattened after annealing, suggesting some decomposition of the LiF layer after a thermal treatment.

In conclusion, the LiF films does not seem to be sufficient to preserve the sample passivation during NiO deposition.

3.7.2 Another decoupling layer: titanium dioxide (TiO_2)

The second tested material was titanium dioxide (TiO_2), taking the suggestion of the already-cited literature that reports TiO_2 films application in c-Si HJ contacts [27, 28, 31-34]. It is also known that TiO_2 can act as a barrier to copper diffusion [35], and copper has a higher diffusivity than nickel [36]. So, also TiO_2 seemed a good candidate to act as a decoupling layer between the passivating layer and the contact of a HJ structure. It has to be pointed out, though, that the cited

TiO_2 films are very often deposited by high-temperature ALD processes. For our applications, we had to implement a room-temperature thermal evaporation method compatible with the other components of the HJ structure. We then evaporated TiO_2 pellets from a W boat in an oxygen atmosphere and a resulting 10^{-4} mbar working pressure.

As a first attempt we produced two samples in which we interposed a 1.5 nm and a 1.8 nm-thick TiO_2 layer, respectively, between the passivated c-Si/SiOx substrate and an intrinsic NiO film, still undoped (Sample 814). The two films were deposited in sequence without breaking the vacuum. The substrate lifetime was increased after deposition in both samples, passing from 420 µs to 930 µs and from 1.0 to 1.4 ms, respectively, proving that no passivation deterioration had taken place. The positive effect on lifetime could be due to the well-known properties of TiO_2 to enhance c-Si surface passivation [37, 38]: in our case the TiO_2 film simply adds up to the SiOx layer producing a better passivation.

The important observation is that, differently from all the samples presented up to now, in these structures containing a TiO_2 interlayer the deposition of the NiO film was not detrimental in terms of lifetime. The GDOES profile of sample 814 in Figure 3.17 does not suggest any accumulation of Ni below the c-Si interface, which would confirm that TiO_2 is acting as a barrier for nickel diffusion.

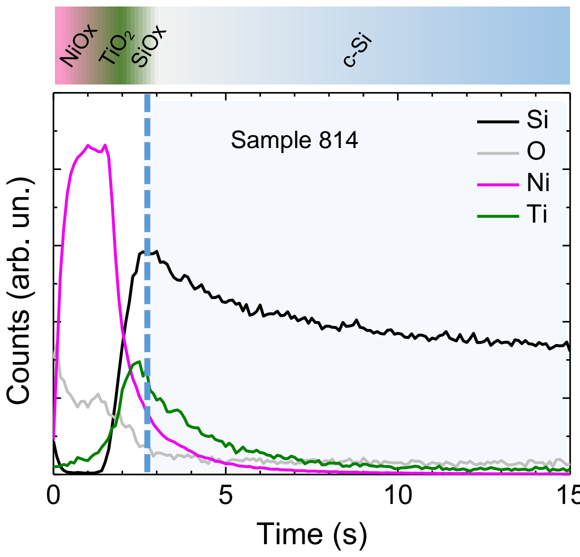

Figure 3.17 GDOES profile of a c-Si/SiOx/TiO_2/NiOx structure (Sample 814).

In addition to these samples, we also tried to slightly change the TiO_2 deposition process by adding more oxygen during the process (Sample 815). Some further descriptions of how this idea took form can be found in Section 4.3.1. The outcomes were even more positive, as the initial lifetime of 1.6 ms was kept unaltered after thermal annealing. This was the first time that such a result was obtained and that no damage of passivation was observed after annealing.

Encouraged by these results, we decided to fix these latter deposition conditions for TiO_2, indicating the corresponding samples as TiO_2*. Then we added the Ag dopant into the NiO film and we deposited two samples with the structure c-Si/SiOx/TiO_2*/NiOx:Ag on two passivated substrates with different starting lifetimes of 1.9 and 2.3 ms, respectively (Samples 818T and 819). After deposition the lifetimes were kept unchanged, while after annealing they decreased to 590 μs and 620 μs, respectively. These lifetimes are the highest observed up to now for annealed samples, so they confirm the positive influence of the TiO_2* layer in protecting passivation even after the deposition of a doped NiOx:Ag layer. However some detrimental effect is still observed, which is then attributed to the presence of the new element, i.e. silver.

The GDOES profile of sample 818T was recorded before and after annealing and is reported in Figure 3.18a. The main effect of the thermal treatment is observed on the Ag signal, which appears more intense in the inner part of the sample and with a slight bump near to the silicon surface. This would suggest a diffusion of silver towards the inside of the sample together with a slight accumulation very close to the SiOx interfaces that could be the main cause of the reduced lifetime after annealing.

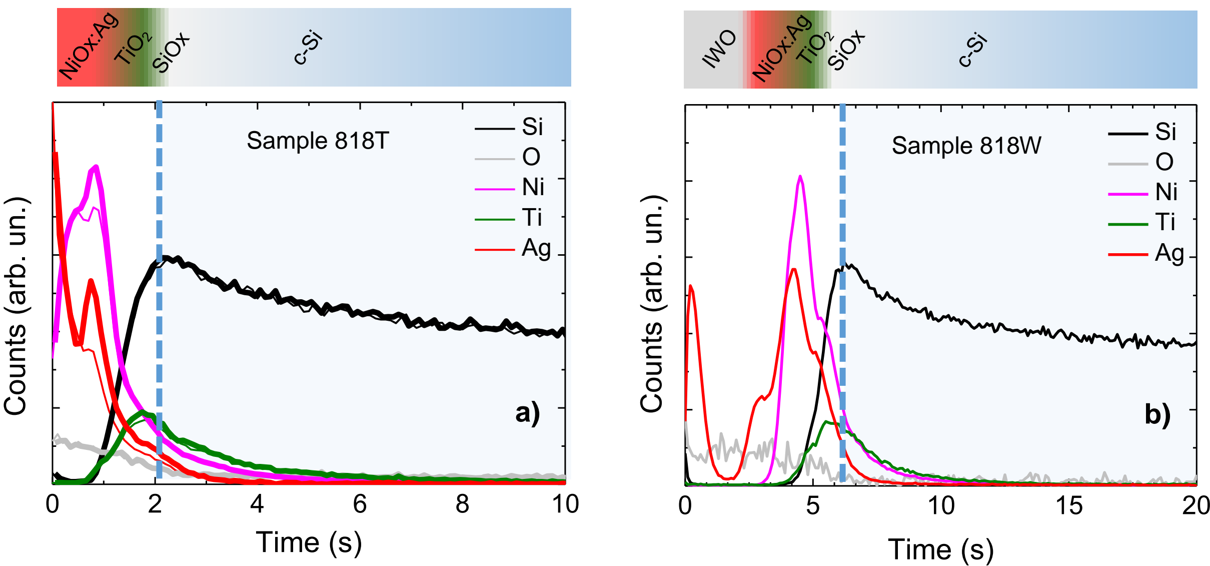

Figure 3.18 GDOES profile of a) a c-Si/SiOx/TiO_2*/NiOx:Ag structure (Sample 818T) and b) a c-Si/SiOx/TiO_2*/NiOx:Ag/IWO structure (Sample 818W). The thin and thick lines in a) are referred to the as-dep and annealed sample, respectively.

On sample 818T we deposited an 80 nm-thick layer of IWO by RF sputtering (see Chapter 5 for details) and we also scribed a metallic grid (Sample 818W) in order to investigate the charge transport inside the structure by measuring the J-V characteristics, reported in Figure 3.19a, and the PV parameters, summarised in Table 3.4. An ohmic contact on the back of the sample was realised with InGa, as described in the Appendix. The light J-V curve of the as-deposited half-cell

shows the desired rectifying behaviour typical of an emitter contact, with no s-shape, a V_{OC} of 421 mV and a fill factor of 32.3 %. The performances of the device are not yet satisfactory, and this is due to many factors: the low V_{OC} is connected to the removed passivation on the back side, and to the damage to passivation due to the IWO deposition, which has not been recovered with an annealing; the low current is related to the excessive width of the fingers; the low fill factor is caused by the poor conductivity of the non-annealed IWO and of the metal grid. Yet the cell starts working, and this is a very good result, because it implies that each deposition step is compatible with the preservation of passivation.

Table 3.4 Structure, characteristics and PV parameters of the half-cell containing a thermally-evaporated NiOx:Ag film with TiO_2* interlayer.

Sample	Films (thickness-nm) composing the cell	Device structure	V_{OC} (mV)	J_{sc} (mA/cm^2)	FF (%)	η (%)
Sample 818W	TiO_2*(1.8)/NiOx:Ag(5)/IWO	half-cell	421	23.6	32.3	3.2

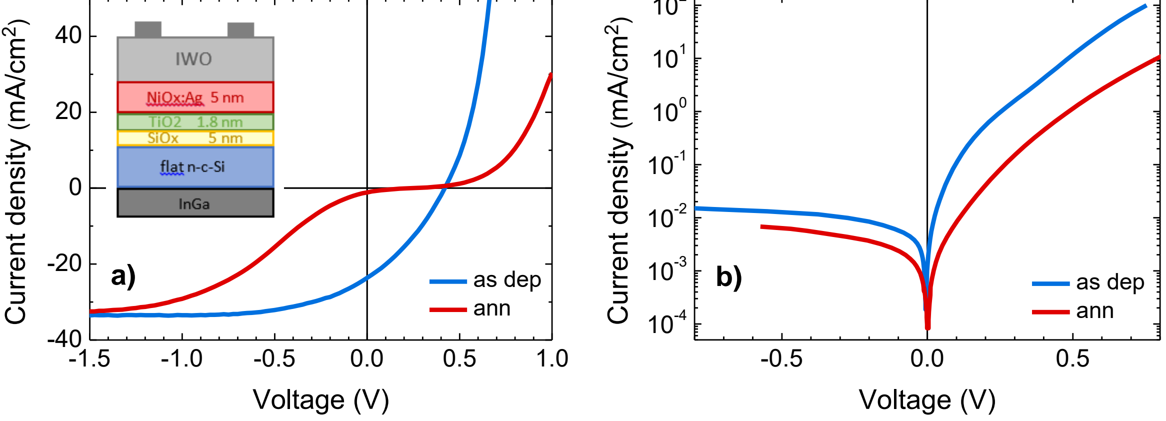

Figure 3.19 Light (a) and dark (b) J-V characteristics of the half-cell c-Si/SiOx/TiO_2/NiOx:Ag/IWO (Sample 818W).

After annealing, the marked s-shape observable on the orange curve in Figure 3.19a indicates an increased series resistance and the creation in the structure of some potential barrier to hole diffusion. The GDOES profile of the as-deposited sample is shown in Figure 3.18b. After the first few (~4) seconds of measurement, relative to the IWO film, the Ni and Ag signals appear very different from the corresponding signals in the as-deposited sample (Figure 3.18a), as they both show intense bumps in the inner part of the sample. This suggests that after IWO deposition and annealing some nickel and silver have been freed from their native layers and have diffused towards the inside of the sample, accumulating near the SiOx layer. This diffusion may have induced

recombining defects both at the tunnelling junction and at the passivating junction, hindering carrier collection. We do not have any further hint to understand where these defects could be located. The lifetime values suggest that after annealing a damage to passivation, i.e. to the c-Si/SiOx interface, has occurred, which may be due to the diffusing species reaching such surface. Comparing the dark JV before and after thermal annealing a barrier against injection is almost evident in forward bias condition even though after thermal annealing a recombination reduction occurs as evident from the reduction of current in low forward and reverse bias voltage. Unfortunately we were not able to measure the lifetime on the sample after annealing to confirm an eventual recovery of passivation.

To sum up, with respect to the cases with the LiF barrier or without any barrier layer over the SiOx film, the introduction of the TiO_2* film has allowed avoiding the loss of passivation after deposition, with encouraging results on half-cells covered with IWO. Even after deposition the passivation is not completely destroyed, indicating that TiO_2* is acting as a (still not perfect) decoupling layer between the SiOx and the emitter. However, both Ni and Ag atoms still seem to have detrimental effects on the structure mostly after thermal annealing, so that an effective solution to the problem has to be found.

3.7.3 The double interlayer

The idea that we tested next was to couple the two just-investigated barrier layers. The TiO_2 was kept to block nickel diffusion, while LiF was reintroduced for its known ability of blocking aluminium and other metals, even if not nickel, as found out in the previous sections. We then deposited a TiO_2*/LiF double layer over the SiOx. The thickness of the films was reduced in order to keep the total thickness of the tunnelling junction low.

A bilayer of TiO_2*/LiF with 1 nm/1 nm thickness was deposited over the SiOx, then the structure was completed with a 5 nm-thick NiOx:Ag layer (Sample 822). The starting lifetime of 1.6 ms was reduced to 1.2 μs after deposition, but remained stable after annealing. This was a very important result, as it was the first time that a structure containing doped NiOx:Ag did not suffer from an important lifetime degradation after annealing. This could be the hint that the double interlayer was effective in protecting the SiOx passivation layer. The reason for this effect is not connected to the thickness of the interlayers, because their total thickness almost matched that of the TiO_2* layer in Sample 818, which lifetime was not preserved after annealing. The efficacy of the double interlayer in avoiding passivation damage is probably connected to the synergic action of the two materials: TiO_2 could act as a barrier for Ni diffusion, as inferred in Section 3.7.2, while LiF is probably efficient in blocking Ag.

On this sample we measured the J-V characteristic after having contacted the rear side with InGa, while the front contact was realised with a semi-transparent 10 nm-thick layer of palladium (Sample 822P). This contact should ensure a direct extraction of the holes without tunnelling because of the better alignment between the work functions of c-Si and Pd (>5 eV). Notwithstanding the preserved passivation, the light J-V characteristic of the as-deposited sample (Figure 3.20a) shows a null photocurrent in direct bias, evidencing a problem in charge transport. Probably the structure contains too many interfaces, which are critical zones where the formation of defects is most probable.

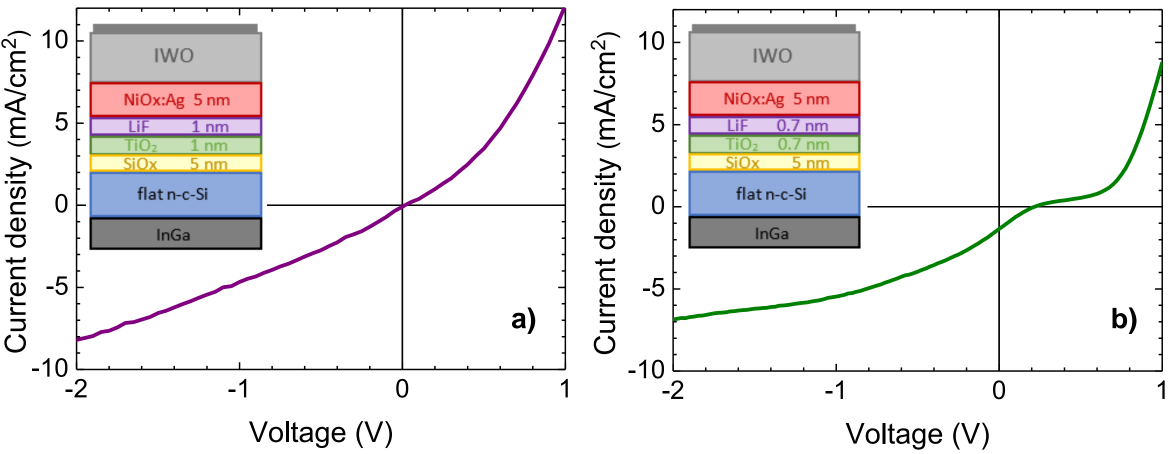

Figure 3.20 J-V light characteristics of half-cells c-Si/SiOx/TiO2*/LiF/Pd with a) 1 nm/1 nm thickness (Sample 822P) and b) 0.7 nm/0.7 nm thickness (Sample 830P) of the double barrier.

It seems, then, that the double interlayer has achieved the goal of stopping any diffusion of metal towards the inside of the sample, which could eventually reach the c-Si/SiOx surface and damage passivation. However, as seen, the transport issues are not yet solved.

One possible hypothesis can be that the total thickness of the barrier layers is too high, so we thinned both layers and manufactured a sample with a 0.7 nm/0.7 nm-thick TiO_2*/LiF barrier (Sample 830P). The initial substrate lifetime of 2.6 ms was reduced to 2.25 ms after deposition and almost halved after annealing. In this case the lifetime had a stronger reduction after annealing with respect to the sample with the thicker double interlayer (Sample 822), but the overall passivation was sufficiently preserved. The J-V characteristic of this sample, reported in Figure 3.20b, showed a very small J_{sc}, yet better than the null value obtained for sample 822P, revealing that the transport problems are still not solved by the thinning of the layers. The hole transport is limited by the presence of too many interfaces that do not allow the tunnelling even in the presence of an electric field. A barrier for hole extraction is present, so that no current is extracted unless in high inverse polarisation.

A structure where the LiF and TiO_2* layers were grown in the inverse order (LiF on SiOx) was also tested (Sample 860), but both the effects on passivation and the J-V characteristics (not shown here) were poorest.

The GDOES analysis of samples 822 and 830 are shown in Figure 3.21. In Sample 830, where the double interlayer is thinner (a), both Ni and Ag appear to move towards the inner part of the sample after annealing. On the contrary in Sample 822, when the double barrier is thicker (b), the Ni signal does not vary after annealing, and the Ag signal shows an accumulation at the surface. This last profile seems, then, to confirm the hypothesis that the thicker double interlayer is able to block metal diffusion and protect the passivation by the synergic action of the LiF and the TiO_2 layer, while the thinner double barrier has only a partial protective effect. It is also worth to notice that in this sample the LiF film does not appear to be disassembled after annealing as was the case (observed in Figure 3.16) for the sample containing the LiF interlayer alone: probably the LiF/TiO2 coupling has a positive effect also from the point of view of the LiF integrity.

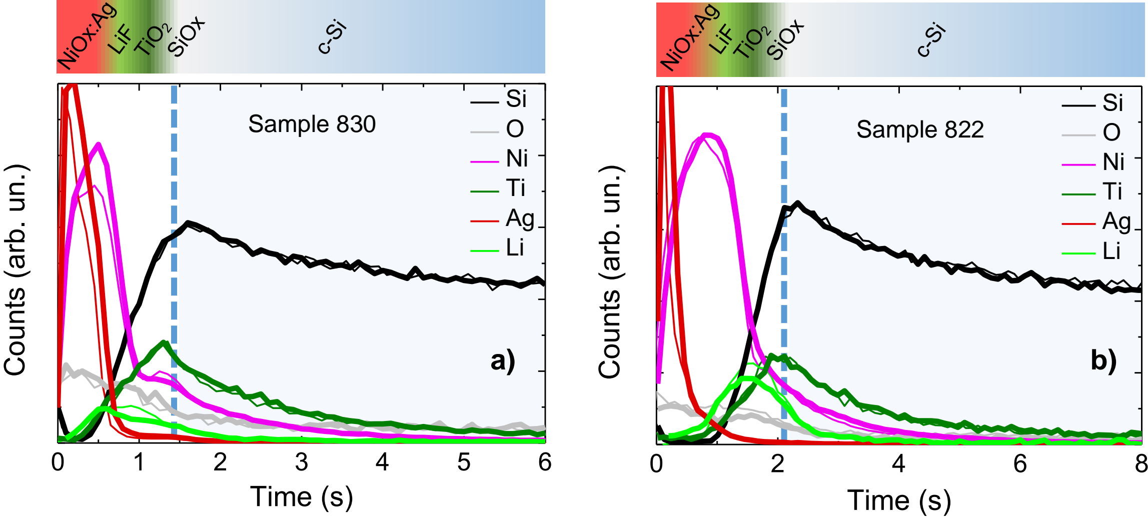

Figure 3.21 GDOES of half-cells c-Si/SiOx/TiO2*/LiF with a) 0.7 nm/0.7 nm thickness (Sample 830) and b) 1 nm/1 nm thickness (Sample 822) of the double barrier. The thin and thick lines are referred to the as-dep and annealed sample, respectively.

Summing up, the last experiments with the double interlayer showed that maybe the road to passivation protection is almost paved, as we demonstrated that an interlayer of TiO_2 is able to block the diffusion of nickel, and a double interlayer of TiO_2/LiF is partially able to block also silver. However, the transport issues are not yet solved, because they depend on the thickness of the barrier and they probably originate from the too high complexity of the multilayer.

3.8 Conclusions on doped NiO as hole-transport layer

We grew and characterised different materials with different dopants, such as NiOx:Li and NiOx:Ag, and we learned that we can obtain materials with different optical and electrical characteristics. However, even if the materials seem to be promising to be applied as HTL, they present many issues when it comes to deposition over a c-Si wafer passivated with a SiOx layer. Electron-beam evaporation is not a suitable method because it is affected by x-ray generation that damages the substrate passivation. Thermal evaporation can pose problems of metal contamination from the crucible if the material has a too high evaporation temperature (such as NiOx or NiOx:Li). Thermal co-evaporation of metallic Ni pellets in a reactive oxygen atmosphere and a metallic dopant (such as Ag) seems the best way to obtain conductive films without contaminants. However it was found out that both Ni and Ag can diffuse inside the samples and induce damages to passivation, which hinder the performances of the cells.

So we tested some materials as interlayers to block such diffusion and preserve passivation. The films, made of insulating materials, have to be kept very thin to allow for tunnelling. The chosen materials showed to be quite effective for the purpose, as we have found out that TiO_2 can act as an effective barrier to Ni diffusion even after a thermal annealing, and that LiF can be suited to partially block Ag diffusion. However these interlayers add complexity to the structures, and usually limit the transport of carriers.

The next steps of the research would include the search for new and better-performing decoupling layers and less-diffusing dopants. Probably it would be beneficial to stick to the thermal-evaporation method, with its advantages if compared to the damaging sputtering and e-beam evaporation techniques.

Results:

- NiOx:Li has suitable characteristics to be used as HTL in c-Si heterojunctions
- Neither e-beam nor thermal evaporation are suitable to deposit doped NiO from ceramic pellets
- NiOx can be thermally evaporated at low temperature from metallic Ni in oxygen atmosphere without contaminations from the crucible and can be doped during growth
- NiOx:Ag deposition is accompanied by metal diffusion that damages passivation
- TiO_2 can act as a barrier to Ni diffusion even after a thermal annealing
- LiF can partially act as a barrier to Ag diffusion
- A double interlayer is the best option in terms of preservation of passivation
- Transport issues are still to be solved

Perspectives:

- Continue experimenting thermal co-evaporation of Ni and different dopants
- Continue experimenting interlayers to preserve passivation

References to Chapter 3

[1] M. Xue, R. Islam, A. C. Meng, Z. Lyu, C. Y. Lu, C. Tae, M. R. Braun, K. Zang, P. C. McIntyre, T. I. Kamins, K. C. Saraswat, J. S. Harris, "Contact selectivity engineering in a 2 μm thick ultrathin c-Si solar cell using transition-metal oxides achieving an efficiency of 10.8%", ACS Appl. Mater. Interfaces 9 (2017) 41863-41870. DOI: 10.1021/acsami.7b12886

[2] T. Abzieher, S. Moghadamzadeh, F. Schackmar, H. Eggers, F. Sutterlüti, A. Farooq, D. Kojda, K. Habicht, R. Schmager, A. Mertens, R. Azmi, L. Klohr, J. A. Schwenzer, M. Hetterich, U. Lemmer, B. S. Richards, M. Powalla, and U. W. Paetzold, "Electron-beam-evaporated nickel oxide hole transport layers for perovskite-based photovoltaics", Adv. Energy Mater. 9 (2019) 1802995. DOI: 10.1002/aenm.201802995

[3] K. J. Patel, M. S. Desai, C. J. Panchal, B. Rehani, "p-type transparent NiO thin films by e-beam evaporation techniques", J. Nano- Electron. Phys. 3:1 (2011) 376-382.

[4] F. H. Hsu, N. F. Wang, Y. Z. Tsai, Y. S. Cheng, M. P. Houng, "A new p-$Ni_{1-x}O$:Li/n-Si heterojunction solar cell fabricated by RF magnetron sputtering", J. Phys. D: Appl. Phys. 46 (2013) 275104. DOI: 10.1088/0022-3727/46/27/275104

[5] M. D. Irwin, D. B. Buchholz, A. W. Hains, R. P. H. Chang, T. J. Marks, "P-type semiconducting nickel oxide as an efficiency-enhancing anode interfacial layer in polymer bulk-heterojunction solar cells", PNAS 105:8 (2008) 2783-2787. DOI: 10.1073pnas.0711990105

[6] R. Islam and K. C. Saraswat, "Metal/Insulator/Semiconductor carrier selective contacts for photovoltaic cells", Proc. IEEE 40th Photovolt. Spec. Conf. PVSC, 2014, pp. 285–289

[7] H. Imran, T. M. Abdolkader, "Carrier-selective NiO/Si and TiO_2/Si contacts for silicon heterojunction solar cells", IEEE Trans. Electron Dev. 63:9 (2016) 3584-3590. DOI: 10.1109/TED.2016.2585523

[8] F. Menchini, M. L. Grilli, T. Dikonimos, A. Mittiga, L. Serenelli, E. Salza, R. Chierchia, M. Tucci, "Application of NiOx thin films as p-type emitter layer in heterojunction solar cells", Phys. Status Solidi C, 13:10-12 (2016) 1006-1010. DOI 10.1002/pssc.201600121

[9] F. H. Hsu, N. F. Wang, Y. Z. Tsai, C. Y. Wu, Y. S. Cheng, M. H. Chien, M. P. Houng, "Enhanced carrier collection in p-$Ni_{1-x}O$:Li/n-Si heterojunction solar cells using LiF/Al electrodes", Thin Solid Films 573 (2014) 159.163. DOI: 10.1016/j.tsf.2014.11.025

[10] X. Yang, W. Liu, J. Chen, Y. Sun, "On the annealing-induced enhancement of the interface properties of NiO:Cu/wet-SiO_x/n-Si tunnelling junction solar cells", Appl. Phys. Lett. 112 (2018) 173904. DOI: 10.1063/1.5026135

[11] A. R. West, "Solid state chemistry and its applications", 2014, John Wiley & Sons Ltd, The Atrium, UK

[12] W. B. Zhang, N. Yu, W. Y. Yu, B. Y. Tang, "Stability and magnetism of vacancy in NiO: a GGA+U study", Eur. Phys. J. B 64 (2008) 153-158. DOI: 10.1140/epjb/e2008-00303-x

[13] J. Arunodaya and T. Sahoo, "Effect of Li doping on conductivity and band gap of nickel oxide thin film deposited by spin coating technique", Mater. Res. Express 7 (2020) 016405. DOI: 10.1088/2053-1591/ab5bf1

[14] C. C. Wu and C. F. Yang, "Investigation of the properties of nanostructured Li-doped NiO films using the modified spray pyrolysis method", Nanoscale Res. Lett. 8 (2013) 33. DOI: 10.1186/1556-276X-8-33

[15] W. L. Jang, Y. M. Lu, W. S. Hwang, W. C. Chen, "Electrical properties of Li-doped NiO films", J. Eur. Ceram. Soc. 30 (2010) 503-508. DOI: 10.1016/j.jeurceramsoc.2009.05.041

[16] W. Chen, F. Z. Liu, X. Y. Feng, A. B. Djurišić, W. K. Chan, Z. B. He, "Cesium doped NiOx as an efficient hole extraction layer for inverted planar perovskite solar cells", Adv. Energy Mater. 7 (2017) 1700722. DOI: 10.1002/aenm.201700722

[17] S. Nandy, U. N. Maiti, C. K. Ghosh, K. K. Chattopadhyay, "Enhanced p-type conductivity and band gap narrowing in heavily Al doped NiO thin films deposited by RF magnetron sputtering", J. Phys. Condens. Matter 21 (2009) 115804. DOI: 10.1088/0953-8984/21/11/115804

[18] M. Yang, Z. Shi, J. Feng, H. Pu, G. Li, J. Zhou, Q. Zhang, "Copper doped nickel oxide transparent p-type conductive thin films deposited by pulsed plasma deposition", Thin Solid Films 519 (2011) 3021-3025. DOI: 10.1016/j.tsf.2010.12.009

[19] T. Zhang, Md. A. Hossain, C.Y. Lee, Y. Zakaria, A. A. Abdallah, B. Hoex, "Atomic layer deposited ZnxNi12xO: a thermally stable hole selective contact for silicon solar cells", Appl. Phys. Lett. 113 (2018) 262102. DOI: 10.1063/1.5056223

[20] J. Zheng, L. Hu, J. S. Yun, M. Zhang, C. F. J. Lau, J. Bing, X. Deng, Q. Ma, Y. Cho, W. Fu, C. Chen, M. A. Green, S. Huang, A. W. Y. Ho-Baillie, "Solution-processed, silver-doped NiOx as hole transporting layer for high-efficiency inverted perovskite solar cells", ACS Appl. Energy Mater. 1 (2018) 561-570. DOI: 10.1021/acsaem.7b00129

[21] W. Chen, Y. Wu, Y. Yue, J. Liu, W. Zhang, X. Yang, H. Chen, E. Bi, I. Ashraful, M. Grätzel, L. Han, "Efficient and stable large-area perovskite solar cells with inorganic charge extraction layers", Science 350:6263 (2015) 944-948. DOI: 10.1126/science.aad1015

[22] Y. Wu, F. Xie, H. Chen, X. Yang, H. Su, M. Cai, Z. Zhou, T. Noda, L. Han, "Thermally stable MAPbI3 perovskite solar cells with efficiency of 19.19% and area over 1 cm^2 achieved by additive engineering", Adv. Mater. 29 (2017) 1701073. DOI: 10.1002/adma.201701073

[23] D. Paul Joseph, M. Saravanan, B. Muthuraaman, P. Renugambal, S. Sambasivam, S. P. Raja, P. Maruthamuthu, C. Venkateswaran, "Spray deposition and characterization of nanostructured Li doped NiO thin films for application in dye-sensitized solar cells", Nanotechnology 19 (2008) 485707. DOI: 10.1088/0957-4484/19/48/485707

[24] L. Serenelli, L. Martini, F. Menchini, M. Izzi, G. de Cesare, G. Condorelli, C. Gerardi, D. Muñoz, M. Tucci, "Selective contacts and fill factor limitations in heterojunction solar cells", Prog. Photovolt: Res. Appl. 29:7 (2021) 876-884. DOI: 10.1002/pip.3418

[25] T. G. Allen, J. Bullock, X. Yang, S. De Wolf, "Passivating contacts for crystalline silicon solar cells", Nature Energy 4 (2019) 914-928. DOI: 10.1038/s41560-019-0463-6

[26] J. Bullock, P. Zheng, Q. Jeangros, M. Tosun, M. Hettick, C. M. Sutter-Fella, Y. Wan, T. Allen, D. Yan, D. Macdonald, S. De Wolf, A. Hessler-Wyser, A. Cuevas, A. Javey, "Lithium fluoride based electron contacts for high efficiency n-type crystalline silicon solar cells", Adv. Energy Mater. 6:14 (2016) 1600241. DOI: 10.1002/aenm.201600241

[27] W. Wang, J. He, D. Yan, C. Samundsett, S. P. Phang, Z. Huang, W. Shen, J. Bullock, Y. Wan, "21.3%-efficient n-type silicon solar cell with a full area rear TiOx/LiF/Al electron-selective contact", Sol. Energy Mater. Sol. Cells 206 (2020) 110291. DOI: 10.1016/j.solmat.2019.110291

[28] J. Bullock, M. Hettick, J. Geissbühler, A. J. Ong, T. Allen, C. M. Sutter-Fella, T. Chen, H. Ota, E. W. Schaler, S. De Wolf, C. Ballif, A. Cuevas, A. Javey, "Efficient silicon solar cells with dopant-free asymmetric heterocontacts", Nat. Energy 1 (2016) 15031. DOI: 10.1038/nenergy.2015.31

[29] D. Yoshimura, T. Yokoyama, E. Ito, H. Ishii, Y. Ouchi, S. Hasegawa, K. Seki, "Electronic structure of Alq3/LiF/Al interfaces studied by UV protoemission", Synthetic Met. 102 (1999) 1145-1146. DOI: 10.1016/S0379-6779(98)01425-8

[30] S. Kim, J. Lee, V. A. Dao, S. Lee, N. Balaji, S. Ahn, S. Q. Hussain, S. Han, J. Jung, J. Jang, Y. Lee, J. Yi, "Effects of LiF/Al back electrode on the amorphous/crystalline silicon heterojunction solar cells", Mater. Sci. Eng. B 178:9 (2013) 660-664. DOI: 10.1016/j.mseb.2012.10.029

[31] J. Bullock, Y. Wan, Z. Xu, S. Essig, M. Hettick, H. Wang, W. Ji, Mathieu Boccard, A. Cuevas, C. Ballif, A. Javey, "Stable dopant-free asymmetric heterocontact silicon solar cells with efficiencies above 20%", ACS Energy Lett. 3 (2018) 508-513. DOI: 10.1021/acsenergylett.7b01279

[32] K. A. Nagamatsu, S. Avasthi, G. Sahasrabudhe, G. Man, J. Jhaveri, A. H. Berg, J. Schwartz, A. Kahn, S. Wagner, J. C. Sturm, "Titanium dioxide/silicon hole-blocking selective contact to enable double-heterojunction crystalline silicon-based solar cell", Appl. Phys. Lett. 106 (2015) 123906. DOI: 10.1063/1.4916540

[33] X. Yang , Q. Bi , H. Ali , K. Davis , W. V. Schoenfeld , K. Weber, "High-performance TiO_2-based electron-selective contacts for crystalline silicon solar cells", Adv. Mater. 28 (2016) 5891-5897, DOI: 10.1002/adma.201600926

[34] X. Yang, K. Weber, Z. Hameiri, S. De Wolf, "Industrially feasible, dopant-free, carrier-selective contacts for high-efficiency silicon solar cells", Prog. Photovolt: Res. Appl. 25 (2017) 896-904. DOI: 10.1002/pip.2901

[35] P. Alén, M. Vehkamäki, M. Ritala, and M. Leskelä, "Diffusion barrier properties of atomic layer deposited ultrathin Ta2O5 and TiO2 Films", J. Electrochem. Soc. 153:4 (2006) G304-G308. DOI: 10.1149/1.2168389

[36] https://thermtest.com/thermal-resources/materials-database

[37] Y. Liu, J. Zhang, H. Wu, W. Cui, R. Wang, K. Ding, S.T. Lee, B. Sun, "Low-temperature synthesis TiOx passivation layer for organic-silicon heterojunction solar cell with a high open-circuit voltage", Nano Energy 34 (2017) 257-263. DOI: 10.1016/j.nanoen.2017.02.024

[38] B. S. Richards, J. E. Cotter, C. B. Honsberg, "Enhancing the surface passivation of TiO_2 coated silicon wafers", Appl. Phys. Lett. 80 (2002) 1123. DOI: 10.1063/1.1445810

Chapter 4

Materials for electron-transport layers

In this chapter different solutions are investigated to produce an electron-selective contacts with n-type c-Si substrates. First, a tungsten-doped titanium dioxide film is studied, but the material's characteristics do not result appropriate for the application. Next, different materials, such as lithium fluoride, titanium dioxide, magnesium fluoride and zinc selenide, are tested as decoupling layers between the SiOx passivation layer and the outer contact. Part of the content of this chapter has been presented in international conferences ([13] in the List of Publications).

4.1 Introduction

The search for an efficient ohmic contact for n-type c-Si, alternative to amorphous silicon, has long been sought but has not yet come to a convincing solution. As already introduced in Section 2.4, some material are currently used to improve electron extraction in Si-based devices, but they are still limited by a low resistance to thermal treatments.

In this chapter different structures are examined. First, a tungsten-doped titanium oxide hole-extracting layer is studied, and its performances inside a heterojunction structure are discussed. Next, different materials are tested as decoupling layers to preserve substrate passivation when an outer contact is deposited on the cell. The behaviour of these materials after thermal annealing is studied and evaluated.

The work described in this chapter has been carried out in parallel and in continuity with that of Chapter 3, so that some results are interlaced. In analogy with the previous work, low-temperature deposition techniques have been employed.

4.2 Tungsten-doped titanium dioxide as electron-transport layer

Titanium dioxide (TiO_2) is present in nature in many polymorphs, the most common of which are rutile, anatase and brookite (see Figure 4.1), which can be also obtained when growing TiO_2 thin films by properly choosing the deposition conditions and post-deposition treatments. Room-temperature deposited TiO_2 films are usually amorphous, while a subsequent thermal annealing or

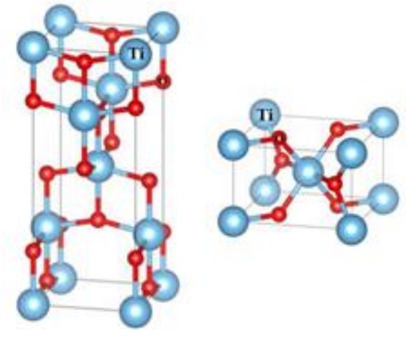

Figure 4.1 Structure of TiO_2 in the a) anatase and b) rutile polimorphs. The blue spheres represent the titanium atoms (cations) while the red spheres represent the oxygen atoms (anions).

a high deposition temperature determine the formation of the anatase phase [1-3]. In photovoltaic applications the anatase phase is usually preferred due to its higher conductivity and mobility.

Recently TiO_2 has been implemented as an electron-transport layer in HJ solar cells due to its small conduction band offset and large valence band offset with silicon [4, 5]. Even though the possibility of using TiO_2 as a passivation layer are known [6, 7], best results have been obtained when using it in conjunction with a passivating tunnel SiO_2 layer. However, the measured V_{OC} of the devices were not very high, and this could depend on a not-ideal band alignment of the materials. The conduction and valence band positions found in literature for TiO_2 span from 3.3 to 4.0 eV and from 6.8 to 7.2 eV, respectively, as depicted in Figure 4.2a. The stoichiometric material is an insulator, while its sub-stoichiometric form, usually obtained from PVD processes, is naturally oxygen-deficient, resulting in a weak n-type semiconducting behaviour with estimated work function values between 3.7 and 4.0 eV [5, 6, 8-10]. The effective band alignment with n-c-Si depends on the combination of these values, so primarily on the electron affinity of the TiO_2 film but also on its doping level and conductivity, which then have to be opportunely chosen. In Figure 4.2b and c we report simulated band diagrams of c-Si heterojunctions containing TiO_2 films with electron affinities that result in different barriers with the c-Si.

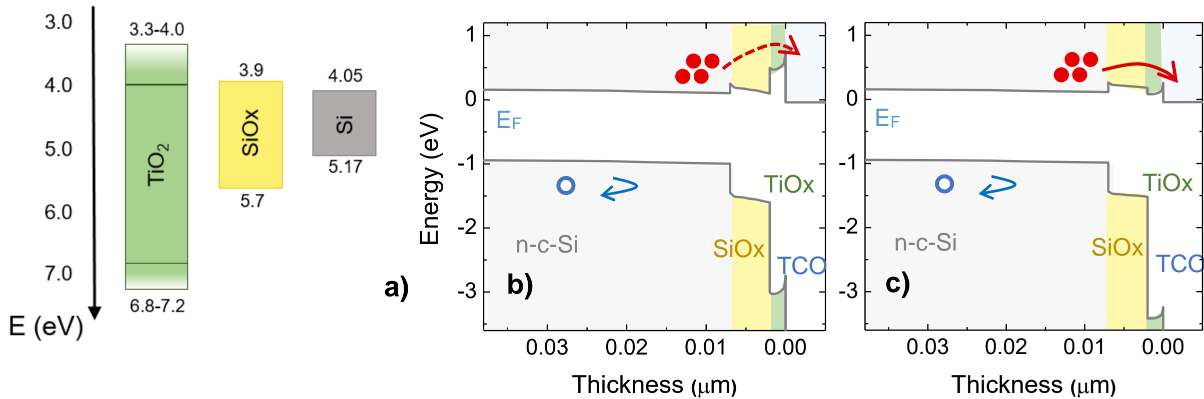

Figure 4.2 a) Energy bands of TiO_2, c-Si and SiOx. Simulated band diagram in a n-c-Si/SiOx/doped-TiOx/TCO structure where the TiOx has an electron affinity of b) 3.5 eV and c) 4.0 eV and a very high doping. In both cases, notwithstanding the high doping of TiOx that brings to an accumulation of the c-Si surface at the interface, in the case of low electron affinity (b) a high barrier for electron extraction is formed.

In analogy with NiO, even TiO_2 has to be doped to obtain a more favourable bad alignment with n-c-Si. It is known that also TiO_2 may become a controlled valence n-type semiconductor by the addition of W^{6+} ions. It has also been proven that the conduction band level of W-doped TiO_2 may be lowered with a consequent reduction of charge recombination in dye-sensitised solar cells [11]. So we decided to experiment tungsten-doped TiO_2 films (TiOx:W).

4.2.1 Thermally evaporated TiOx:W as electron-transport layer

It is clear from the band diagram in that undoped TiO_2 cannot work as a base contact unless it is doped, to move its work function closer to the conduction band. So, we deposited tungsten-doped TiO_2 films (TiOx:W) by thermal evaporation starting from a sintered powder with a nominal dopant concentration of 2% wt. The powder was heated in a tungsten boat and the substrates were not intentionally heated, to keep the process low-temperature. The obtained films were most certainly grown in an amorphous or rutile phase. First, a 7 nm-thick sample was deposited on glass for the optical and electrical characterisation. The absorption coefficient of the film (Figure 4.3a) was found to be lower than that of a-Si, while the energy gap evaluated from the Tauc plot (Figure 4.3b) is around 3.6 eV. The electrical conductivity of the films was around 10^{-5} $(\Omega\cdot cm)^{-1}$, but turned out to be very unstable after air exposure.

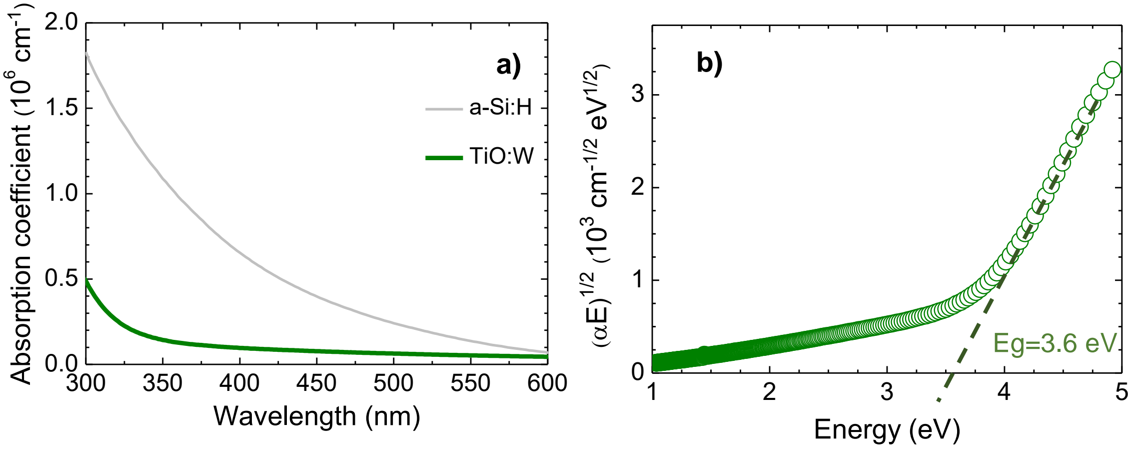

Figure 4.3 Optical and electrical characterisation of TiOx:W films: a) absorption coefficient, b) Tauc plot for the determination of Eg.

The TiOx:W film was then deposited onto n-type c-Si substrates passivated on both sides by a 5.5 nm-thick film of SiOx in order to test its performances as electron-transport layer. The minority carrier lifetime of the sample was checked before and after deposition, and it was found out that the initial substrate lifetime of 500 μs was slightly reduced after TiOx:W deposition (320 μs), evidencing a partial damage to passivation. The sample was then covered with an IWO film over the TiOx:W layer and annealed to recover the sputter damage, and its lifetime of 390 μs showed a

partial increase of lifetime. A half-cell was then produced after removing the back-side passivation and contacting it with InGa (see Appendix), and the measured J-V characteristics are reported in Figure 4.4a in semilog and linear (inset) scales. It appears clear that the contact is not ohmic and shows a typical Schottky behaviour, evidencing the appearance of some barrier to electron transport inside the structure. We verified that the TiOx:W/IWO contact is ohmic (see Figure 4.4b), so that the barrier could only have arisen between SiOx and TiOx:W.

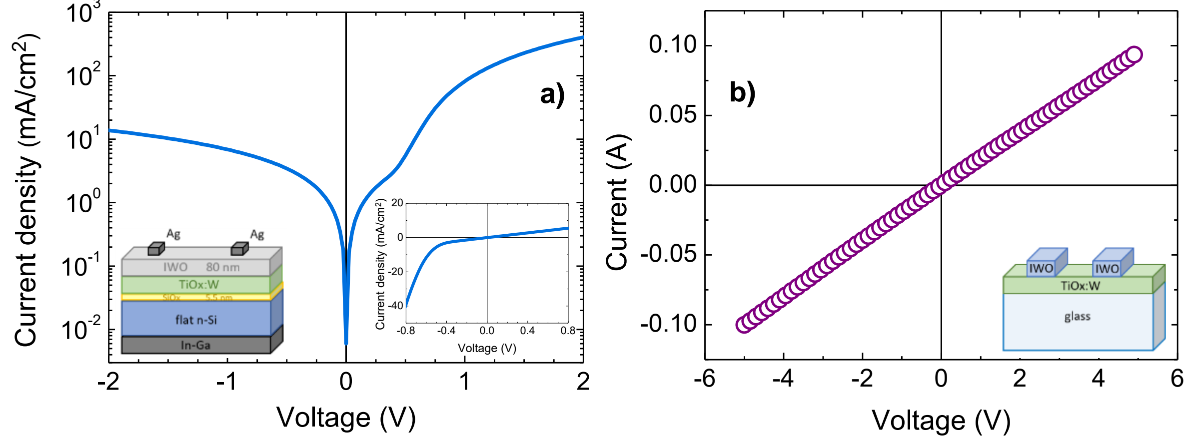

Figure 4.4 a) Dark J-V characteristic of a half cells containing a TiOx:W film (the structure is sketched in the inset). b) Characteristic of the IWO/TiOx:W/IWO contact.

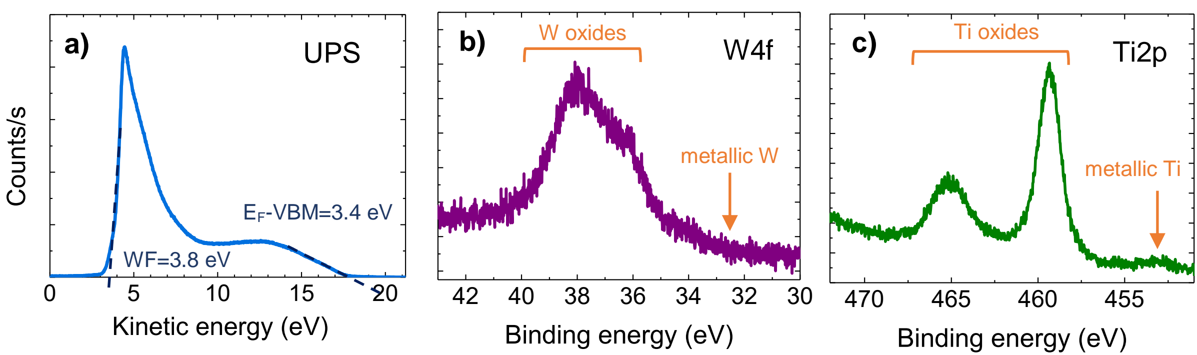

Figure 4.5 a) UPS and XPS profiles of b) W4f and c) Ti2p of TiOx:W.

To have a deeper insight into the matter, we have performed UPS measurements to characterise the energy levels of the TiOx:W film. The spectrum is reported in Figure 4.5a and reveals a work function of 3.8 eV and a distance of the Fermi level from the valence band maximum of 3.4 eV. These data, combined with a band gap of 3.6 eV, place the bottom of the conduction band at 3.6 eV; thus a difference of about 0.4 eV between the conduction band edges of c-Si and TiOx:W arises, which constitutes a barrier to electron transport. The obtained energy diagram is similar to that

depicted in Figure 4.2b. The simulated J-V characteristics for the same sample structure are shown in Figure 4.6a (purple curve), and are clearly rectifying, for any doping level (grey curves). Only an electron affinity of 4.0 eV and a very high level of doping, simulating the band structure in Figure 4.2b, would allow the formation of an ohmic contact (Figure 4.6b).

Moreover, the Schottky-type behaviour of the junction recognised in Figure 4.4a suggests that some metal atoms in the TiOx:W (both Ti or W) could have diffused towards the inner side of the samples, reaching the c-Si interface. This would explain also the observed lifetime reduction after the films deposition. The XPS measurements (Figure 4.5b and c) do not reveal the presence of any metallic W on the outer surface, while the presence of some metallic Ti cannot be excluded; of course, it has to be kept in mind that a completely different situation could be present at the inner interface with SiOx.

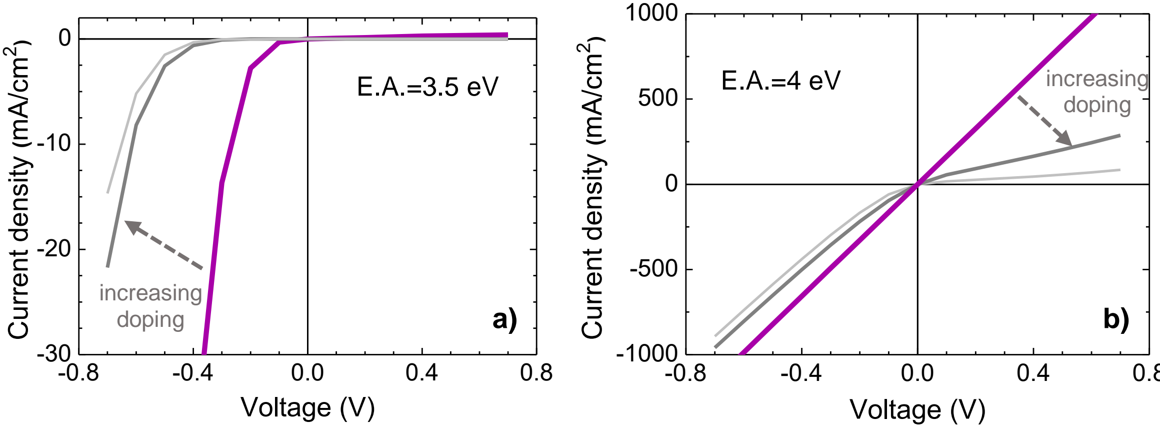

Figure 4.6 Simulated J-V characteristics (purple curves) for the structure and energy levels reported in Figure 4.2b and c. The electron affinity (E.A.) of TiOx:W is fixed at a) 3.5 eV and b) 4.0 eV, and also the doping level is varied (grey curves). Only the situation with an electron affinity of 4.0 eV and a very high doping level brings to an ohmic contact.

4.2.2 Conclusions on TiOx:W

In conclusion, we deposited TiOx:W films over SiOx-passivated n-c-Si substrates, but none of the samples formed an ohmic contact. This result is probably due to the low electron affinity and low work function of the material, as revealed by UPS measurements, which determined the formation of a barrier towards electron collection, as also confirmed by simulations. Another possible cause could be the formation of defects during TiOx:W deposition, as suggested by the lowered lifetime of the samples.

We believe that the success of devices containing TiO_2 films reported in the literature is to be ascribed to the high-temperature ALD deposition process that is common to most of them; moreover in all the works the passivation layer is represented by a high temperature-grown tunnel

SiO_2 film. Both these aspects are most likely at the basis of the effective device performances. On the contrary in our case the low-temperature route makes the properties of the film unsuitable for this application.

However the aim of our research was that of individuating fabrication routes that can be more compatible with industrial production lines, for example by avoiding high temperatures or low-throughput processes, as found in ALD. In this direction, we plan to continue investigating the thermal deposition process, trying to optimise the characteristic of the material mainly by acting on the process parameters and on the doping procedure.

4.3 Oxide, fluorides and selenides tunnelling contacts

As described in Section 4.2.1, the realisation of an electron-transport layer by a thick TiOx:W doped films was not successful. This could be due to different causes, but all of them seem to be connected with the deposition and doping processes. However, we wanted to keep on focusing on the low-temperature thermal evaporation process, which is interesting for its low thermal budget with respect to the ALD one.

We then passed to investigate the possibility of obtaining ohmic base contacts on SiOx by using very thin layers of materials which should act as "decouplers" between passivation and external metallic contact. The starting point is the knowledge that depositing a metallic contact directly on the SiOx passivation layer damages its structure and decreases the lifetime even without any thermal treatment. The problem of passivation damage on the base contact after annealing is well known in the literature. To date, no effective undoped ohmic contact for the n-side on c-Si that is not damaged by annealing has been individuated yet, nor with a full-area metallic film neither with a transparent TCO, which is the long-chased solution for bifacial devices. With these premises, we tried to fabricate an electron contact based on different materials which could add features to the state-of-the-art, such as a simpler deposition method and the possibility of undergoing a thermal treatment. Several decoupling layers were tested in order to get a deeper understanding of the processes happening at the base contact. We tested their contact behaviour and evaluated their recombination rate by comparing the lifetime of the samples before and after deposition. The research was brought about in parallel with what described in Section 3.7, where we were also testing solutions to decouple the passivating SiOx layer from the above-deposited emitter layers. The outer metallic contact was realised by a thin titanium layer, replacing the classic aluminium one. Titanium is another low-work function (<4.2 eV) metal already used in the metallisation of n-type c-Si heterojunctions, which is known to have a lower diffusivity than Al [12]. The substrates were flat n-type c-Si wafers passivated on both sides with a SiOx film which was 5.5 nm thick on the front side and 15 nm thick on the back, to evaluate the lifetime of the structure. To measure the J-V characteristics of the contacts, the back-side passivation was removed and the samples were contacted with InGa (see Appendix for details). All samples used to test the n-contact are grouped in Table 4.1.

Table 4.1 Summary of samples used for base-contact studies, together with some of their characteristics. The substrates are always constituted by flat n-type c-Si wafers passivated by SiOx layers. The lifetimes are measured on the substrate before deposition (Initial), on the sample after the deposition of the bi/trilayer and after the thermal annealing. In brackets are indicated the "delta" that values represent percent variations with respect to the initial value.

Sample #	**Structure and thicknesses (nm)**	**Lifetime (μs)**			**Nature of the contact**	
		Initial	**After base contact deposition**	**After annealing**	**After base contact deposition**	**After annealing**
798	TiO_2(2)/Ti(50)	2500	1500 (-40%)	2000 (-20%)	rectifying	rectifying
827	TiO_2(1)/Ti(30)	2200	690 (-69%)	710 (-67%)	rectifying	-
780	LiF(1.5)/Ti(50)	980	1070 (+9%)	20 (-98%)	OHMIC	rectifying
775	LiF(2)/Ti(50)	540	570 (+6%)	340 (-37)	rectifying	-
836	LiF(1)/TiO_2(0.7)/Ti(30)	990	1000 (+1%)	1670 (+69%)	rectifying	-
832	MgF_2(1)/Ti (30)	3100	3700 (+19%)	230 (-93%)	OHMIC	rectifying
837	MgF_2(1)/ZnS(0.7)/Ti (30)	2700	2300 (-15%)	2200 (-19%)	OHMIC	rectifying

4.3.1 TiO_2/Ti base contact

The first tested material was TiO_2, taking the suggestion of the already-cited literature and the fact that TiO_2 can act as a barrier to copper diffusion [13]. In Section 4.2.1 we already tested doped TiOx:W films as electron-transport layers, but we concluded that the material that we deposited was not suitable to the purpose due to not-ideal band alignment with c-Si. Moreover the deposition of TiOx:W films had a slightly detrimental effect on passivation, probably connected with the deposition process and to a possible diffusion of metallic Ti atoms in the structure. However, as said, TiO_2 is widely used in the literature in c-Si HJ base contacts. The idea was then to implement very thin TiO_2 film as tunnelling barrier layers to metal diffusion.

To this purpose, we decided to deposit TiO_2 by reactive thermal evaporation of TiO_2 pellets in an oxygen atmosphere with the aim of obtaining a more stoichiometric compound with no spurious metallic Ti, as already described in Section 3.7.2.

The first sample (see structures in Figure 4.7a and b) contained a 2-nm thick TiO_2 layer (Sample 798). Positive news came from the lifetime measurements: the starting substrate lifetime of 2.5 ms was damaged by the TiO_2 deposition (1.5 ms), but it was almost recovered after annealing (2.0 ms). This indicated TiO_2 as a possible decoupler between SiOx and the outer metallic Ti contact when a thermal treatment has to be performed. However, from the J-V characteristics (see Figure 4.7c) the contact did not result ohmic, neither before nor after the thermal annealing.

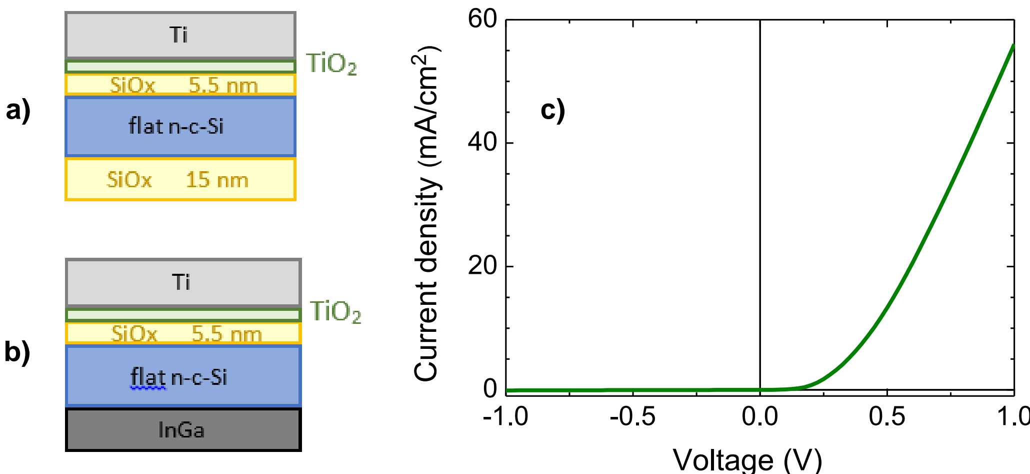

Figure 4.7 Structure of the samples used to test the TiO_2/Ti base contact: a) sample for lifetime measurements; b) sample for J-V characterisation. c) J-V characteristic of the structure c-Si/SiOx/TiO_2/Ti (Sample 798). The contact is not ohmic.

Supposing that the TiO_2 films was too thick to allow a tunnelling for electrons, we grew a similar structure with a 1 nm-thick TiO_2 film (Sample 827). In this sample the substrate lifetime (2.2 ms) was greatly reduced after the bilayer deposition and subsequent annealing (710 µs), showing that a thinner TiO_2 layer is only partially able to protect the passivation, even in the as-deposited sample. However not even this thinner film formed an ohmic contact.

It is evident that the TiO_2/Ti deposition caused some damage to the structure, as evidenced by the lifetime reduction observed in both samples. In the case of the thinner film, where no issues can be attributed to a too-thick tunnelling barrier, still these defects posed limitations to carrier transport. In analogy with the findings of the previous sections, this damage could again be due to a diffusion, probably from the outer metallic Ti contact towards the c-Si/SiOx passivating interface, or to defects created at the TiO_2/SiOx interface during growth.

Summing up, we have found out that a thin TiO_2 layer is not suited to form a tunnelling junction between SiOx and Ti, even for a very small thickness of 1 nm. This is somehow in contrast with what can be read in the already cited literature [4, 5, 8, 14-16]. The possible explanation can lie in the different deposition methods used: most of the reported TiO_2 layers in ohmic base contacts are deposited by high temperature ALD. This method is obviously very different from the thermal evaporation that we employ, so that the two materials cannot be directly compared. Most probably the ALD-grown TiO_2 films have some structural and chemical characteristics which make them more compatible with the adjacent layers. Moreover, the passivating layer that we employ is quite different from the standard a-Si film usually coupled with TiO_2 in the literature, and this could also influence the compatibility with TiO_2. One possible test would be of thinning also the passivating SiOx layer, to enhance the tunnelling probability. However, we already know that this would reduce

the protection to the c-Si/SiOx interface, leaving it exposed to the sputtering damage that would inevitably come when depositing the TCO. So, even this attempt would probably not bring to any solution.

These latter results do not invalidate the relevance of the parallel attempts performed on the emitter contact containing the NiOx:Ag films. In the former case, in fact, the tunnelling through TiO_2 was supposed to be enhanced by the presence of the built-in voltage between the c-Si and the emitter. In that case, however, the poor performances of the structure were ascribed to the bad band alignment between c-Si and NiOx:Ag and thus to the poor doping of the emitter.

In conclusion, given that the protection of the SiOx passivation with a thin TiO_2 layer is not yet satisfactory, we passed to test different decoupling layers.

4.3.2 LiF/Ti base contact

We tested thin tunnel LiF layers on c-Si/SiOx substrates (see Figure 4.8a and b), encouraged by the LiF ability of blocking metallic Ag as deduced in Section 3.7.3.

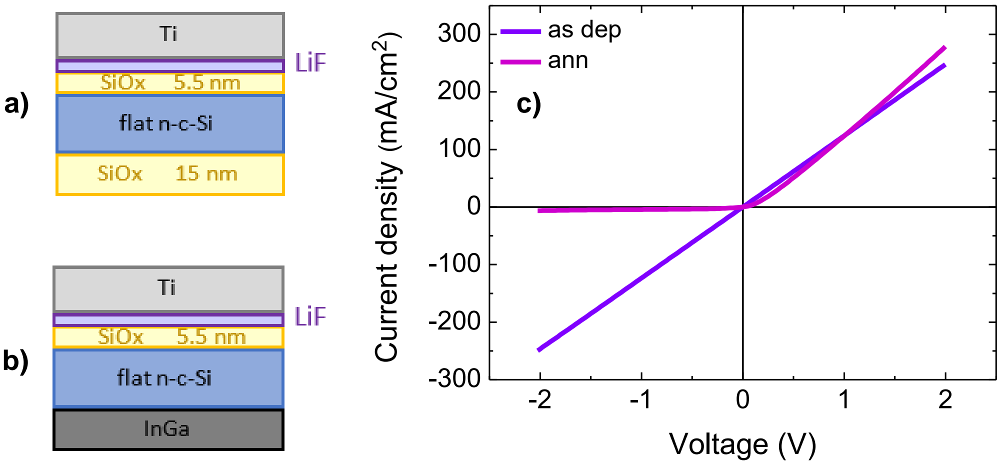

Figure 4.8 Structure of the samples used to test the LiF/Ti base contact: a) sample for lifetime measurements; b) sample for J-V characterisation. c) J-V characteristics of the structure c-Si/SiOx/LiF/Ti (Sample 780) before and after annealing. The contact is ohmic before annealing, but becomes rectifying after the thermal treatment.

A first sample was grown in which the LiF film was 1.5 nm thick (Sample 780). The minority carrier lifetime (980 μs) of the passivated wafer was not degraded after evaporation of the LiF film and of the bilayer (1070 μs), and this is a first good result that confirms the fact that both LiF and Ti are compatible with SiOx and that the LiF thin film acts as a decoupling layer between the metal contact and the passivation layer. The transverse J-V characteristic of the as-deposited contact

showed an ohmic behaviour, reported in Figure 4.8c, confirming the formation of a tunnelling base contact. However, after annealing the structures at 200°C for 10 minutes the lifetime was drastically reduced to 20 µs and the contact was found to be rectifying. A possible cause could be again a Ti diffusion through the LiF film and toward the SiOx, so we tested the contact with a thicker (2 nm) LiF film (Sample 775). The initial lifetime (540 µs) was preserved after the bilayer deposition (570 µs), but the contact had become rectifying, probably because the LiF film thickness was too large to allow a tunnelling of the electrons. After annealing, while the contact was still rectifying, the lifetime was reduced, even if not completely cut down as for the thinner sample. One possible explanation of these behaviours could be that the thicker LiF film works as a barrier to Ti diffusion even after annealing, thus acting as a decoupling layer from SiOx, even if the efficiency is not perfect. At the same time the thicker layer is no more ensuring a tunnelling contact. This could be also a consequence of the LiF film degradation upon annealing observed from the GDOES profiles in Figure 4.17.

In summary we have found that a thin LiF layer allows the formation of an ohmic base contact with a c-Si/SiOx substrate, while partially preserving the passivation. This is an improvement with respect to the thin TiO_2 layer, which was neither perfectly preserving passivation nor ensuring an ohmic contact. Probably the oxide nature of TiO_2 is not completely compatible with the (similar) oxide nature of the underlying SiOx, probably due to the presence of hydrogen within the SiOx that in principle could diffuse inside TiO_2 and reduce it at the interface. On the contrary, the ionic nature of the LiF film molecules could be the key to explain its better preservation of passivation and its better transport mechanisms. The explanation of these effects could be the topic of future investigations.

4.3.3 LiF/TiO_2/Ti base contact

Having observed in Section 3.7 that the TiO_2/LiF barrier was somehow effective in preserving passivation, even if not yet with a good behaviour in terms of transport, we planned a further experiment with a double barrier layer on the base contact (see Figure 4.9a and b). We grew a sample with a LiF (1 nm)/TiO_2 (0.7 nm) bilayer (Sample 836). The initial passivation of 990 µs was preserved after the trilayer deposition (1000 µs) and even increased after annealing (1670 µs) but the contact did not show an ohmic behaviour already for the as-deposited sample, as shown in Figure 4.9c.

In this sample we observe a very good preservation of passivation, probably connected with the capacities of the films to block metal diffusion. However we still are in the presence of transport issues that do not allow the tunnelling of carriers and thus do not form an ohmic contact. This is probably connected to the too many interfaces present in the structure that create too many barriers to transport. Unfortunately we could not test a structure with both LiF and TiO_2 layers made thinner.

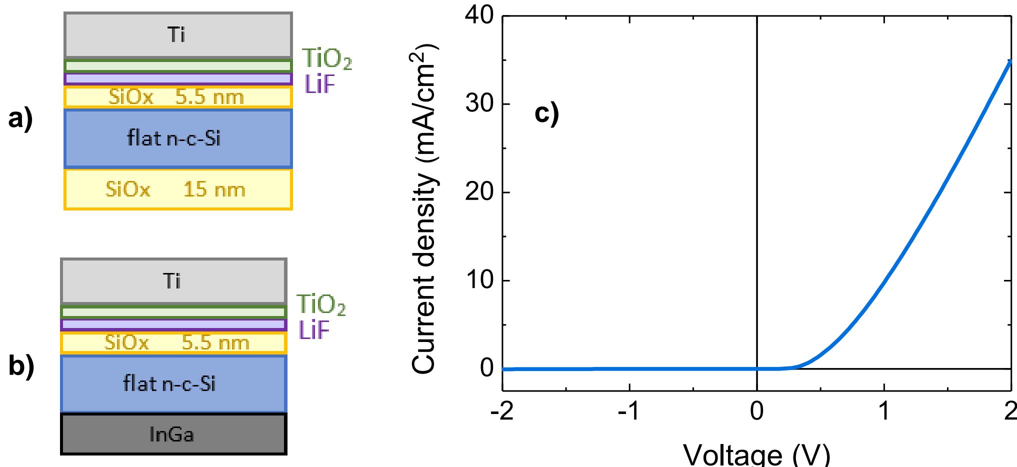

Figure 4.9 Structure of the samples used to test the $LiF/TiO_2/Ti$ base contact: a) sample for lifetime measurements; b) sample for J-V characterisation. c) J-V characteristics of the structure c-Si/SiOx/LiF/TiO_2/Ti (Sample 836). The contact is not ohmic.

4.3.4 MgF_2/Ti base contact

We then explored another ionic material suggested by the literature [17], namely MgF_2, to investigate also its behaviour (see Figure 4.10a and b). The layer was 1 nm thick (Sample 832), and the initial substrate lifetime of 3.1 ms was increased to 3.7 ms after deposition. Similarly to the case LiF, also the contact was ohmic in the as-deposited sample, as shown in Figure 4.10c. However after annealing the lifetime decreased to 230 µs, revealing even in this case a complete deterioration of the passivation. Again, probably Ti had diffused inside the structure and caused the damage to passivation.

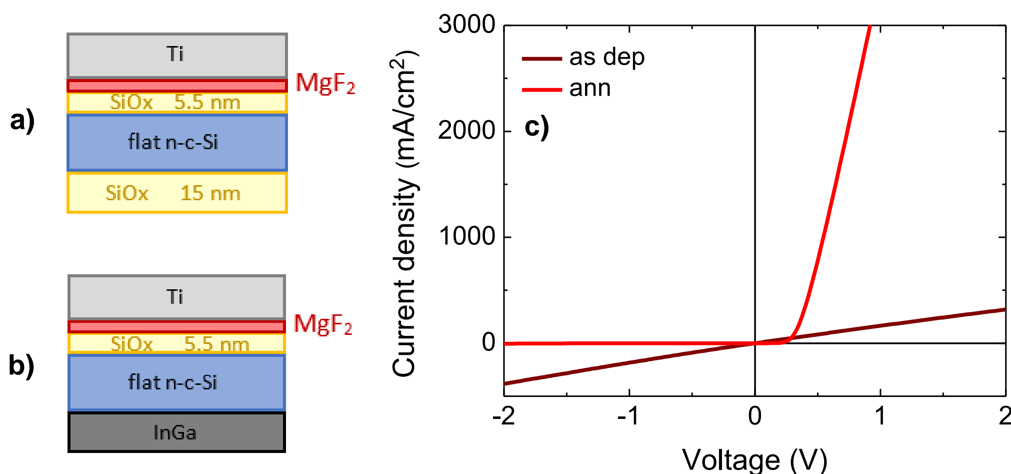

Figure 4.10 Structure of the samples used to test the MgF_2/Ti base contact: a) sample for lifetime measurements; b) sample for J-V characterisation. c) J-V characteristics of the structure c-Si/SiOx/MgF_2/Ti (Sample 832) before and after annealing.

Some side investigations showed that the damage to passivation happened after the Ti deposition and annealing while, before Ti deposition, the bare MgF_2 film was stable and preserved passivation even after an annealing. This could suggest the use of annealed MgF_2 films in future experiments.

4.3.5 MgF_2/ZnS/Ti base contact

The last structure that we tested was an MgF_2/ZnS bilayer with film thicknesses of 1 nm and 0.7 nm respectively (Sample 837), taking suggestion from the literature [18]. The initial lifetime of 2.7 ms was only slightly damaged after the deposition of the contact (2.3 ms), and was almost preserved after annealing (2.2 ms). The J-V characteristic was ohmic before deposition, but again rectifying after annealing, as shown in Figure 4.11.

Up to this point this was the structure which allowed the formation of an ohmic contact which best preservation of passivation after the annealing, and will be the starting point for future experimentations.

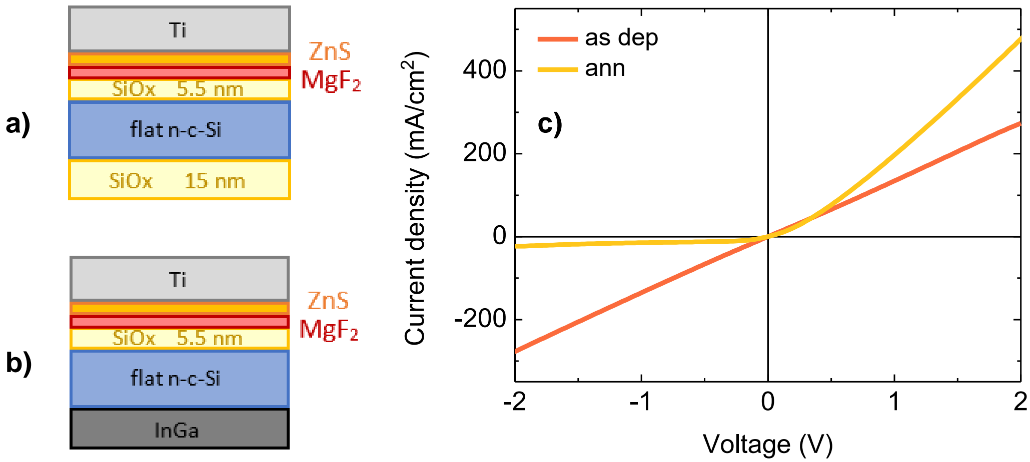

Figure 4.11 Structure of the samples used to test the MgF_2/ZnS/Ti base contact: a) sample for lifetime measurements; b) sample for J-V characterisation. c) J-V characteristics of the structure c-Si/SiOx/MgF_2/ZnS/Ti (Sample 837) before and after annealing.

4.3.6 Conclusion on base contacts

To sum up the results on barrier layers for base contacts, we have found three interlayers or double interlayers that have allowed the formation of ohmic contacts with the passivated c-Si substrate, namely LiF, MgF_2 and MgF_2/ZnS. All of them have preserved or only slightly reduced the initial substrate passivation, and are thus suited for application to c-Si heterojunctions.

The challenge was then to find contacts that could withstand a thermal annealing without loosing their characteristics. Unfortunately still none of the tested structures did fulfil the request. However some structures presented a good preservation of passivation after annealing, and will be further investigated.

4.4 Conclusions on materials for base contacts

We investigated the possibility of using a thermally-evaporated film of TiOx:W as ETL. The transparency and conductivity of the films was suitable for the application, but unfortunately when the film was grown on a passivated substrate it induced a strong lifetime degradation, and did not form an ohmic contact. This was ascribed to possible defects induced on the SiOx/TiOx:W interface, but also to a non-ideal band alignment. Both issues are most likely connected with the low-temperature deposition process, which is very different from the commonly-used ALD found in the literature. Further experiments are needed in order to check if low-temperature thermal evaporation can supply films with the desired behaviour.

We also examined different materials to be used as barrier layers between the SiOx passivating layer and the outer metallic contact. A TiO_2 interlayer did not allow the formation of an ohmic contact, even if it partially helped preserve passivation after annealing. This confirmed the fact that the current deposition method for TiO_2 is still not optimised. A structure with a LiF interlayer did perform an ohmic contact right after deposition, but became rectifying after annealing. The results confirm the fact, observed in Section 3.7.1, that the LiF layer is probably decomposed after annealing. A double LiF/TiO_2 interlayer gave rise to an increase in passivation even after annealing, but the complex nature of the structure did not allow the formation of an ohmic contact, even with very thin layers. A structure containing an MgF_2 interlayer also formed an ohmic contact, and the film was proven to be very effective in preserving passivation. MgF_2 performed even better in conjunction with ZnS, with an ohmic behaviour after deposition and a very good preservation of passivation after annealing. However for both structures the ohmic contact was not maintained after the thermal treatment.

In conclusion, some of the barrier layers actually did perform an effective protection of passivation, but still none of them was able to form an ohmic contact after annealing. This problem was connected with the defects or diffusions induced in the structure during film growth and after annealing, and most probably coming from the capping Ti metal layer. The best performing structure seems to be the MgF_2/ZnS bilayer, which could be then added to the list presented in [17] and which will be the starting point of the upcoming research. Future experiments should aim at individuating a low-temperature deposition procedure able to produce stable, non-diffusing films with low defects. The final goal would be their implementation into contacts in which the metal layer is replaced by a transparent conductive oxide layer in order to obtain a transparent ohmic contact for the n-side.

Results:

- The TiOx:W films grown in our laboratory are not suitable to be used as ETL in c-Si heterostructures, due to a non-optimal band alignment with c-Si.
- Several layers were tested to decouple the SiOx passivating layer from a metallic contact. LiF, MgF_2 and MgF_2/ZnS allowed the formation of an ohmic contact in the as-deposited samples and guaranteed the preservation of passivation.

Perspectives:

- Test different low-temperature deposition methods to deposit TiO_2 films.
- Search for layers that allow the formation of an ohmic contact after annealing.
- Substitute the metallic contact with a TCO.

References to Chapter 4

[1] D. A. H. Hanaor, C. C. Sorrell, “Review of the anatase to rutile phase transformation”, J. Mater. Sci. 46 (2011) 855.874. DOI: 10.1007/s10853-010-5113-0

[2] L. Franco Arias, A. Kleiman, A. Márquez, “Rutile titanium dioxide films deposited with a vacuum arc at different temperatures”, J. Phys. Conf. Ser. 370 (2011) 012027. DOI: 10.1088/1742-6596/370/1/012027

[3] R. Chierchia, F. Menchini, L. Serenelli, P. Mangiapane, T. Polichetti, M. Tucci, “Titanium oxide films deposited by e-beam evaporation as n-type electrode for solar cell applications”, Phys. Status Solidi C 13:10-12 (2016) 1002-1005. DOI: 10.1002/pssc.201600119

[4] X. Yang, P. Zheng, Q. Bi, K. Weber, “Silicon heterojunction solar cells with electron selective TiOx contact”, Sol. Energy Mater. Sol. Cells 150 (2016) 32-38. DOI: 10.1016/j.solmat.2016.01.020

[5] C. Lee, S. Bae, H. Park, D. Choi, H. Song, H. Lee, Y. Ohshita, D. Kim, Y. Kang, H.S. Lee, “Properties of thermally evaporated titanium dioxide as an electron-selective contact for silicon solar cells”, Energies 13 (2020) 678. DOI: 10.3390/en13030678

[6] Y. Liu, J. Zhang, H. Wu, W. Cui, R. Wang, K. Ding, S. T. Lee, B. Sun, “Low-temperature synthesis TiOx passivation layer for organic-silicon heterojunction solar cell with a high open-circuit voltage”, Nano Energy 34 (2017) 257-263. DOI: 10.1016/j.nanoen.2017.02.024

[7] B. S. Richards, J. E. Cotter, C. B. Honsberg, “Enhancing the surface passivation of TiO2 coated silicon wafers”, Appl. Phys. Lett. 80 (2002) 1123. DOI: 10.1063/1.1445810

[8] J. Bullock, Y. Wan, Z. Xu, S. Essig, M. Hettick, H. Wang, W. Ji, Mathieu Boccard, A. Cuevas, C. Ballif, A. Javey, “Stable dopant-free asymmetric heterocontact silicon solar cells with efficiencies above 20%”, ACS Energy Lett. 3 (2018) 508-513. DOI: 10.1021/acsenergylett.7b01279

[9] J. Bullock, Y. Wan, M. Hettick, X. Zhaoran, S. Pheng Phang, D. Yan, H. Wang, W. Ji, C. Samundsett, Z. Hameiri, D. Macdonald, A. Cuevas, A. Javey, “Dopant-free partial rear contacts enabling 23% silicon solar cells”, Adv. Energy Mater. 9 (2019) 1803367. DOI: 10.1002/aenm.201803367

[10] H. Kim, K. L. Ou, X. Wu, P. F. Ndione, J. Berry, Y. Lambert, T. Melin, N. R. Armstrong, S. Graham, “Investigation of ultra-thin titania films as hole blocking contacts for organic photovoltaics”, J. Mater. Chem. A 3 (2015) 17332. DOI: 10.1039/c5ta04687d

[11] X. Zhang, F. Liu, Q.L. Huang, G. Zhou, Z. S. Wang, “Dye-sensitized W-doped TiO_2 solar cells with a tunable conduction band and suppressed charge recombination”, J. Phys. Chem. C 115 (2011) 12665-12671. DOI: 10.1021/jp201853c

[12] https://thermtest.com/thermal-resources/materials-database

[13] P. Alén, M. Vehkamäki, M. Ritala, and M. Leskelä, “Diffusion barrier properties of atomic layer deposited ultrathin Ta_2O_5 and TiO_2 Films”, J. Electrochem. Soc. 153:4 (2006) G304-G308. DOI: 10.1149/1.2168389

[14] K. A. Nagamatsu, S. Avasthi, G. Sahasrabudhe, G. Man, J. Jhaveri, A. H. Berg, J. Schwartz, A. Kahn, S. Wagner, J. C. Sturm, “Titanium dioxide/silicon hole-blocking selective contact to enable double-heterojunction crystalline silicon-based solar cell”, Appl. Phys. Lett. 106 (2015) 123906. DOI: 10.1063/1.4916540

[15] X. Yang , Q. Bi , H. Ali , K. Davis , W. V. Schoenfeld, K. Weber, “High-performance TiO_2-based electron-selective contacts for crystalline silicon solar cells”, Adv. Mater. 28 (2016) 5891-5897. DOI: 10.1002/adma.201600926

[16] X. Yang, K. Weber, Z. Hameiri, S. De Wolf, “Industrially feasible, dopant-free, carrier-selective contacts for high-efficiency silicon solar cells”, Prog. Photovolt: Res. Appl. 25 (2017) 896-904. DOI: 10.1002/pip.2901

[17] Y. Wan, C. Samundsett, J. Bullock, T. Allen, M. Hettick, D. Yan, P. Zheng, X. Zhang, J. Cui, J. Anne McKeon, A. Javey, A. Cuevas, “Magnesium fluoride electron–selective contacts for crystalline silicon solar cells”, ACS Appl. Mater. Interfaces 8:23 (2016) 14671-14677. DOI: 10.1021/acsami.6b03599

[18] Y. Liu, Y. Sun, W. Liu, J. Yao, “Novel high-efficiency crystalline-silicon-based compound heterojunction solar cells: HCT (heterojunction with compound thin-layer)”, Phys. Chem. Chem. Phys. 16 (2014) 15400. DOI: 10.1039/c4cp00668b

Chapter 5

Indium tungsten oxide (IWO) as a high-mobility TCO

In this chapter the properties of indium tungsten oxide (IWO) films are investigated. Reactive and non-reactive sputtering deposition are employed as deposition methods for the samples, and it is shown that the latter, simpler, process permits to grow samples with very good optical and electrical properties that are suitable for applications in HJ solar cells. Part of the content of this chapter has been submitted for publication and has been presented in international conferences ([10, 14, 16] in the List of Publications).

5.1 Introduction

As introduced in Chapter 2, the main tasks a TCO should accomplish are a transparent and antireflection behaviour, in order to minimise losses of impinging radiation on the cell, and a low resistivity, in order to enhance lateral conductivity and efficiently lead carriers from the bottom layers to the outer metallic contacts. Besides these characteristics, which are at the basis of an efficient implementation of the material in HJ solar cells, also simple, non-expensive and high-throughput deposition methods are required for actual integration in industrial processes.

For decades indium tin oxide (ITO) has occupied a main place among TCOs. A substitute should have comparable properties and cheapness. From the optical point of view, it should have an absorption coefficient smaller than 10^4 cm^{-1} in the near-UV and Vis range and an optical band gap Eg>3 eV, while having an electrical resistivity around 10^{-4} Ω·cm [1]. As the thickness of the TCO is optimised on the base of optical constraints, the way to enhance the conductivity of the material avoiding free carrier absorption is to have a high mobility along with a low electron density. Moreover, to achieve very high cell efficiencies, the passivation of the crystalline silicon (c-Si) wafer surfaces by means of hydrogenated amorphous silicon (a-Si:H) [2] or hydrogenated silicon oxide (a-SiOx:H) [3, 4] must be preserved during the cell fabrication. Therefore also the effects of TCO deposition on possible recombination effects on the silicon surface and then on cell performances have to be carefully analysed.

Indium oxide has already shown to be suitable to host dopants other than tin and form high performance TCOs [5, 6]. Tungsten-doped indium oxide (IWO) is a promising solution to accomplish all the above-mentioned requests [7-14], and (in its hydrogen-doped version) it was recognized to be the only alternative to ITO to have found its way into industrial production [15].

A lot of literature has long sought for physical explanations of the simultaneous conduction and optical transparency in TCOs, often falling into an empirical approach, which still remains a shared choice. Many researchers have investigated the origin of high mobility in TCOs, revealing the main mechanisms governing this characteristic [13, 14, 16-22]. The high mobility of IWO films has then been ascribed to three main effects [9]: i) a reduced scattering activity of the ionised doping centres due to the high Lewis acidic strength of W^{6+} with respect to In^{3+} ions in the lattice, which enables a screening of the dopant's effective charge; ii) the high crystallinity of the samples, due to the small difference in the atomic radii of W^{6+} and In^{3+}; iii) the charged complexes that can be formed between W^{6+} and O^{2-} interstitial impurities, that are able to provide carriers while reducing the number of dopant scattering centres.

Radio-frequency (RF) sputtering has been recognised as one of the methods which brings to large mobility values due to the high energy of the plasma ions, which assists the crystal growth during deposition and leads to a better crystallographic and electronic quality of the material [20]. Even though the pulsed laser deposition (PLD) [23, 24] and reactive plasma deposition (RPD) [25-27] techniques can produce high mobility IWO films, RF sputtering remains the most employed technique in industrial plants of HJ cells manufacturing. The sputtering parameters definitely play a fundamental role in defining the characteristics of the films [8, 9, 11, 14, 28-31], so they have to be carefully tuned; however their mutual interactions make that a complete cross-variability test is difficult to be carried out. Oxygen and/or hydrogen added to argon in the sputtering reactive plasma are often reported in the literature as the way to obtain high-mobility IWO films, often aided by high temperatures and/or thermal annealing of the samples. Investigations have been performed on the influence of the gas partial pressures in the sputtering plasma mixture during the film growth. The results have shown a very high variability of values and trends for the electrical properties, thus demonstrating that a prediction of the best deposition conditions is very difficult, and that a wide range of performances is possible for IWO films. However, none of the works to our knowledge has investigated the possibility of growing IWO films by non-reactive RF plasma, i.e. in a pure Ar plasma, which would simplify the deposition process. Moreover, there seems to be a lack of results about the modifications of c-Si passivation after the deposition of IWO films, which is indeed a key factor when envisaging HJ solar cells applications.

In view of applications as a TCO, the deposition of IWO films by RF sputtering was tested. Starting from the same target of mixed-oxide composition (as detailed in the following), we grew films both in a pure argon plasma and in a reactive environment (i.e. with the addition of oxygen). The optoelectronic characterisation of the films was carried out, and the effects of the deposition on the passivation of the silicon substrate were investigated. Finally, the work function (WF) of the samples was evaluated and the films were integrated in heterojunction solar cells. All IWO films were deposited at the same time on both glasses and textured crystalline silicon substrates with an approximate thickness of 120 nm on glass and 80 nm on textured silicon.

5.2 IWO films deposited by reactive RF sputtering

IWO films were deposited by RF sputtering from a compound In_2O_3:WO_3=99:1 wt% target. The chamber pressure prior to the sputtering process was always kept under 4×10^{-7} mbar, while the samples were loaded in the system through a load-lock chamber to reduce contaminations. The RF power (P_{RF}) was varied between 60 and 300 W on a 170 cm² area target. For reactively-grown samples, 40 sccm of H_2 diluted (4%) in Ar and 0.5 sccm of O_2 were fluxed in the chamber to compose the plasma mixture. In the case of non-reactively sputtered samples, only a 40 sccm Ar flux was used. The total pressure was set at different values in the range between 1×10^{-3} and 1.5×10^{-2} mbar. The growth rate varied from 0.5 to 2.5 Å depending on the deposition conditions.

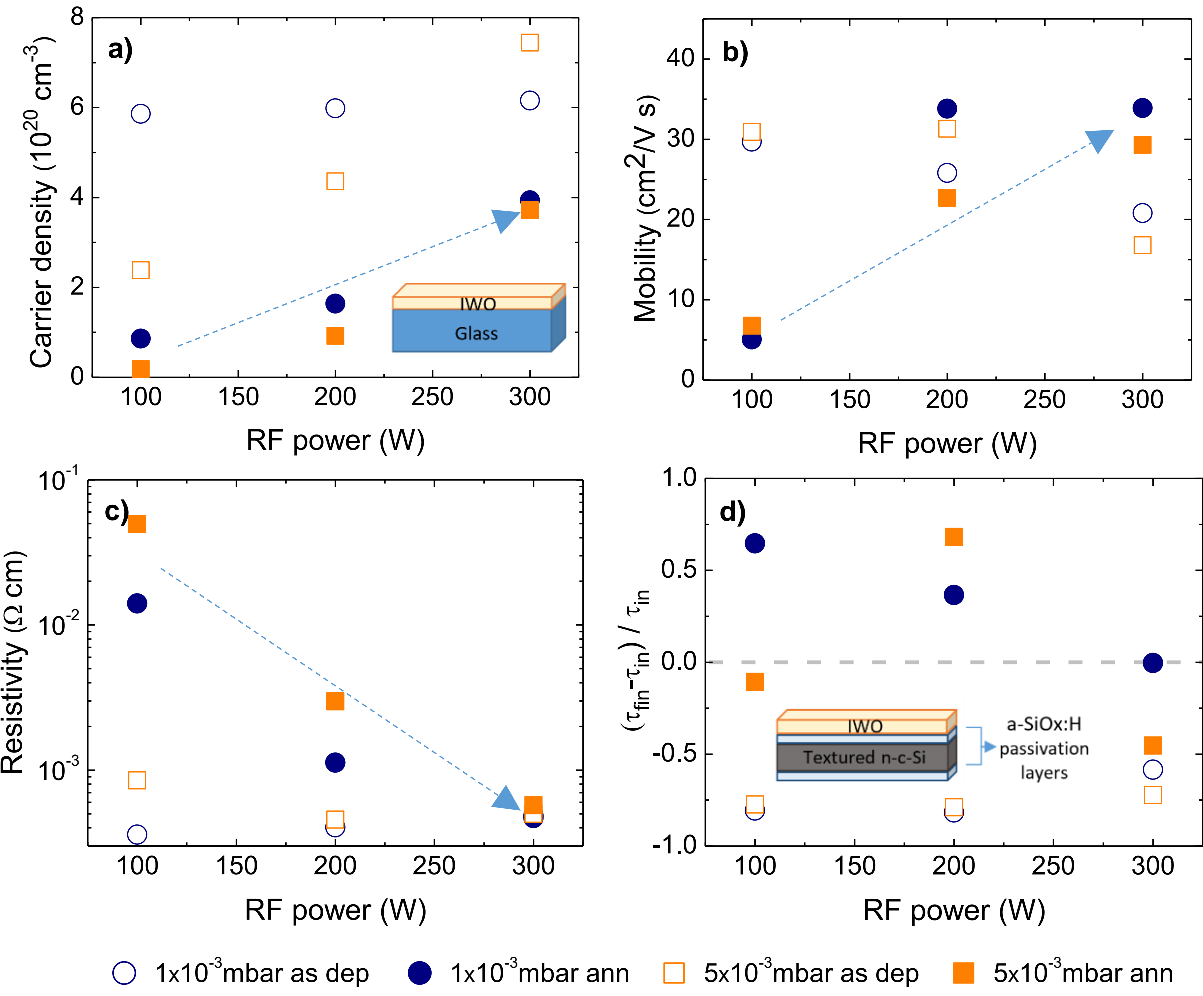

Figure 5.1 Variation of a) carrier density, b) mobility, c) resistivity and d) relative variation of substrate lifetime as a function of the RF power at two total pressure values for reactively-sputtered IWO films. Blue round and orange square symbols refer to samples deposited at a total pressure of 1×10^{-3} and 5×10^{-3} mbar, while empty and full symbols refer to samples measured before and after a thermal annealing treatment, respectively.

IWO films were deposited using different values for the RF power and the total working pressure. The electrical properties of the films are shown in Figure 5.1. The empty symbols are referred to samples measured right after deposition, while the full symbols refer to samples after thermal annealing. All samples show an n-type behaviour. The carrier densities (Figure 5.1a) visibly decrease for all samples after the thermal treatment, while mobilities (Figure 5.1b) show an opposite trend at low and high RF power values, i.e. they are reduced at 100 W and are increased at 300 W, evidencing that the films grown at different RF power are characterised by very different structures which are differently modified by the thermal treatment. As a consequence the resistivity values (Figure 5.1c) are strongly increased after annealing in samples grown at low RF power, while they show small changes at high RF power. The trends are very similar for batches of samples grown at the two tested values of total pressure of 1×10^{-3} and 5×10^{-3} mbar, showing no significant influence of this parameter on the electric properties of the films. Concerning the values after thermal annealing, it is found that samples grown at the lowest RF power (100 W) are characterised by a very low mobility (<10 $cm^2/V{\cdot}s$) which increases up to around 35 $cm^2/V{\cdot}s$ at a RF power of 300 W (Figure 5.1b); in the same range of RF power the carrier density increases from five to ten times in the range 0.4-5×10^{20} cm^{-3} (Figure 5.1a). As a consequence, at low RF power the resistivity is very high (between $7\text{x}10^{-2}$ and 5×10^{-3} $\Omega{\cdot}cm$), but when RF power is increased to 300 W it reaches values around 10^{-4} $\Omega{\cdot}cm$ (Figure 5.1c). Thus, from the point of view of charge transport, only sputtering at high RF power produces films that can be suitable for applications as TCOs. The observed differences in carrier densities could be due to different stoichiometry in samples grown in different deposition conditions, which could bring to different doping levels, while the difference in mobilities could be due to different grain boundary conditions. However, no XRD or SEM analysis were performed on the samples, which could confirm the hypothesis.

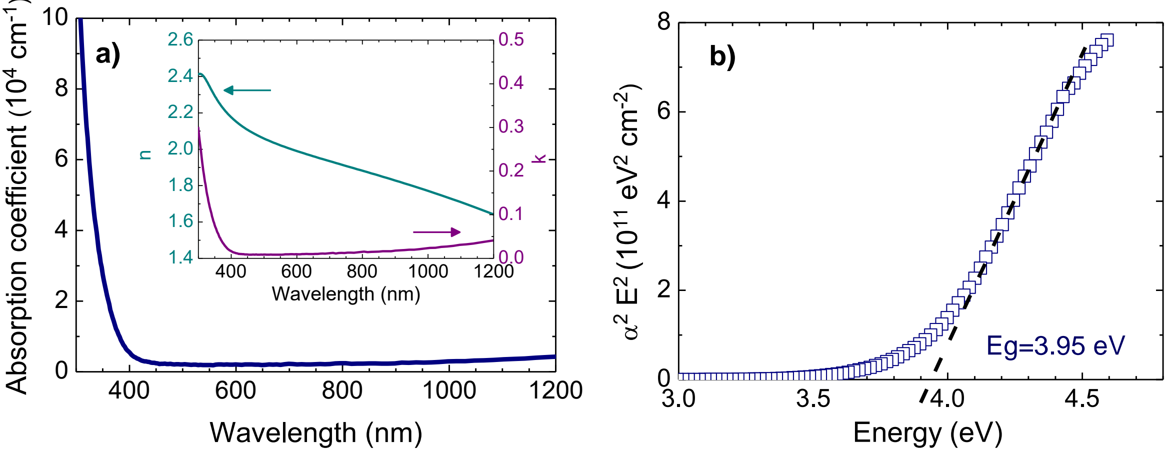

Figure 5.2 Optical characterization of an IWO film reactively grown at 300 W and 1×10^{-3} mbar: a) absorption coefficient (α) and complex refractive index (inset); b) Tauc plot to estimate the bandgap.

The samples grown at 300 W show a very low absorption in the 300-1200 nm wavelength range (Figure 5.2a), and a band gap energy Eg of 3.95 eV (Figure 5.2b). The refractive index is around 2 (inset in Figure 5.2a), and results suitable for anti-reflection (AR) purposes, being the geometric mean between the refractive indices of air and silicon.

In order to evaluate the effects on passivation, the IWO films were deposited on one side of n-type crystalline-silicon (n-c-Si) wafers passivated on both sides by a 15 nm-thick film of amorphous hydrogenated silicon oxide [4] and the minority carrier lifetime was measured. The relative variations of lifetime are reported in Figure 5.1d for samples grown in different conditions. It is well known [4] that the passivating properties of a-SiO_x:H can be deteriorated by the sputtering process, but they can be recovered after a thermal annealing treatment. So it was not surprising to observe a reduction of the minority carrier lifetime in the passivated samples after the deposition of the IWO films (Figure 5.1d). Unfortunately the subsequent thermal treatment was not always able to induce a complete restoration of the passivation quality measured before IWO film deposition; in particular the best-performing samples in terms of electronic properties (those deposited at 300 W) did not always recover the initial passivation level.

In summary, IWO films grown by reactive sputtering are found to be very sensitive to the deposition conditions, with resistivities that may vary of up to two orders of magnitude. It appears that obtaining the desired anti-reflecting and conducting characteristics is possible after a fine tuning of the deposition parameters, but in the presented case not all the best-performing samples were able to preserve the c-Si surface passivation.

5.3 IWO films deposited by non-reactive RF sputtering

It could be, though, very desirable to obtain optimal film characteristics with a simpler process. In this perspective, a series of samples was deposited at room temperature without adding either oxygen or hydrogen in the sputtering plasma gas mixture. First, two RF power values were chosen and the total pressure was varied. The measured electronic characteristics of the obtained IWO films are reported in Figure 5.3. All samples show an n-type behaviour. Similarly to reactively-sputtered samples, mobilities increase after the thermal annealing treatment (Figure 5.3b) and, notwithstanding some variable behaviour of the carrier concentration, the resistivities are reduced. Maximum values of mobilities, with a top value of 70.9 $cm^2/V \cdot s$, associated to low resistivities, are found for 1-1.5×10^{-2} mbar total pressure for both values of RF power.

Starting from these results, a wider RF power range at 1×10^{-2} mbar was investigated, and the results are shown in Figure 5.4. In all films the thermal treatment had the effect to reduce the carrier concentration, increase the mobility and decrease the resistivity, therefore only data after thermal annealing are reported in the graphs. The annealed samples show average mobilities above 50 $cm^2/V \cdot s$ for samples grown at RF powers up to 200 W, average carrier densities of 2-3×10^{20} cm^{-3} and resulting average resistivities below 4×10^{-4} $\Omega \cdot cm$, which are comparable to values reported in

the literature for sputtered samples [9, 11, 15, 28-31]. Maximum mobilities of 70.9 cm²/V·s are measured, which compared to values reported in the literature are only surpassed in high-temperature processes or in RPD at 200°C [27]. The drop in mobility observed for high sputtering powers could be due to defects induced in the lattice by the fast process. It is interesting to note that, independently from the RF power, the resistivities of all samples grown without the addition of oxygen and hydrogen in the plasma gas mixture are of the same order of magnitude, which is a quite different behaviour with respect to the reactively-sputtered samples. Moreover, while thermal annealing causes an improvement of mobility and conductivity in all these latter samples, regardless of deposition conditions, in the case of the reactively-sputtered samples there was no unique trend. This is the indication that all the non-reactively deposited samples share similar properties in terms of crystallinity, grain dimensions and impurity content, which confirms the overall process stability. All the results are comparable to those reported in the already cited literature for reactively-sputtered samples, and confirm the very good characteristics of the IWO films.

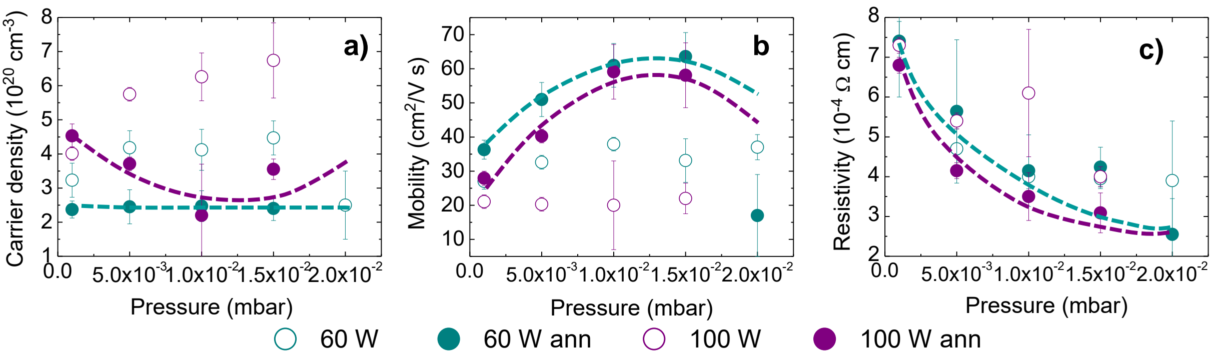

Figure 5.3 Variation of a) carrier density, b) mobility and c) resistivity as a function of the total pressure at two RF power values for non-reactively sputtered IWO films. Blue and purple symbols refer to samples deposited at a RF power of 60 and 10 W, respectively, while empty or full symbols refer to samples before and after a thermal annealing treatment, respectively. The dashed lines are guides for the eye for full symbols only.

For what concerns passivation, the initial lifetime of the wafers is lowered by the IWO film deposition, as expected, and the values are not reported here. However, differently form the reactively-sputtered samples of Figure 5.1d, the lifetime of the passivated samples is fully recovered and even improved after the subsequent thermal annealing for all deposition conditions, as can be seen in Figure 5.4d. This effect implies that the non-reactive sputtering IWO deposition does not permanently damage the underlying passivation, which can be recovered after thermal processing. This finding is very positive, as it is crucial to achieve high efficiencies in HJ solar cells that have to undergo the thermal processes required by the manufacturing processes.

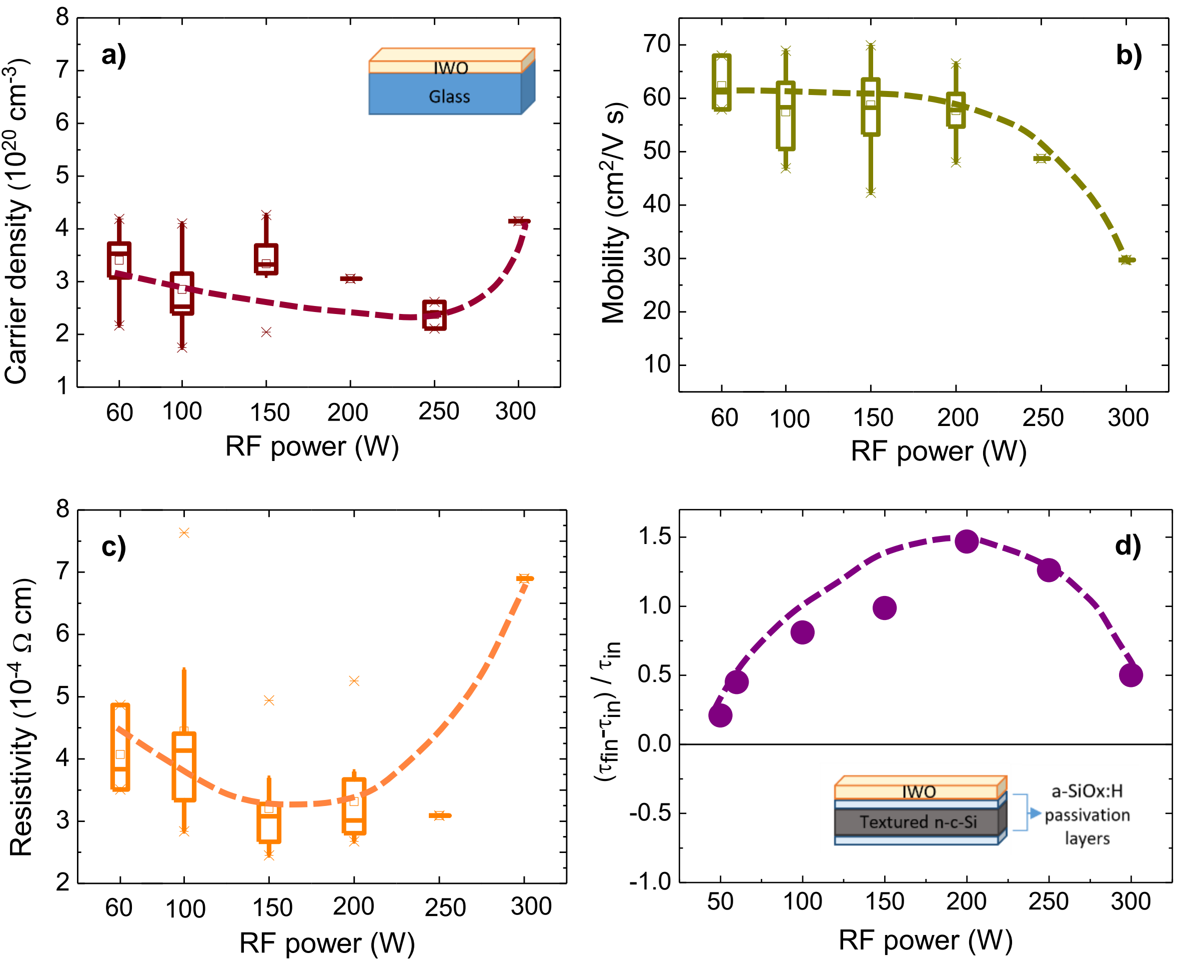

Figure 5.4 Variation of a) carrier density, b) mobility, c) resistivity and d) relative variation of lifetime as a function of RF power for non-reactively sputtered IWO films. Only values after thermal annealing are reported. The dashed lines are guides for the eye.

The samples were further characterised in order to better understand their behaviours. Figure 5.5 shows the optical characteristics of two films grown in different conditions and having quite different Hall parameters after thermal annealing (see Table 5.1 for details). Both samples show a high transparency in the UV-Vis-NIR range, with absorption coefficients in the Vis-NIR range lower than 10^4 cm^{-1} (Figure 5.5a). The absorption coefficient of Sample B slightly increases in the NIR range, reflecting the higher carrier density with respect to Sample A. The refractive indices have a similar value around 2 (inset in Figure 5.5a), as necessary for best AR coupling; the Eg values derived from the Tauc plots (Figure 5.5b) are around 3.95-4.0 eV, with a slight increase in Sample B (which has a higher free carriers density) as predicted by the Burstein-Moss theory. All samples show similar optical characteristics.

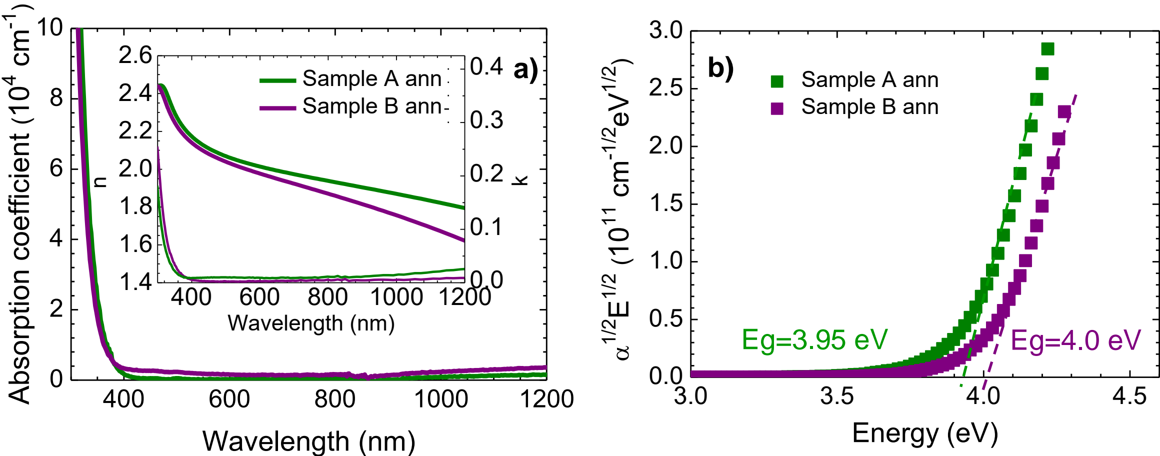

Figure 5.5 Comparison between a) the absorption coefficients, complex refractive indices (inset) and b) Tauc plots for two annealed IWO films with different electrical characteristics (see Table 5.1 for details).

Table 5.1 Growth conditions and Hall parameters for two selected IWO films after thermal annealing.

Sample	P_{RF} (W)	p (mbar)	R (Ω· cm)	N (cm^{-3})	μ (cm^2/V·s)
A ann	60	0.015	4.7×10^{-4}	2.1×10^{20}	50.2
B ann	200	0.010	2.8×10^{-4}	3.5×10^{20}	62.3

In order to correlate the effect of the thermal treatment on the electrical and optical characteristics with the structural properties of the IWO films, XRD and XPS spectra were measured. The XRD spectra of the two samples indicated in Table 1 are shown in Figure 5.6, where the typical peaks of the In_2O_3 cubic bibixyte [JCPDS file no. 71-2195] are recognised. Figure 5.6a refers to Sample A after annealing and shows the main reflections corresponding to the (222), (211) and (440) planes, indicating that the IWO film keeps the polycrystalline cubic In_2O_3 structure. The diffractogram referred to Sample B after annealing, reported in Figure 5.6b, shows a very different crystalline arrangement, with the appearance of the (400) preferred orientation. It can also be seen (Figure 5.6b) that the film before annealing is almost amorphous, showing hints of a possible preferential orientation along the (22) and (332) planes. The crystallinity dramatically improves after the thermal annealing, which is a well-known effect of high temperature during or post deposition [8]. It is known that the crystalline orientation of In_2O_3 films depends on the deposition process [32], and the preferred (400) orientation could be the reason of the higher mobility of Sample B, as observed also in [30].

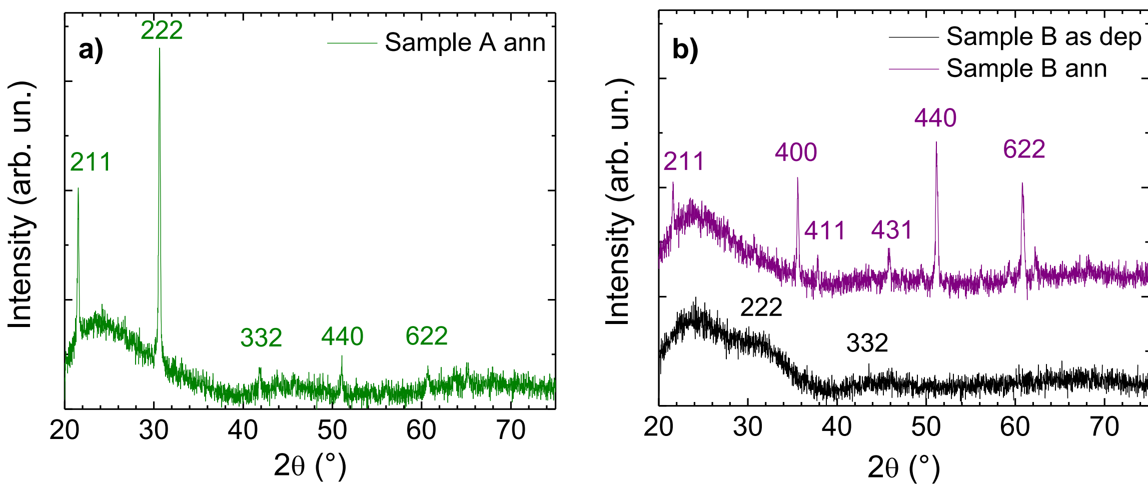

Figure 5.6 XRD spectra of two IWO film with different electrical characteristics (see Table 5.1).

The XPS analysis of sample B before and after annealing shows the signals for In3d, O1s, W4f (Figure 5.7) as the main constituents of the films. The signal of C1s from adventitious contamination is also present, but is not shown here. No signals from other elements were detected. The In3d spectra display the two $3d_{5/2}$ and $3d_{3/2}$ peaks at 444.6 and 452.2 eV, respectively, which correspond to the binding energy of In^{3+} in In_2O_3 [33]. The normalised spectra of In3d and W4f are almost coincident, proving that the In_2O_3 lattice network is not modified by the thermal treatment. The W4f spectra show a double-peak structure centred at 35.9 eV and 37.4 eV, which confirms that tungsten is bond to oxygen, probably in the W^{6+} valence state [34]. The O1s profile can be decomposed in two bands centred at 529.9 (O_I) and 531.7 eV (O_{II}), not reported in the graph. The low binding energy (BE) O_I band can be attributed to O^{2-} interstitial ions in the tetrahedral In_2O_3 lattice, while the O_{II} band can be attributed to oxygen ions in the oxygen deficient regions or oxygen atoms in the amorphous phase [35]. The O_I/O_{total} and O_I/In_{444} ratios were calculated (see Table 5.2), and the slightly higher value found for the annealed sample can be related to improved crystallinity after the thermal treatment, in agreement with the XRD data. The O_{tot}/In_{tot} and W_{tot}/In_{tot} ratios in the two samples show very small differences if compared to those observed in the literature when comparing samples with different doping concentrations [36], so that they can be considered as almost equivalent This may suggest that the main effect of the thermal annealing in nitrogen atmosphere is to improve crystallinity, and that the reduced carrier concentration in the annealed sample could be due to a reduced activation of the doping atoms. These observations could provide an explanation for the simultaneous increased mobility and reductions of carrier concentration in the films after annealing.

In summary, all samples grown without the addition of oxygen or hydrogen to the sputtering plasma show very good electro-optical characteristics, in line with those presented in the already reported literature but here obtained with a simplified process. All samples after annealing show a

simultaneous decrease in carrier concentration and an increase in mobility, which results in a reduced resistivity. In addition to the electro-optical performances, the passivation of c-Si substrates is maintained after IWO deposition and a subsequent thermal treatment at 200°C.

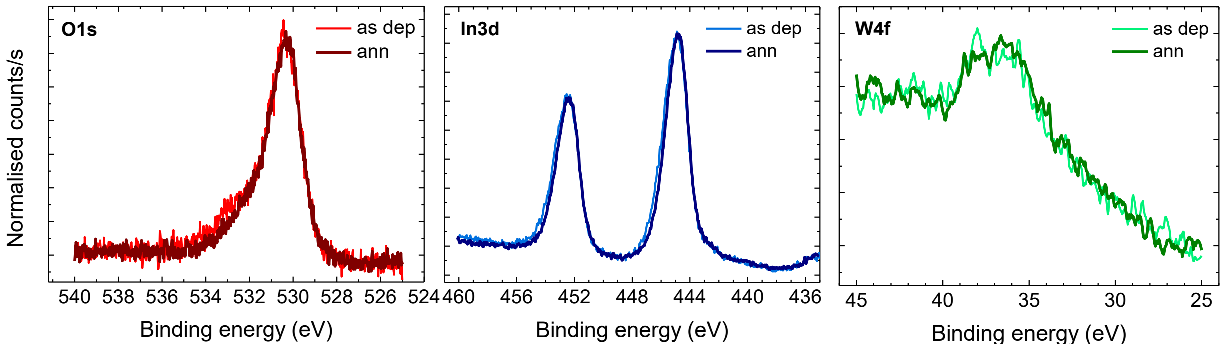

Figure 5.7 XPS normalised spectra of the composing elements of an IWO film measured after deposition and after the thermal treatment.

Table 5.2 Ratios of band areas from XPS signals in sample B (see Table 5.1) before and after annealing.

Sample	O_I/O_{total}	O_I/In_{444}	O_{tot}/In_{tot}	W_{tot}/In_{tot}
B as dep	0.59	0.66	1.10	0.009
B ann	0.63	0.75	1.12	0.010

As a final remark, it can be observed that the error bars in Figure 5.3 and Figure 5.4 result from data collected over more than 40 samples, which also provides an idea of the process stability. Similar variances are also evident in other works [28, 37], thus inviting to the challenge for an investigation of their origin. After some tests we have concluded that the variability strongly depends on the “history” of the target, i.e. from how long the target has been sputtered with or without oxygen and at which temperature, which, in turn, determines the oxygen content in the ceramic target that is a well-known issue also for reactively-sputtered samples [29]. The effect of oxygen content on the films characteristic is, in fact, widely reported in the literature [8, 9, 29]. Moreover, a slight trend was found in the data with the aging of the target, i.e. a reduction of mobility and an increase in carrier concentration, suggesting a compositional variation of the target due to preferential sputtering of the metal cations or to oxygen deficiency. It has to be added that the sputtering equipment is not dedicated only to IWO deposition, but also to the growth of other materials, as commonly happens in research laboratories. More efforts and experiments are needed in order to define a presputtering routine that would increase the repeatability of results and avoid modifications of the target.

5.4 Heterojunctions containing IWO films as TCO

As described in the previous paragraphs, even if the stability of the RF deposition process still needs some refining, we were able to find particular deposition conditions for which the deposited IWO films are highly transparent and possess a high mobility that ensured them a high conductivity. To demonstrate the applicability of the material to complete solar cells, we then realised several devices.

5.4.1 Work function evaluation

In addition to the already discussed electro-optical characteristics and the capability to maintain the wafer passivation, another fundamental feature of a TCO is its work function. This parameter assesses the suitability of the material to be applied to the n-transport or to the p-transport contact [38-40]. Direct WF measurements on films, for example by ultraviolet photoelectron spectroscopy or kelvin probe, can only estimate the WF at the free surface of a sample, which is affected by external contaminations. Nevertheless, the only value of WF that can be useful for band-alignment considerations should be measured at the interface with the underlying passivating layer. In order to determine this WF value we proposed a method [38] for any kind of TCO film for HJ solar cells, involving the measurement of J-V characteristics at different temperatures of the electron-selective contact completed with a TCO film and subsequently thermally annealed (see Section 2.3.5 for details on the method). All annealed samples show linear or almost-linear J-V characteristics at RT and even at low temperatures (see Figure 5.8a for a representative sample), evidencing that no barrier to electron collection is present at the contact, and indicating that the WF of IWO film lines up with the Fermi level in c-Si wafer without forming a depleted region. In the case of the temperature dependence of J-V characteristics depicted in Figure 5.8a, it can be inferred that the WF of the IWO films is lower than 4.2 eV.

After the whole campaign of IWO characterisation, we monitored the WF values, and we found that for more recent samples the results were very different from those of some months before, as shown in Figure 5.8b: in this case the characteristic is rectifying at all temperatures, showing that a transport issue has arisen. This can be correlated to an increase in the WF of the IWO film, evaluated in ~4.4 eV. We could not perform any test to verify where these differences came from. However we hypothesise that they could be connected to the fact that our sputtering apparatus is not dedicated to a single process (namely room-temperature non-reactive IWO deposition), but it hosts several experiments that are performed in different experimental conditions. This could have caused some modifications in the target, as already discussed in the previous section.

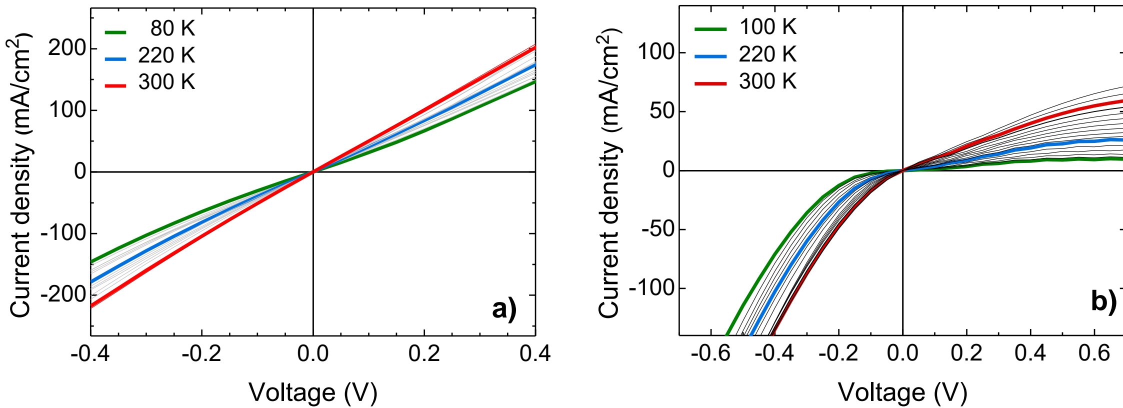

Figure 5.8 J-V characteristics at different temperatures to test the nature of the contact formed by IWO films on half cells. a) Samples deposited at the beginning of the campaign; b) samples deposited after some months.

Further investigations would be very interesting in order to understand the observed differences. Moreover, information on the work function of IWO films seem to be lacking in the literature, so that this could be an interesting topic to tackle. In particular, it could be tested if growing the samples at high temperature would result in films with a different work function, similarly to what happens for ITO.

5.4.2 Solar cells

Several solar cells were produced during all the experimentation campaign. Standard HJ cells were covered with the same IWO films on both sides, subsequently thermally annealed and contacted on both sides with an Ag grid deposited by screen printing of a low curing-temperature silver paste. The specific contact resistivity (ρ_c) between the IWO films and the Ag grid is another important parameter in complete devices, which must be low in order to minimise its contribution to total series resistance. The ρ_c was measured with the TLM method, and a ρ_c(IWO)=2.84 m$\Omega\cdot$cm^2 on a 120 nm-thick film with sheet resistance ρ_{sh}=54 $\Omega/\square$ was obtained.

A representative J-V characteristic is reported in Figure 5.9(left) and shows an evident s-shape which contributes to the poor overall cell efficiency. This result was somehow expected because the same type of IWO film (with a WF≤4.2 eV) was used for both selective contacts of the cell. It is known, though (see also Section 2.3.4), that the best solution to obtain a high-efficiency HJ cell would be the use of two different TCO layers: one with a high work function (WF≈5.2 eV) on the emitter side and another with a lower work function (WF≈4.1 eV) at the base contact, in order to respectively collect holes and electrons without affecting the Fermi level position at the edges of the cell; if an intermediate WF value is used for both sides, the J-V characteristics could be affected by an s-shape that reveals a barrier against carrier collection. The expectations were confirmed by

isolating the two selective contacts by means of a chemical etching and separately characterizing the J-V behaviour of both contacts: while the base behaves almost linearly, the emitter side evidences the presence of barriers to carrier transport (Figure 5.9 right). It is thus confirmed that the IWO WF value, around 4.2 eV, is not appropriate to complete the hole-selective contact.

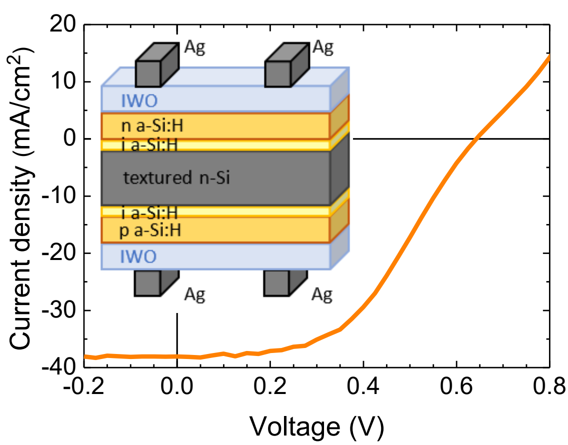

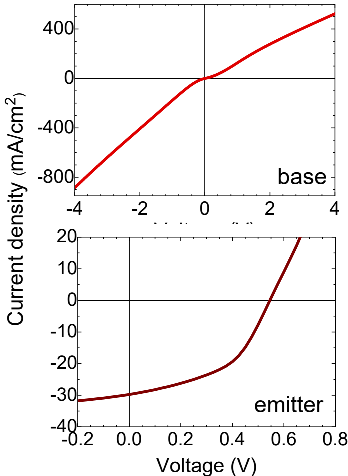

Figure 5.9 J-V light characteristic of the sketched cell (left) and of the separate base and emitter contact (right).

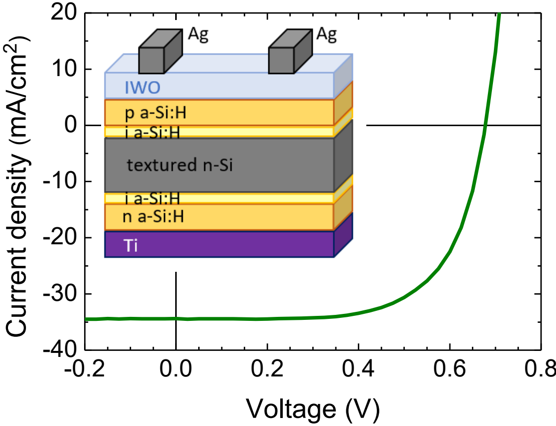

Figure 5.10 J-V light characteristic of the sketched cell.

On the other side, similar cells produced several months later confirmed the above-described WF shift. In this case the IWO film on the n-side was replaced by a full Ti metallic layer, which ensured an ohmic contact. The cell J-V characteristic, shown in Figure 5.10, does not show any undesired s-shape, evidencing that the transport issue at the emitter side is reduced. This is explained with the increased WF of the IWO films that was observed in the latest period of experimentation. The cell FF of 72.1% is still limited by the non-optimised screen-printed front grid and correlated contact resistivity with the IWO film. Moreover the 50 nm-thick Ti film on the

back, though ensuring the ohmic contact, should be thickened to further reduce series resistance. These last results show that in principle it is possible to control the WF of the IWO films.

5.5 Summary, conclusions and future perspectives

IWO is a promising material for applications as TCO in HJ solar cells. The necessary characteristics of the films are: high transparency in the UV-Vis-NIR spectrum and wide bandgap to reduce optical losses, high conductivity and low contact resistivity with the metal grid to reduce series resistance, guarantee that the RF sputtering damage on passivation can be recovered to minimize recombination losses and adequate work function for carrier selectivity.

RF sputtering is the most employed deposition technique in industrial applications, so we have tested the possibility of depositing IWO films with the desired characteristics by a simple non-reactive RF sputtering process. We have produced films which possess high mobility after thermal annealing, up to 70.9 cm/V·s, together with low carrier concentrations of $2\text{-}4\times10^{20}$ cm^{-3}, which results in resistivities as low as 2.5×10^{-4} Ω·cm, and are also characterised by a high transparency in the UV-Vis-NIR range. The deposition of the films is not detrimental for the passivation of the c-Si substrates, as the minority carrier lifetime is recovered or even surpassed after a thermal treatment which simulates the temperature changes experimented by the cells during the production process.

We have observed that the sputtering target is changed after a long working time, and we have hypothesised that this depends on the target “history”. The target modifications have brought to fluctuations in the electro-optical characteristics of the films, but always in the range where they appear suitable for employment in high-efficiency HJ solar cells. We are confident that a higher stability in the process could be achieved by optimizing a pre-sputtering treatment in a mixed $Ar+O_2$ plasma. The WF of the IWO films has been estimated, and has been found to vary, as well, approximately in the range 4.2-4.4 eV. This gives way for an optimisation process to obtain customised films characteristics optimised for both types e of selective contact. Sample heating (at temperatures lower than 200°C) during the growth can be tested, also with the aim of changing the work function on the films.

Results:

- IWO films with high UV-Vis transparency, high mobility, low carrier density and low resistivity can be grown by RF sputtering in a pure Ar atmosphere
- The IWO deposition is not detrimental for the substrate passivation, which can be recovered after a thermal annealing

Perspectives:

- Investigate possible variations of the target that bring to differences in the characteristics of the deposited films

References to Chapter 5

[1] R. A. Afre, N. Sharma, M. Sharon, M. Sharon, "Transparent conductive oxide films for various applications: a review", Rev. Adv. Mater. Sci. 53 (2018) 79-89. DOI: 10.1515/rams-2018-0006

[2] M. Tanaka, M. Taguchi, T. Matsuyama, T. Sawada, S. Tsuda, S. Nakano, H. Hanafusa, Y. Kuwano, "Development of new aSi/c-Si heterojunction solar cells: ACJ-HIT (Artificially Constructed Junction-Heterojunction with Intrinsic Thin layer)", Jpn. J. Appl. Phys. 31 (1992) 3518-3522. DOI: 10.1143/JJAP.31.3518

[3] H. Fujiwara, T. Kaneko, M. Kondo, "Application of hydrogenated amorphous silicon oxide layers to c-Si heterojunction solar cells", Appl. Phys. Lett. 91 (2007) 133508. DOI: 10.1063/1.2790815

[4] L. Serenelli, L. Martini, L. Imbimbo, R. Asquini, F. Menchini, M. Izzi, M. Tucci, "Metastability of a-SiOx:H thin films for c-Si surface passivation", Appl. Surf. Sci. 392 (2017) 430-440. DOI: 10.1016/j.apsusc.2016.09.026

[5] S. Calnan, A. N. Tiwari, "High mobility transparent conducting oxides for thin film solar cells", Thin Solid Films 518 (2010) 1839-1849. DOI: 10.1016/j.tsf.2009.09.044

[6] T. Koida, Y. Ueno, H. Shibata, "In2O3-based transparent conducting oxide films with high electron mobility fabricated at low process temperatures", Phys. Status Solidi A 2015 (2018) 1700506. DOI: 10.1002/pssa.201700506

[7] Z. Y. Hu, J. Zhang, X. Chen, S. Ren, Z. Hao, X. Geng, Y. Zhao, "Performance of electron beam deposited tungsten doped indium oxide films as anodes in organic solar cells", Sol. Energy Mater. Sol. Cells 95 (2011) 2173. DOI: 10.1016/j.solmat.2011.03.020

[8] Y. Abe, N. Ishiyama, "Polycrystalline films of tungsten-doped indium oxide prepared by d.c. magnetron sputtering", Mater. Lett. 61 (2007) 566-569. DOI: 10.1016/j.matlet.2006.05.010

[9] C. Han, Y. Zhao, L. Mazzarella, R. Santbergen, A. Montes, P. Procel, G. Yang, X. Zhang, M. Zeman, O. Isabella, "Room-temperature sputtered tungsten-doped indium oxide for improved current in silicon heterojunction solar cells", Sol. Energy Mater. Sol. Cells 227 (2021) 111082. DOI: 10.1016/j.solmat.2021.111082

[10] J. G. Kim, J. E. Lee, S. M. Jo, B. D. Chin, J. Y. Baek, K. J. Ahn, S. J. Kang, H. K. Kim, "Room temperature processed high mobility W-doped In2O3 electrodes coated via in-line arc plasma ion plating for flexible OLEDs and quantum dots LEDs", Sci. Rep. 8 (2018) 12019. DOI: 10.1038/s41598-018-30548-w

[11] X. Li, Q. Zhang, W. Miao, L. Huang, Z. Zhang, "Transparent conductive oxide thin films of tungsten-doped indium oxide", Thin Solid Films 515 (2006) 2471-2474. DOI: 10.1016/j.tsf.2006.07.014

[12] H. Wang, D. Zhang, Y. Luo, X. Zhao, F. Luo, L. Huang, Y. Li, W. Wang, "Fabrication and study of laser-damage-resistant transparent conductive W-doped In2O3 films", J. Phys. D: Appl. Phys. 44 (2011) 215101. DOI: 10.1088/0022-3727/44/21/215101

[13] M. Yang, J. Feng, G. Li, Q. Zhang, "Tungsten-doped In2O3 transparent conductive films with high transmittance in near-infrared region", J. Cryst. Growth 310 (2008) 3474-3477. DOI: 10.1016/j.jcrysgro.2008.05.012

[14] J. H. Kim, Y.H. Shin, T.Y. Seong, S.I. Na, H.K. Kim, "Rapid thermal annealed WO3-doped In2O3 films for transparent electrodes in organic photovoltaics", J. Phys. D: Appl. Phys. 45 (2012) 395104. DOI: 10.1088/0022-3727/45/39/395104

[15] A. Cruz, D. Erfurt, R. Köhler, M. Dimer, E. Schneiderlöchner, B. Stannowski, "Industrial TCOs for SHJ solar cells: approaches for optimizing performance and cost", PV magazine 44 (2020) 86-96. www.pv-tech.org

[16] J. Yu, J. Bian, W. Duan, Y. Liu, J. Shi, F. Meng, Z. Liu, "Tungsten doped indium oxide film: ready for bifacial copper metallization of silicon heterojunction solar cells", Sol. Energy Mater. Sol. Cells 144 (2016) 359-363. DOI: 10.1016/j.solmat.2015.09.033

[17] G. J. Exarhos, X.D. Zhou, "Discovery-based design of transparent conducting oxide films", Thin Solid Films 515 (2007) 7025-7052. DOI: 10.1016/j.tsf.2007.03.014

[18] K. Ellmer, R. Mientus, "Carrier transport in polycrystalline transparent conductive oxides: a comparative study of zinc oxide and indium oxide", Thin Solid Films 516 (2008) 4620-4627. DOI: 10.1016/j.tsf.2007.05.084

[19] A. Valla, P. Carroy, F. Ozanne, D. Muñoz, "Understanding the role of mobility of ITO films for silicon heterojunction solar cell applications", Sol. Energy Mater. Sol. Cells 157 (2016) 874-880. DOI: 10.1016/j.solmat.2016.08.002

[20] K. Ellmer, "Magnetron sputtering of transparent conductive zinc oxide: relation between the sputtering parameters and the electronic properties", J. Phys. D: Appl. Phys. 33 (2000) R17. DOI: 10.1088/0022-3727/33/4/201

[21] Y. Zhang, "Electronegativities of elements in valence states and their applications. 2. A scale for strengths of lewis acids", Inorg. Chem. 21:11 (1982) 3889-3893. DOI: 10.1021/ic00141a006

[22] S. J. Wen, G. Campet, J. Portier, G. Couturier, J. B. Goodenough, "Correlations between the electronic properties of doped indium oxide ceramics and the nature of the doping element", Mater. Sci. Eng. B 14 (1992) 115-119. DOI: 10.1016/0921-5107(92)90339-B

[23] R.K. Gupta, K. Ghosh, S.R. Mishra, P.K. Kahol, "High mobility W-doped In2O3 thin films: dffect of growth temperature and oxygen pressure on structural, electrical and optical properties", Appl. Surf. Sci. 254 (2008) 1661-1665. DOI: 10.1016/j.apsusc.2007.07.146

[24] P. F. Newhouse, C. H. Park, D. A. Keszler, J. Tate, P. S. Nyholm, "High electron mobility W-doped In2O3 thin films by pulsed laser deposition", Appl. Phys. Let. 87 (2005) 112108. DOI: 10.1063/1.2048829

[25] S. Huang, W. Liu, X. Li, Z. Li, Z. Wu, W. Huang, Y. Yang, K. Jiang, J. Shi, L. Zhang, F. Meng, Z. Liu, "Prolonged annealing improves hole transport of silicon heterojunction solar cells", Phys. Status Solidi -Rapid Res. Lett. 15 (2021) 2100015. DOI: 10.1002/pssr.202100015

[26] Z. Lu, F. Meng, Y. Cui, J. Shi, Z. Feng and Z. Liu, “High quality of IWO films prepared at room temperature by reactive plasma deposition for photovoltaic devices”, J. Phys. D: Appl. Phys. 46 (2013) 075103. DOI: 10.1088/0022-3727/46/7/075103

[27] F. Meng, J. Shi, Z. Liu, Y. Cui, Z. Lu, Z. Feng, “High mobility transparent conductive W-doped In2O3 thin films prepared at low substrate temperature and its application to solar cells”, Sol. Energy Mat. Sol. Cells 122 (2014) 70-74. DOI: 10.1016/j.solmat.2013.11.030

[28] G. Christmann, “High mobility IWO for improved current in heterojunction technology solar cells”, Zenodo (2018). DOI: 10.5281/zenodo.1744966

[29] Y. Abe, N. Ishiyama, H. Kuno, K. Adachi, “Amorphous indium tungsten oxide films prepared by DC magnetron sputtering”, J. Mater. Sci. 40 (2005) 1611-1614. DOI: 10.1007/s10853-005-0660-5

[30] Y. Li, W. Wang, J. Zhang, R. Wang, “Preparation and properties of tungsten-doped indium oxide thin films”, Rare Met. 31:2 (2012) 158. DOI: 10.1007/s12598-012-0483-x

[31] J. Pan, W. Wang, D. Wu, Q. Fu, D. Ma, “Tungsten doped indium oxide thin films deposited at room temperature by radio frequency magnetron sputtering”, J. Mater. Sci. Technol. 30:7 (2014) 644-648. DOI: 10.1016/j.jmst.2013.10.023

[32] Y. Shigesato, D.C. Paine, “A microstructural study of low resistivity tin-doped indium oxides prepared by d.c. magnetron sputtering”, Thin Solid Films 238 (1994) 44-50. DOI: 10.1016/0040-6090(94)90646-7

[33] Z. M. Detweiler, S. M. Wulfsberg, M. G. Frith, A. B. Bocarsly, S. L. Bernasek, “The oxidation and surface speciation of indium and indium oxides exposed to atmospheric oxidants”, Surf. Sci. 648 (2016) 188-195. DOI: 10.1016/j.susc.2015.10.026

[34] L. Fang, S. J. Baik, J. W. Kim, S. J. Kang, J. W. Seo, J. W. Jeon, Y. H. Kim, K. S. Lim,” Tunable work function of a WOx buffer layer for enhanced photocarrier collection of pin-type amorphous silicon solar cells”, J. Appl. Phys. 109 (2011) 104501. DOI: 10.1063/1.3583576

[35] D. Beena, K. J. Lethy, R. Vinodkumar, V.P. Mahadevan Pillai, V. Ganesan, D.M. Phase, S.K. Sudheer, “Effect of substrate temperature on structural, optical and electrical properties of pulsed laser ablated nanostructured indium oxide films”, Appl. Surf. Sci. 255 (2009) 8334-8342. DOI: 10.1016/j.apsusc.2009.05.057

[36] R. R. Krishnan, V. S. Kavitha, S. R. Chalana, R. Prabhu and V. P. M. Pillai, “Effect of tungsten doping on the properties of In2O3 films”, JOM 71:5 (2019) 1885-1896. DOI: 10.1007/s11837-019-03426-7

[37] M. Boccard, N. Rodkey, Z. C. Holman, “High-mobility hydrogenated indium oxide without introducing water during sputtering”, Energy Procedia 92 (2016) 297-303. DOI: 10.1016/j.egypro.2016.07.083

[38] L. Martini, L. Serenelli, F. Menchini, M. Izzi, M. Tucci, “Silicon heterojunction solar cells toward higher fill factor”, Prog. Photovolt: Res. Appl. 28 (2020) 307-320. DOI: 10.1002/pip.3241

[39] L. Serenelli, L. Martini, F. Menchini, M. Izzi, G. de Cesare, G. Condorelli, C. Gerardi, D. Muñoz, M. Tucci, “Selective contacts and fill factor limitations in heterojunction solar cells”, Prog. Photovolt: Res. Appl. 29 (2021) 876-884. DOI: 10.1002/pip.3418

[40] E. Centurioni and D. Iencinella, “Role of front contact work function on amorphous silicon/crystalline silicon heterojunction solar cell performance”, IEEE Electron Device Lett. 24:3 (2003) 177-179. DOI: 10.1109/LED.2003.811405

Chapter 6

Additional research

During the period of the PhD course, I contributed to experimental investigations reported in several peer-reviewed papers. Such side investigations, which do not exactly match the main research topic but that however in most cases concern photovoltaic topics, constitute a complement to my work of the period. The results are summarised in the following, specifying my contribution to the research.

Mechanically stacked, two-Terminal Graphene-Based Perovskite/Silicon Tandem Solar Cell with Efficiency over 26%

E. Lamanna, F. Matteocci, E. Calabrò, L. Serenelli, E. Salza, L. Martini, F. Menchini, M. Izzi, A. Agresti, S. Pescetelli, S. Bellani, A. Esaù Del Río Castillo, F. Bonaccorso, M. Tucci, A. Di Carlo

Joule 4 (2020) 1-17

Adapted from summary and conclusions

Perovskite/silicon tandem solar cells represent an attractive pathway to upgrade the market-leading crystalline silicon technology beyond its theoretical limit. Two-terminal architectures result in reduced plant costs compared to four-terminal ones. However, it is challenging to monolithically process perovskite solar cells directly onto the micrometer-sized texturing on the front surface of record-high efficiency amorphous/crystalline silicon heterojunction cells, which limits both high-temperature and solution processing of the top cells. To tackle these hurdles, we present an innovative and highly efficient two-terminal perovskite/silicon tandem configuration, which is obtained by a simple mechanical stacking of the sub-cells. The two sub-cells are independently optimized to maximize the PCE and, at the same time, to minimize the optical losses within the multiple layers and interfaces. Bifacial mesoscopic perovskite solar cells have been optimized for their implementation in tandem solar cells by (1) carrying out a low-power sputtering process over a PTAA hole selective layer to preserve its optoelectronic properties during the deposition of the ITO counter electrode without needing a protective oxide-based buffer layer; (2) engineering the optical design by identifying the ideal thickness of the ITO counter electrode to reduce the reflective optical losses at the PTAA/ITO interface; and (3) incorporating graphene flakes into the $cTiO_2$ and $mTiO_2$, used as electron selective layers, in order to lower the series resistance and enhance the electron extraction efficiency. Such optimized bifacial perovskite solar cells have been used as top cells in tandem devices adopting either double-side textured c-Si and Si HJT bottom cells, reaching a champion PCE of 26.3% in reverse voltage scan mode (25.7% in forward voltage scan mode and stabilized PCE of 25.9%) over an active area of 1.43 cm^2. Our “mechanical approach,” based on the

independent optimization and fabrication of the sub-cells, is ready to synergistically exploit the most recent progress achieved in both perovskite and silicon solar cells, as well as their corresponding modules, in order to propel perovskite/silicon tandem solar cells beyond current photovoltaic technology established in the market.

Contribution to the work

I collaborated to the characterisation of the perovskite solar cell via spectrophotometric and quantum efficiency measurements, and to the J-V characterisation of the tandem devices.

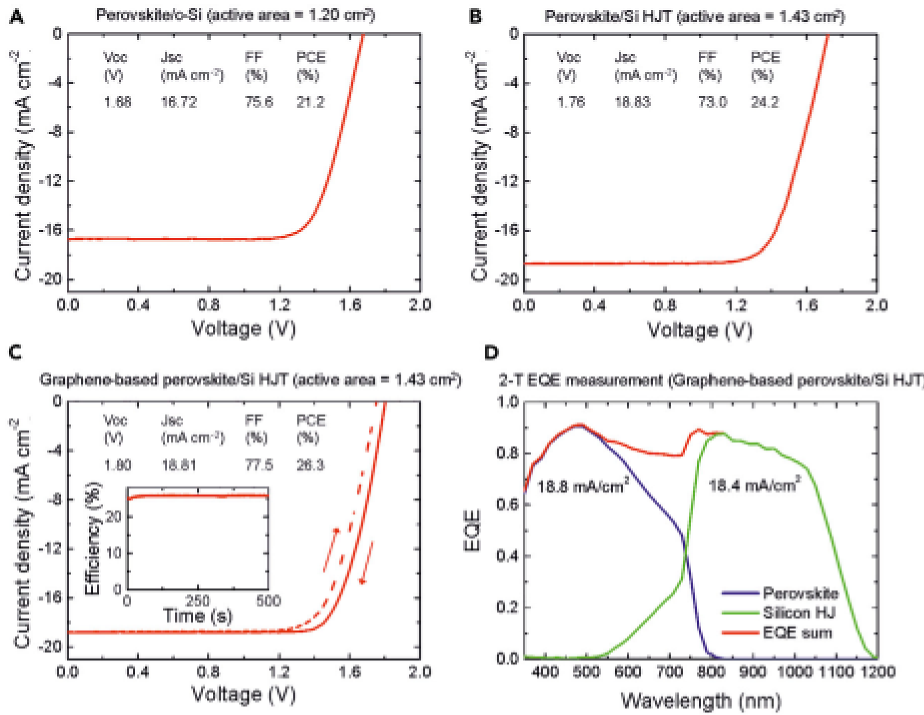

Figure 4. Performance of Mechanically Stacked Two-Terminal Perovskite/Silicon Tandem Solar Cells

(A–C) J-V characteristic of the perovskite/c-Si, perovskite/Si HJT tandem, and graphene-based perovskite/Si HJT tandem solar cells. In (A) and (B), the J-V curves have been measured in reverse voltage scan mode. In (C), both forward and reverse voltage scan mode have been used to measure the J-V curves. The inset to (C) shows the PCE measured over time at the MPP (i.e., the stabilized efficiency).

(D) EQE spectra of the stand-alone graphene-based perovskite and Si HJT sub-cells. The EQE spectrum of the Si HJT cell filtered by the graphene-based perovskite top cell is also shown for the analysis of the "current-matching condition."

Copper-Based Corrole as Thermally Stable Hole Transporting Material for Perovskite Photovoltaics

A. Agresti, B. Berionni Berna, S. Pescetelli, A. Catini, F. Menchini, C. Di Natale, R. Paolesse, A. Di Carlo

Adv. Funct. Mater. (2020) 2003790

Adapted from summary and conclusions

Perovskite solar cells (PSCs) represent nowadays a promising starting point to develop a new efficient and low-cost photovoltaic technology due to the demonstrated power conversion efficiency (PCE) exceeding 25% on small area devices. However, best reported devices suffer from stability issue under real working conditions thus slowing down the race for the commercialization. In particular, the hole transporting material commonly employed in mesoscopic n–i–p PSCs (nip-mPSCs), namely spiro-OMeTAD, is strongly corrupted when subjected to temperatures above 70 °C due to intrinsic thermal instability and because of the dopant employed to improve the hole mobility. In this work, the novel use of a copper-based corrole as HTM is proposed to improve the device thermal stability of nip-mPSCs under prolonged 85 °C stress conditions. Corrole-based devices show remarkable PCE above 16% by retaining more than 65% of the initial PCE after 1000 h of thermal stress, while spiro-OMeTAD cells abruptly lose more than 60% after the first 40 h. Once scaled-up to large area modules, the proposed device structure can truly represent a possible way to pass thermal stress tests proposed by IEC-61646 standards and, not less importantly, the high temperature required by the lamination process for panel production.

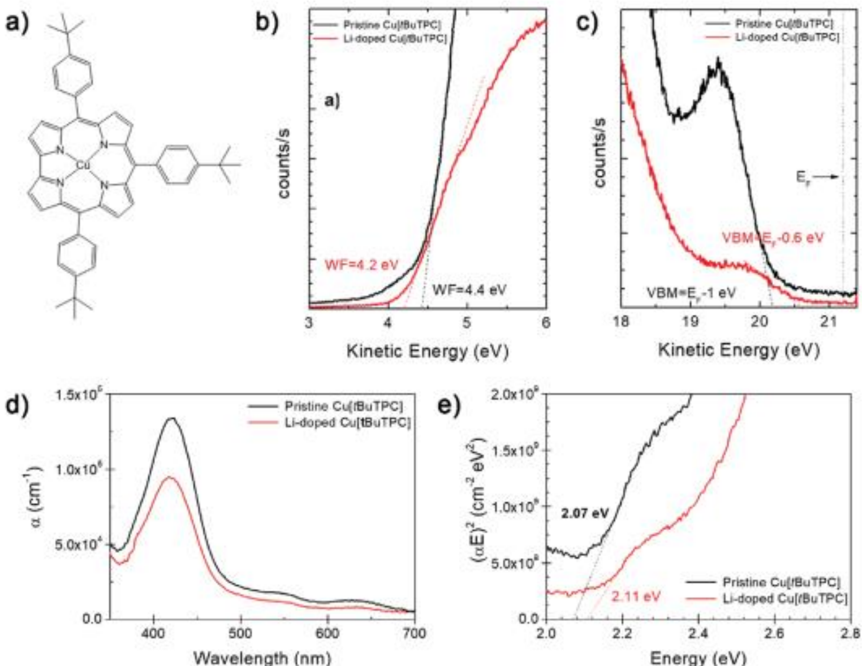

Figure 1. a) Chemical structure of Cu[*t*BuTPC]; UPS spectra of Cu[*t*BuTPC] samples, in their pristine (black line) and Li-doped form (red line). b) Work function of the two HTMs, obtained through low-energy data mining. c) Distance from E_F to VBM (obtained through high-energy data mining). d) UV–vis spectra and e) Tauc plot for pristine (black line) and Li-doped (red line) Cu[*t*BuTPC] films.

We have prepared and tested for the first time a corrole derivative as HTM in perovskite solar cells. Mesoscopic perovskite based solar cells achieved power conversion efficiency of 13.11% and 16.49%, when pristine and doped corroles were used as hole transporting material, respectively. Corrole outstanding conductivity, together with the improved device thermal stability, demonstrated after 1000 h at 85 °C, make this derivative an excellent and cheaper alternative to the standard spiro-OMeTAD. Considering the absence of corrole-based HTMs for PSCs, this study paves the way for the exploitation of new hole transporting materials based on porphyrinoids. Moreover, the superior thermal stability showed by corrole-based HTLs, opens a route for the replacement of commonly employed spiro-OMeTAD HTM, by suggesting an easy and fast way to scale-up the perovskite solar cell technology up to panel configuration.

Contribution to the work

I performed the spectrophotometric and UPS characterisation of the corrole materials and contributed to the definition of the band energy diagram of the material.

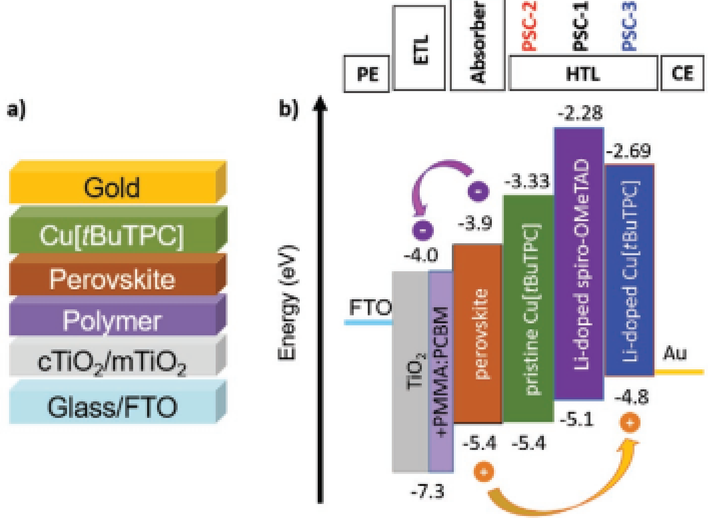

Figure 2. a) Schematic structure and b) energy band diagram of investigated PSC structure. Valence (VB) and conduction band (CB) values for polymer passivated TiO_2 ETL was taken from UPS measurements reported in ref. [59]; highest occupied molecular orbital (HOMO) and lowest unoccupied molecular orbital (LUMO) levels were derived from UPS measurements reported in ref. [60] for perovskite layer while from ref. [61] for Li-doped spiro-OMeTAD HTM. Finally, HOMO levels of pristine and Li-doped Cu[*t*BuTPC] were experimentally determined in this work by UPS measurements while LUMO levels are estimated according to the following equation: $E_{LUMO} = E_{HOMO} + E_g$ (optical bandgap).

A novel water-resistant and thermally stable black lead halide perovskite, phenyl viologen lead iodide $C_{22}H_{18}N_2(PbI_3)_2$

A. Latini, S. Quaranta, F. Menchini, N. Lisi, D. Di Girolamo, O. Tarquini, M. Colapietro, L. Barba, N. Demitri, A. Cassetta

Dalton Trans. 49 (2020) 2616

Adapted from summary and conclusions

A novel black organoammonium iodoplumbate semiconductor, namely phenyl viologen lead iodide $C_{22}H_{18}N_2(PbI_3)_2$ (PhVPI), was successfully synthesized and characterized. This material showed physical and chemical properties suitable for photovoltaic applications. Indeed, low direct allowed band gap energy (Eg = 1.32 eV) and high thermal stability (up to at least 300 °C) compared to methylammonium lead iodide CH3NH3PbI3 (MAPI, Eg = 1.5 eV) render PhVPI potentially attractive for solar cell fabrication. The compound was extensively characterized by means of X-ray diffraction (performed on both powder and single crystals), UV-Vis diffuse reflectance spectroscopy (UV-Vis DRS), UV-photoelectron spectroscopy (UPS), FT-IR spectroscopy, TG-DTA, and CHNS analysis. Reactivity towards water was monitored through X-ray powder diffraction and thermal stability was evaluated by temperature-controlled powder XRD measurements. Phenyl viologen lead iodide can be amenable for the fabrication of solar devices by spin coating as actually done for MAPI-based cells. The crystal structure, determined by means of single crystal X-ray diffraction using synchrotron radiation, turned out to be triclinic and consequently differs from the prototypal perovskite structure. Finally, the determination of the electron band energies with respect to the vacuum level (i.e. E_F=-4.9 eV, CB=-4.4 eV, and VB=-5.7 eV) can pave the way for further investigation dedicated to the development of appropriate combinations of electron donor and acceptor materials to be used along with PhVPI in thin film solar cells.

Contribution to the work

I performed the spectrophotometric and UPS characterisation of the corrole materials and contributed to the definition of the band energy diagram of the material.

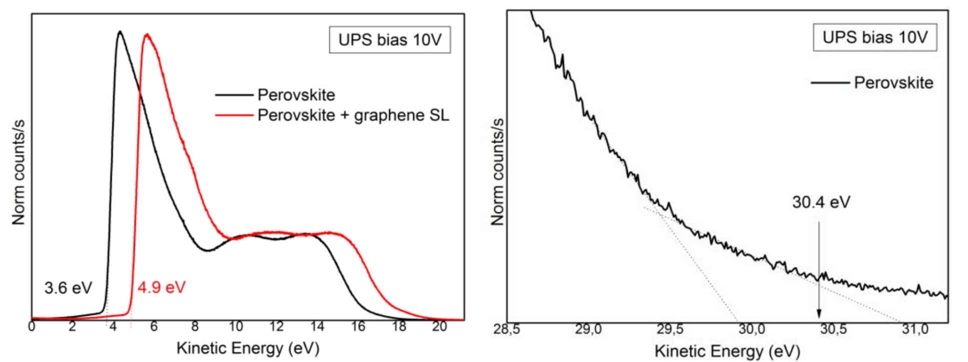

Fig. S7. Normalised UPS spectrum of a perovskite sample before (black) and after (red) being covered by a graphene monolayer.

Fig. S8. Normalised UPS spectrum of the perovskite sample: zoom of the VBM region.

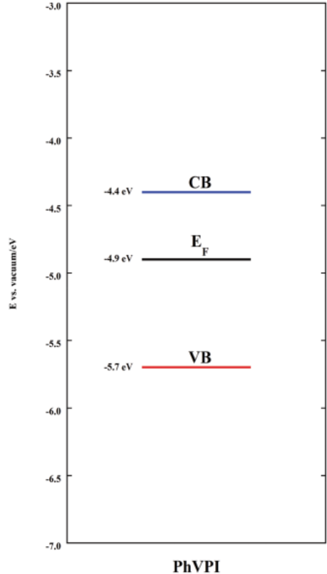

Fig. 10 Positions of the band edges and Fermi level of PhVPI with respect to the vacuum level.

The Prevention of Implant Surface Alterations in the Treatment of Peri-Implantitis: Comparison of Three Different Mechanical and Physical Treatments

M. Lollobrigida, L. Fortunato, G. Serafini, G. Mazzucchi, G. Bozzuto, A. Molinari, E. Serra, F. Menchini, I. Vozza, A. De Biase

Int. J. Environ. Res. Public Health 17 (2020) 2624

Adapted from summary and conclusions

The surgical treatment of peri-implantitis is currently based on the removal of biofilms from the implant surface by primary means of mechanical and physical treatments. However, such approaches often determine some alterations of the implant surface with detrimental effects on re-osseointegration. This study aims to evaluate the effects of four different mechanical and physical
treatments on titanium samples with moderately rough surface. Air powder abrasion (AP) with glycine powder, a titanium brush (TB) and a diode laser at 3 W (L3) and 4 W (L4) were tested. Surface morphology, roughness and chemical composition were then assessed by scanning electron microscope (SEM), white light interferometer and X-ray photoelectron spectroscopy (XPS), respectively. Among the treatments tested in this study, air powder abrasion with glycine powder and 3 W diode laser had the lowest impact on surface physicochemical properties.

Contribution to the work

I performed the XPS analysis on the surface of the samples and calculated the atomic percentage composition of the material left over the implants.

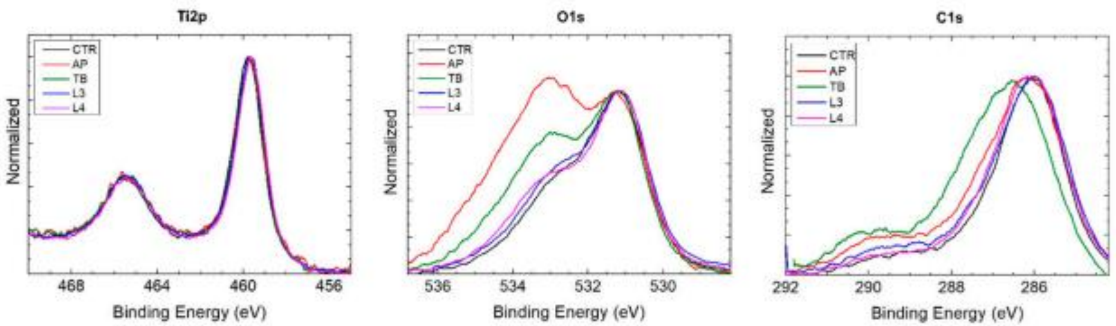

Figure 7. XPS (X-ray photoelectron spectroscopy) analysis of samples showing the spectra of Ti2p, O1s and C1s.

Table 2. Atomic percentage composition of samples.

	Titanium (%)	Oxygen (%)	Carbon (%)	Sodium (%)
CTR	9	43	45	3
AP	4	43	50	3
TB	8	48	42	2
L3	11	50	36	3

Efficacy of combined mechanical and chemical decontamination treatments on smooth and rough titanium surfaces and their effects on osteoconduction: an ex vivo study

M. Lollobrigida, L. Lamazza, M. Di Pietro, S. Filardo, M. Lopreiato, A. Mariano, G. Bozzuto, A. Molinari, F. Menchini, A. Piattelli, A. De Biase

JOMI 37:1 (2022) 57-66

Adapted from summary and conclusions

The aim of this ex vivo study was to assess the ability to remove oral biofilm by different combinations of mechanical and chemical treatments on smooth and rough titanium surfaces, as well as their impact on osteoconduction.

Contribution to the work

I performed XPS spectra on the samples after decontamination, in order to characterise the residual elements.

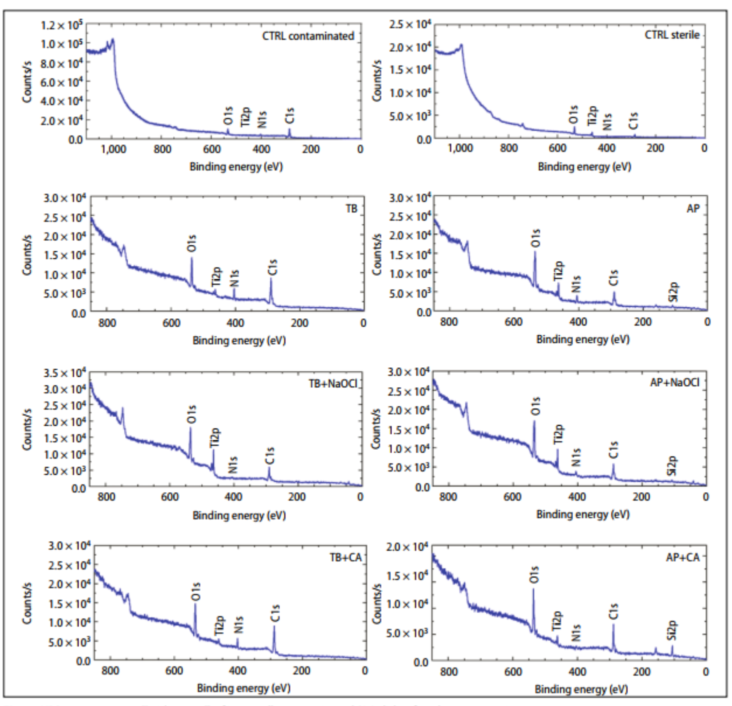

Fig 3 XPS survey spectra ("wide scans") of intraorally contaminated SLA disks after decontamination.

Table 2 Semi-quantitative Analysis of Samples Following Physical or Chemical-Physical Treatments on Human Oral Biofilm Formed on SLA Disks After 24 Hours

	CTRL (Contaminated disk)	CTRL (sterile disk)	TB	TB+NaOCl	TB+CA	AP	AP+NaOCl	AP+CA
N (1s)	5.7	1.3	9.3	1.2	7.0	6.6	3.8	Traces
Na (1s)	–	–	–	Traces	–	7.0	Traces	–
C (1s)	75.8	48.4	66.1	47.4	66.4	39.1	43.7	47.7
O (1s)	18.5	37.7	22.9	40.9	25.3	39.5	41.7	32.3
Ti (2p)	–	12.6	1.7	10.5	1.3	4.5	5.9	2.1

CTRL = control disk; TB = titanium brush; NaOCl = sodium hypochlorite; CA = citric acid; AP = air polishing.

Conclusions

This thesis enrols in the trend-topic of alternative selective contacts for silicon-based heterojunction solar cells, which are sought to replace the traditional amorphous-silicon layers. This substitution would allow avoiding the use of toxic and dangerous gases, thus achieving cheaper and safer industrial manufacturing processes. For the purpose, we have tested several materials and evaluated their performances as hole- and electron-transport layers in silicon-based heterostructures.

Doped nickel oxide possesses ideal energy-band levels to be used as hole-transport layer on an n-type c-Si substrate, but it has not yet been fully exploited. We have deposited lithium-doped nickel oxide (NiOx:Li) films by e-beam evaporation and obtained samples with a higher transparency with respect to the amorphous-silicon counterpart, a large bandgap around 3.7 eV and conductivity between 2×10^{-6} and 1.6×10^{-4} $(\Omega\cdot cm)^{-1}$ for different doping concentrations. A proof-of-concept cell was fabricated which confirmed the correct behaviour of the material as HTL. However it was found out that the reduced performances of the cell were connected to the inevitable x-ray production during the e-beam growth process that causes a well-known damage to the substrate passivation. We then turned to another deposition method, i.e. thermal evaporation, with which again we demonstrated the hole-transport behaviour of the NiOx:Li films. Even in this case, however, the cell performances were limited due to metallic contaminations coming from the evaporation crucibles that again damaged the silicon substrate passivation. As we were not able to avoid such contaminations even after having tested many different crucibles (due to the high evaporation temperature of the NiOx:Li ceramic precursor), we tested another deposition method, in which NiOx was thermally evaporated by Ni metallic pellets in an oxygen reactive atmosphere and doped by a co-evaporation of silver. Even in this case the lifetime measurements revealed a damage to surface passivation. We then borrowed from the literature the idea of some "decoupling" layer to act as a barrier against N diffusion toward the silicon surface and buffer interface. We then tested several materials, such as lithium fluoride, titanium dioxide and a combination of both, and in some cases they turned out to efficiently preserve the initial substrate passivation. We ascribed these results to their ability to respectively block metallic Ni and Ag from the emitter film, even if the complexity of the structures introduced limitations to carrier transport. Even if the same preservation of passivation could not be ensured after thermal annealing, the presented results offer some useful hints for future developments in the direction of protecting the passivating layer from contaminants and damage.

In parallel with the investigations on hole-transport layers, we tested several materials to be used as electron-transport layers useful to produce base contacts in the n-type silicon-based heterostructure. The challenge was to find a base contact able to withstand thermal treatments above 150°C without being degraded. We deposited tungsten-doped titanium oxide by thermal

evaporation, but we found out that the band energies of the material were not suited to the behaviour as electron-transport layer with n-type crystalline silicon. These properties were connected with the used low-temperature deposition technique. We then passed to explore the possibility of forming an ohmic base contact by using a tunnelling decoupling layer between the passivating film and the outer metallic or TCO electrode. Different materials were tested, such as lithium fluoride, magnesium fluoride, zinc sulfide or a combination of them, and some of them actually performed as ohmic contacts, also ensuring a preservation of passivation. The combination MgF_2/LiF was able to provide the highest degree of conservation of the initial lifetime, but still could not ensure an ohmic contact after thermal annealing, even if we demonstrated that MgF_2 film is resistant to thermal treatment up to 200°C for 10 minutes. On this base we will continue the challenge to find the novel material and processes for a new generation of heterojunction solar cell with reduced industrial impact.

During the whole period of the experimental work on new materials, also simulation activities were carried out to complement the research. Some empirical methods to detect hidden barriers at the base contact of HJ cells and transport limitations at the emitter contact were presented. Moreover, the V_{OC} reduction due to the common use of small-area samples was finally evaluated.

The final exploited topic regarded tungsten-doped indium oxide (IWO). This transparent conductive oxide is known to possess high transparency and low resistivity, as requested for a TCO. Moreover it can reach high mobility values coupled with low carrier densities, which allow it to show lower free carrier absorption with respect to traditional TCOs. We deposited IWO films by non-reactive RF sputtering and obtained samples with a high mobility after thermal annealing, up to 70.9 cm/V·s, together with low carrier concentrations of $2\text{-}4\times10^{20}$ cm^{-3}, which resulted in resistivities as low as 2.5×10^{-4} Ω·cm. Most importantly, the deposition of the films was not detrimental for the passivation of the c-Si substrates, as the minority carrier lifetime was recovered or even surpassed after a thermal treatment. IWO films with different work function values were applied to silicon-based heterojunction solar cells and their suitability to complete the selective contacts was demonstrated.

In conclusion, the work performed and discussed in this thesis aimed at examining the potentialities of new materials and new deposition techniques for applications as carrier-selective contacts in silicon-based heterojunction solar cells. We did not mean to follow the already-traced paths, but to explore new possible solutions, with the aim of simplifying the manufacturing process and adding knowledge to the field. We have shown confirmations of the good potentialities of some materials and we have shared some warnings about possible degradation mechanisms connected to metal diffusion. Starting from these results, many routes can be followed to hopefully reach the desired optimal solutions.

Appendix

A.1 Deposition techniques

Plasma-enhanced chemical vapour deposition (PECVD) was employed to deposit the passivation a-SiOx:H layers. The system (Figure A.1) has a parallel-plate configuration with 23 cm diameter plates at a distance of 1.5 cm. The RF generator frequency is 13.56 MHz.

E-beam and thermal evaporation were used to deposit the materials for selective contacts. The typical chamber base pressure is of 10^{-6} mbar. The system accommodates the sample in a rotating dome over the crucibles, and co-evaporation can be performed from two sources. The crucible-to substrate distance is of about 80 cm. The thickness of the deposited films is controlled by a calibrated quartz microbalance.

RF sputtering was employed to grow the IWO films described in Chapter 5. The apparatus, produced by Kenosystec (Figure A.1), consists in an in-line, four-target chamber with a load-lock to minimise ambient contamination and reduce process duration. The typical base pressure is 3×10^{-7} mbar. Argon is used to form the plasma, but other gases (such oxygen or hydrogen) can be added. The target area is 170 cm^2 and the target-to-substrate distance is 6 cm. The substrates are kept oscillating under the target during deposition.

Figure A.1 Picture of the PECVD system (left) and the RF sputtering system (right) available at the TERIN-FSD-IIF laboratories, ENEA.

A.2 Materials

The materials used for e-beam and thermal evaporation described in the following were prepared by Prof. A. Latini from the Chemistry Department of Sapienza University of Roma. Nickel oxide (NiOx) was first obtained by calcination at 800°C of a solution of nickel nitrate hexahydrate

$(Ni(NO_3)_2{\cdot}6\ H_2O)$. Then NiOx was mixed with the appropriate amount of lithium nitrate ($LiNO_3$), and the powder mixture was pressed in a pellet and calcined at 1000°C. The obtained material is nickel lithium oxide ($Ni_{1-x}Li_xO$) with a variable Li content (3% < x < 10% at.), indicated as NiOx:Li in the work. TiO:W was obtained by hydrolysis of solutions of Ti and W alcoxides in hetanol, followed by autoclaving. The obtained solid is then calcined at 500°C to remove organic contaminants and refine the crystallisation of the material. The obtained pellets reveal an anatase phase.

A.3 Experimental methods and measuring techniques

The silicon substrates are constituted by monocrystalline silicon wafers, both flat Floating Zone (250 μm thick) and textured Czochralski (180 μm thick) with 1-5 Ω·cm conductivity. Before any deposition, the wafers are submitted to a standard RCA cleaning procedure consisting in a first bath in an SC1 solution (NH_4OH : H_2O_2 : DIW = 1 : 1 : 5 vol.) at 80°C for 20’, followed by a second bath in an SC2 solution (HCl : H_2O_2 : DIW = 1 : 1 : 6 vol.) at 80°C for 20’.

The silicon wafers are passivated by layers of amorphous hydrogenated silicon oxide (a-SiOx:H) deposited by plasma enhanced chemical vapour deposition (PECVD) at 300°C, with a working pressure of 4000 mTorr, radio frequency power of 15.36 MHz of 9 W, flux of 5% argon-diluted silane (SiH_4) of 120 sccm, flux of hydrogen (H_2) of 200 sccm, flux of carbon dioxide (CO_2) of 1.6 sccm.

Different sample structures were used for different characterisations. The most recurrent are depicted in Figure A..

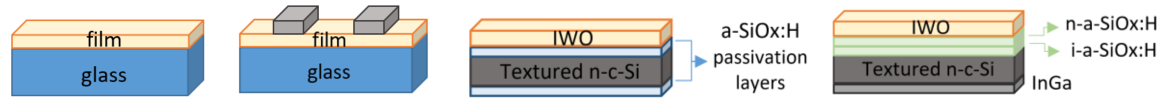

Figure A.2 Sample structures for different measurements: a) film on glass for optical characterisation; b) film on glass with metallic or TCO contacts for planar conductivity, TLM, Hall and activation energy measurements; c) film on passivated c-Si substrate for lifetime measurements; d) IWO film on base contact for WF measurements.

When applicable, the rapid thermal annealing treatment was performed in a furnace in a N_2 atmosphere with fast (2°C/s) heating rate.

The thickness of the thin films grown by e-beam or thermal evaporation (0.7-30 nm) was measured by a calibrated quartz oscillator placed inside the deposition chamber and very close to the substrate. The thickness of thicker RF-sputtered samples (80-120 nm) was evaluated by means of the open-source simulation program* [1] starting from optical data.

Optical characterisations were performed by transmittance (T) and reflectance (R) measurements in a commercial UV-Vis-NIR double-beam spectrophotometer on films coated on borosilicate or sodalime glass slabs. For samples of sufficient thickness (i.e. for which the R and T showed at least one extreme) the complex refractive index ñ=n-ik was calculated by means of an open-source simulation program ksemaw* [1]. The absorption coefficient α was calculated from the absorption coefficient, when available, or from the optical measurements by the approximated formula

$$\alpha = \frac{1}{d} ln \frac{1-R}{T},$$

where d is the thickness of the film. The optical bandgap (Eg) was evaluated by extrapolating the linear part of the Tauc plot of the measurements, as in Figure A.3(left) [2].

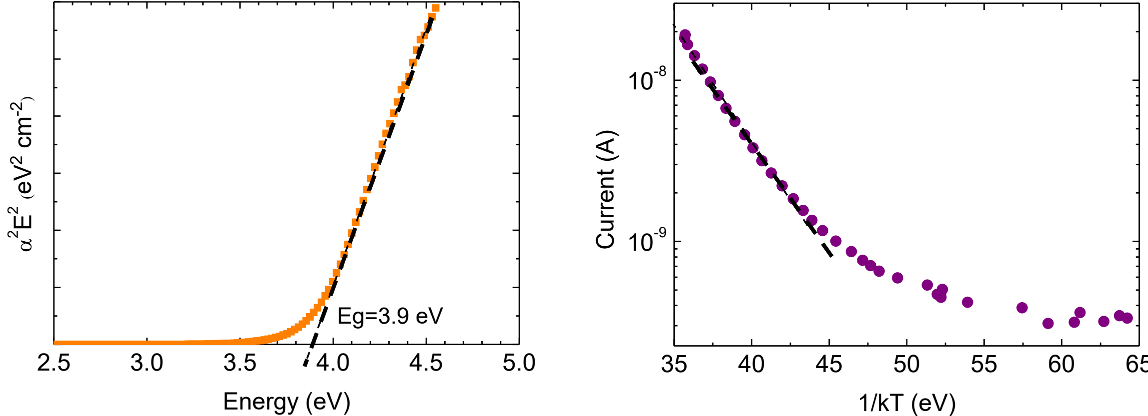

Figure A.3 Tauc plot (left) for the estimation of the direct band gap and Arrhenius plot (right) for the determination of the activation energy.

The conduction properties of the samples were measured on samples deposited on glass over which two contact areas of different materials (metal or TCO) were deposited. The two contacts were used as input/sense terminals for J-V measurements in planar configuration. Current and voltage were applied/measured by a Keytley multimeter in a 2-wire configuration. The resistivity was calculated from the slope of the J-V characteristics at RT. For the evaluation of the activation energy the samples were placed in a liquid nitrogen cryostat and temperatures were varied between 100 and 320 K; the activation energy was be deduced by the slope of the high-temperature linear portion of the Arrhenius plot of J vs 1/kT, as in Figure A.3(right).

The electrical properties of the films deposited on glass, namely carrier type, bulk resistivity (ρ), mobility (μ) and free carrier density (N) were measured by means of the Van der Paw method.

The minority carrier lifetime τ was measured by quasi-steady-state photoconductance measurements in a Sinton WCT-120 instrument. The lifetime τ of a wafer can be expressed as

$$\frac{1}{\tau} = \frac{1}{\tau_B} + \frac{1}{\tau_S}, \quad (1)$$

where τ_B and τ_S refer to the lifetime in the bulk and at the interfaces, respectively. Given that all our substrates have approximately the same intrinsic lifetime this term results negligible in expression (1), so that the total lifetime τ directly reflects the recombination at the interfaces, and thus their quality.

The specific contact resistivity between IWO films and screen-printed silver paste was evaluated by means of the transfer length method (TLM) on 80 nm-thick films deposited on glass.

The semi-quantitative elemental content of the films was derived by the decomposition of the x-ray photoelectron spectroscopy (XPS) spectra obtained in a Vacuum Generator ESCA LAB MKII system using the Al K_α line as an x-ray source. A Shirley background was applied to the data, and Gauss-Lorentz bands were used to decompose the curves. The results are typically affected by a 10-15% error. The same system was equipped by a He lamp to perform UPS spectroscopy. The spectra were calibrated with a Au sample. A 4 V bias was applied to the sample.

The crystallinity of the samples was investigated by x-ray diffraction (XRD) measurements in a RIGAKU Smartlab X-Ray diffractometer with Cu-K_α radiation.

The J-V light characteristics are measured under illumination of a Class A sun simulator which reproduces the standard AM 1.5G conditions equipped by a gold-plated chuck and a 4-terminal Keythley multimeter.

The external quantum efficiency measurements were performed by a home-made system and were corrected with reflectance spectra to obtain the internal quantum efficiency.

The simulated band diagrams and J-V characteristics are obtained with a home-made numerical simulator which details can be found in [3]. The program is based on the Anderson approximation and on the hypothesis of high-quality c-Si substrates. Each layer is described by several parameters among which its electron affinity, energy gap, concentration of dopants and carrier mobility, and the simulator solves the Poisson, continuity and current equations.

A.4 GDOES measurements

The elemental content of the samples was qualitatively evaluated via glow discharge optical emission spectroscopy (GDOES) in a Horiba instrument. The sample is etched by an Ar plasma, and the removed material is ionised by the plasma, emitting a radiation which wavelength can be strictly related to the excited element. A spectrometer reveals the signal relative to the different elements. The technique is destructive, as it produces a crater in the sample, and only qualitative, since no calibration of the signal is performed.

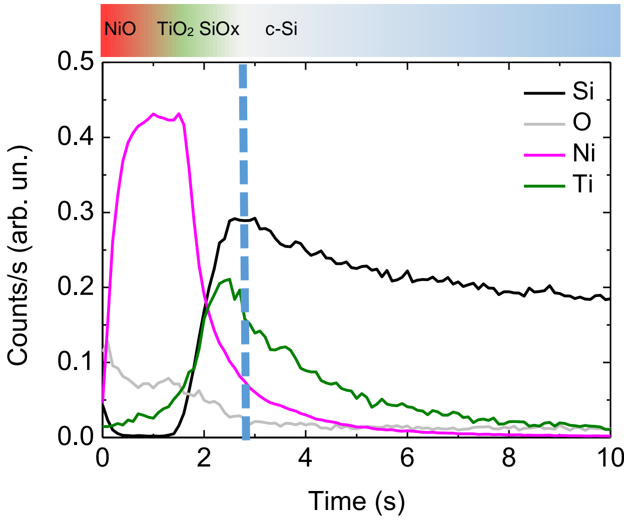

Figure A.4 GDOES profile of a Si/SiOx/TiO_2/NiO structure.

In Figure A.4 we show a GDOES profile similar to those shown in Chapters 3 and 4. The sample is composed by a crystalline silicon substrate, a 5.5 nm-thick SiOx, a 2 nm-thick TiO_2 layer and a 7 nm-thick NiO layer. The spectra show the signal variation for each element vs the etching time, which is proportional to the etched thickness of material. If the etching profile of the crater were parallel to the sample surface, neat edges of the signals would be detected in correspondence to the interfaces of multilayered structures. In real cases, the crater profiles have complex shapes (see Figure A.5), which depend also on the sputtering parameters, the etched material and the substrate shape and conductivity. For this reason the signals at the layers interfaces do not present steep variations but show some tail. This makes that we cannot be sure about the exact positioning of the several sample interfaces, nor clearly understand if the long tails of each element are actually penetrating in the adjacent layers. The oxygen signal can be used as an indicator of the presence of some oxide layers over the c-Si substrate, and we can be sure that there will be no oxygen inside the c-Si substrate. So we can place a blue vertical line where the oxygen signal ends and use it as an approximate mark of the c-Si interface. It is seen that the decrease of oxygen occurs in correspondence of the maximum of the Si signal, so that such position will be considered as the beginning of the c-Si substrate. Moreover, because of the different etching rates of the elements, when passing from a layer to another no proportionality is kept between the etching time and the etched thickness, so that along the x-axis no indication can be extracted about the thickness of the payers. In conclusion, only comparisons between samples with identical structures can give some indications of the differences between the composing elements.

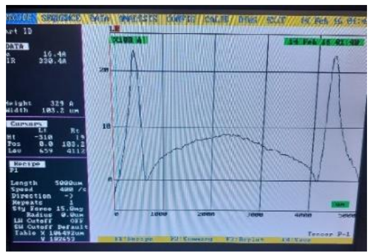
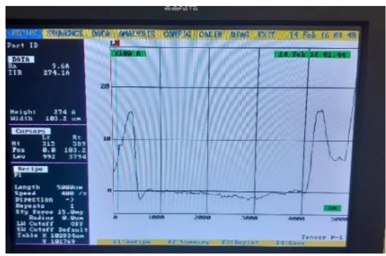
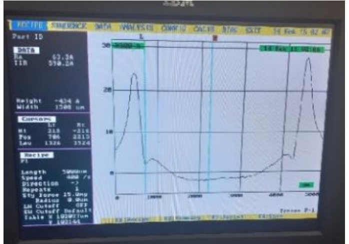

Figure A.5 Different crater profiles revealed by a mechanical profilometer.

A.5 Ohmic contact with InGa

Some of the samples described in the thesis were not full cells, as it was not possible to deposit a traditional n-a-Si/TCO/metal contact on the back side. The materials and structures under investigation were deposited only on one side of the c-Si substrate. This was done in experiments where it was necessary to investigate the partial response of devices after single fabrication steps. In these cases, in order to measure the J-V characteristics of the samples, it was necessary to ensure an ohmic contact on the un-deposited side of the Si substrate, which was actually most of the times covered by the passivating SiOx layer.

InGa eutectic, with its work function of approximately 4.1 eV, is suitable for the purpose. We tested this possibility on samples composed by a c-Si substrate which was passivated by SiOx only on the back side. The front side (c-Si) is directly contacted by InGa, as the contact is known to be ohmic. The direct application of InGa over the back SiOx layer did not allow the formation of an ohmic contact (red line in Figure A6), nor did a mechanical scratch on the passivated silicon surface help “freeing” enough bulk Si surface for the InGa to contact it (blue line in Figure A6). We then completely etched the SiOx film by a reiterated application of hydrofluoric acid (HF) and hydrogen peroxide (H_2O_2): first the acid starts dissolving the oxide film, then the H_2O_2 liquid re-oxidises the surface, that can be more efficiently removed by the subsequent HF application; the process is repeated 3 times until the complete removal of the oxide film is obtained. When InGa is applied to the so-treated surface, the measured J-V transverse characteristic is ohmic (green line in Figure A6). This procedure allows obtaining an ohmic contact by a quite elaborated procedure, which is however faster and easier than the standard deposition of the base contact, and which is useful when only a first quick evaluation of the device is required. Moreover, this is an easy way to obtain an ohmic contact on the c-Si wafers that we use, which have a quite low ~ 5 Ω·cm resistivity that often poses some problems when trying to establish a good ohmic contact.

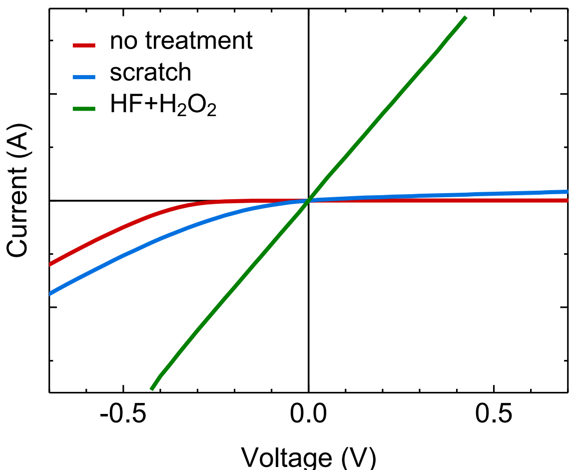

Figure A.6 Transverse J-V characteristic of c-Si substrate contacted as follows: on the front side, InGa was applied on the clean c-Si surface; on the back side, InGa was applied on the SiOx-passivated c-Si surface after the treatments indicated in the legend.

References to Appendix

[1] M. Montecchi, A. Mittiga, C. Malerba, F. Menchini, “KSEMAW: an open source software for the analysis of spectrophotometric, ellipsometric and photothermal deflection spectroscopy measurements”, Open Research Europe (2021), 1:95. DOI: 10.12688/openreseurope.13842.1

[2] J. Tauc, R. Grigorovici and A. Vancu, “Optical properties and electronic structure of amorphous germanium”, Phys. Stat. Sol. 15 (1966) 627. DOI: 10.1002/pssb.19660150224

[3] L. Martini, L. Serenelli, F. Menchini, M. Izzi, M. Tucci, “Silicon heterojunction solar cells toward higher fill factor”, Prog. Photovolt: Res. Appl. 28 (2020) 307-320. DOI: 10.1002/pip.3241

List of publications and contributions to conferences

During the three years of PhD project I disseminated part of the work described in the thesis in the form of peer-reviewed papers, presentations to national and international conferences and project reports. Here I summarise the references.

Peer-reviewed papers

[1] M. Lollobrigida, L. Lamazza, M. Di Pietro, S. Filardo, M. Lopreiato, A. Mariano, G. Bozzuto, A. Molinari, F. Menchini, A. Piattelli, A. De Biase, "Efficacy of combined mechanical and chemical treatments on smooth and rough titanium surfaces and their effects on osteoconduction: an ex vivo study", International Journal of Oral & Maxillofacial implants 37:1 (2022) 57-66. DOI: 10.11607/jomi.9105

[2] M. Montecchi, A. Mittiga, C. Malerba, F. Menchini, "KSEMAW: an open source software for the analysis of spectrophotometric, ellipsometric and photothermal deflection spectroscopy measurements", Open Research Europe 1:95 (2021) 1-27. DOI: 10.12688/openreseurope.13842.1

[3] L. Serenelli, L. Martini, F. Menchini, M. Izzi, G. de Cesare, G. Condorelli, C. Gerardi, D. Muñoz, M. Tucci, "Selective contacts and fill factor limitations in heterojunction solar cells", Progress in Photovoltaics: Research and Applications 29 (2021) 876-884. DOI: 10.1002/pip.3418

[4] L. Martini, L. Serenelli, F. Menchini, M. Izzi, M. Tucci, "Silicon heterojunction solar cells toward higher fill factor", Progress in Photovoltaics: Research and Applications 28 (2020) 307-320. DOI: 10.1002/pip.3241

[5] E. Lamanna, F. Matteocci, E. Calabrò, L. Serenelli, E. Salza, L. Martini, F. Menchini, M. Izzi, A. Agresti, S. Pescetelli, S. Bellani, A. Esaù Del Río Castillo, F. Bonaccorso, M. Tucci, and A. Di Carlo, "Mechanically stacked, two-terminal graphene-based perovskite/silicon tandem solar cell with efficiency over 26%", Joule 4 (2020) 1-17. DOI: 10.1016/j.joule.2020.01.015

[6] A. Latini, S. Quaranta, F. Menchini, N. Lisi, D. Di Girolamo, O. Tarquini, M. Colapietro, L. Barba, N. Demitri and A. Cassetta, "A novel water-resistant and thermally stable black lead halide perovskite, phenyl viologen lead iodide $C_{22}H_{18}N_2(PbI_3)_2$", Dalton Transactions 49 (2020) 2016-2627. DOI: 10.1039/c9dt04148f

[7] A. Agresti, B. Berionni Berna, S. Pescetelli, A. Catini, F. Menchini, C. Di Natale, R. Paolesse, and A. Di Carlo, "Copper-based corrole as thermally stable hole transporting material for perovskite photovoltaics", Advanced Functional Materials (2020) 200379., DOI: 10.1002/adfm.202003790

[8] M. Lollobrigida, L. Fortunato, G. Serafini, G. Mazzucchi, G. Bozzuto, A. Molinari, E. Serra, F. Menchini, I. Vozza and A. De Biase, "The prevention of implant surface alterations in the treatment of peri-implantitis: comparison of three different mechanical and physical

treatments", International Journal of Environmental Research and Public Health 17 (2020) 2624. DOI: 10.3390/ijerph17082624

Submitted papers

[9] L. A. Castriotta, E. Calabrò, F. Di Giacomo, S. Harshavardhan Reddy, D. Takhellambam, B. Paci, A. Generosi, L. Serenelli, F. Menchini, L. Martini, M. Tucci, A. Di Carlo, "An universal multi-additive strategy to enhance efficiency and stability in inverted perovskite solar cells", submitted to Nano Energy (2022)

[10] F. Menchini, L. Serenelli, L. Martini, G. Stracci, E. Salza and M. Tucci, "High mobility tungsten-doped indium oxide (IWO) for heterojunction solar cells deposited by room-temperature non-reactive RF sputtering", submitted to Applied Surface Science (2022)

[11] L. Serenelli, L. Martini, F. Menchini, M. Izzi, M. Tucci, "Open circuit voltage reduction due to recombination at the heterojunction solar cell edge", submitted to Solar Energy (2022)

Contributions to conferences

[12] F. Menchini, "UV photoelectron spectroscopy as a tool for characterizing materials for photovoltaic applications", NanoInnovation 2022, Roma, 2022, Invited talk and Book of Abstracts

[13] F. Menchini, L. Serenelli, L. Martini, E. Salza, P. Mangiapane, M. Tucci, "Lithium fluoride as an interlayer in transparent selective contacts for heterojunction solar cells", 8th World Conference on Photovoltaic Energy Conversion, Milano, 2022, Visual presentation and Book of Abstracts

[14] F. Menchini, L. Serenelli, L. Martini, E. Salza, G. Stracci, M. Tucci, "High-mobility IWO films deposited in nonreactive plasma by RF sputtering", 8th World Conference on Photovoltaic Energy Conversion, Milano, 2022, Visual presentation and Book of Abstracts

[15] E. Nonni, F. Matteocci, L. Serenelli, E. Magliano, M. Tucci, L. Martini, F. Menchini, A. Di Carlo, "Two-terminal perovskite/silicon tandem based on double cation formulation", 8th World Conference on Photovoltaic Energy Conversion, Milano, 2022, Oral presentation and Book of Abstracts

[16] F. Menchini, L. Serenelli, L. Martini, E. Salza, G. Stracci, M. Izzi, M. Tucci, "IWO films for silicon heterojunction solar cells: effects of the sputtering conditions on optoelectronic properties and carrier lifetime", 38th European Photovoltaic Solar Energy Conference and Exhibition, Online, 2021, Visual presentation and Book of Abstracts

[17] L. Serenelli, L. Martini, F. Menchini, M. Izzi, M. Tucci, "Edge Recombination Influence on the V_{OC} of Silicon Heterojunction solar cells", 38th European Photovoltaic Solar Energy Conference and Exhibition, Online, 2021, Visual presentation and Book of Abstracts

[18] F. Menchini, L. Serenelli, S. Rakhshani, L. Martini, A. Latini, G. de Cesare, D. Caputo, E. Salza, G. Stracci, M. Izzi, M. Tucci, "Lithium-doped nickel oxide as hole transport layer for heterostructure solar cells", 37th European Photovoltaic Solar Energy Conference and Exhibition, Online, 2020, Visual presentation and Book of Abstracts

[19] L. Serenelli, L. Martini, F. Menchini, M. Izzi, G. Condorelli, C. Gerardi, M. Tucci, “Base contact as fill factor limitation in heterojunction solar cells”, 37th European Photovoltaic Solar Energy Conference and Exhibition, Online, 2020, Oral presentation and Book of Abstracts

Project reports

[20] M. Della Noce, M. L. Addonizio, E. Bobeico, M. Ferrara, L. Fusco, M. Izzi, L. Lancellotti, C. Malerba, P. Mangiapane, L. Martini, F. Menchini, L. V. Mercaldo, E. Salza, L. Serenelli, G. Stracci, I. Usatii, P. Scognamiglio, L. Verdoliva, M. Tucci, P. Delli Veneri, “Definizione di processi e materiali per la realizzazione di celle ad eterogiunzione di silicio”, Report RdS/PTR(2021)322, Ricerca di Sistema, Accordo ENEA-MiSE, 2021

[21] L. Serenelli, L. V. Mercaldo, E. Bobeico, A. De Maria, M. Della Noce, M. Ferrara, V. La Ferrara, L. Lancellotti, G. Rametta, G. V. Sannino, A. Romano, I. Usatii, L. Martini, F. Menchini, E. Calabrò, E. Nonni, F. Matteocci, M. Tucci, P. Delli Veneri, “Definizione di materiali e architetture per la realizzazione di celle solari tandem perovskite/silicio”, RdS/PTR(2021)/324, Ricerca di Sistema, Accordo ENEA-MiSE, 2021

[22] M. L. Addonizio, E. Bobeico, M. Della Noce, L. Fusco, L. Lancellotti, C. Malerba, P. Mangiapane, L. Martini, F. Menchini, L. V. Mercaldo, E. Salza, L. Serenelli, G. Stracci, I. Usatii, L. Verdoliva, M. Tucci, P. Delli Veneri, “Sviluppo di processi e materiali innovativi per celle ad eterogiunzione di silicio”, Report RdS_PTR_2020_231, Ricerca di Sistema, Accordo ENEA-MiSE, 2020

[23] L. Martini, F. Menchini, L. Serenelli, D. Caputo, M. Tucci, G. de Cesare, “Sviluppo di materiali a film sottile per contatti selettivi in celle solari ad eterogiunzione di silicio”, Report RdS_PTR_2020_232, Ricerca di Sistema, Accordo ENEA-MiSE, 2020

[24] E. Bobeico, A. De Maria, M. Della Noce, M. Ferrara, V. La Ferrara, L. Lancellotti, L. V. Mercaldo, G. Rametta, G. V. Sannino, A. Romano, I. Usatii, L. Martini, L. Serenelli, F. Matteocci, A. Agresti, M. Tucci, P. Delli Veneri, “Sviluppo di materiali e architetture per celle solari tandem perovskite/silicio”, Report RdS_PTR_2020_234, Ricerca di Sistema, Accordo ENEA-MiSE, 2020

[25] M. L. Addonizio, E. Bobeico, M. Della Noce, L. Fusco, L. Lancellotti, L. Martino, F. Menchini, L. V. Mercaldo, I. Usatii, L. Verdoliva, M. Tucci, P. Delli Veneri, “Film di MoOx e WOx come trasportatori di lacune in celle in silicio e processi di testurizzazione dei wafer di Si”, Report RdS/PTR2019/154, Ricerca di Sistema, Accordo ENEA-MiSE, 2019

[26] L. Serenelli, L. Martini, E. Salza, F. Menchini, M. Izzi, M. Tucci, E. Bobeico, A. De Maria, M. Della Noce, V. La Ferrara, L. Lancellotti, L. V. Mercaldo, G. Rametta, I. Usatii, P. Delli Veneri, E. Lamanna, F. Matteocci, E. Calabrò, A. Di Carlo, “Sviluppo di celle solari tandem perovskite/silicio”, Report RdS/PTR2019/155, Ricerca di Sistema, Accordo ENEA-MiSE, 2019